

# Electronic and catalytic properties of two-dimensional materials and van der Waals heterostructures

**Americo, Stefano**

*Publication date:*
2023

*Document Version*
Publisher's PDF, also known as Version of record

**DTU Physics**
Department of Physics

Ph.D. Thesis

# Electronic and catalytic properties of two-dimensional materials and van der Waals heterostructures

Stefano Americo, October 2023

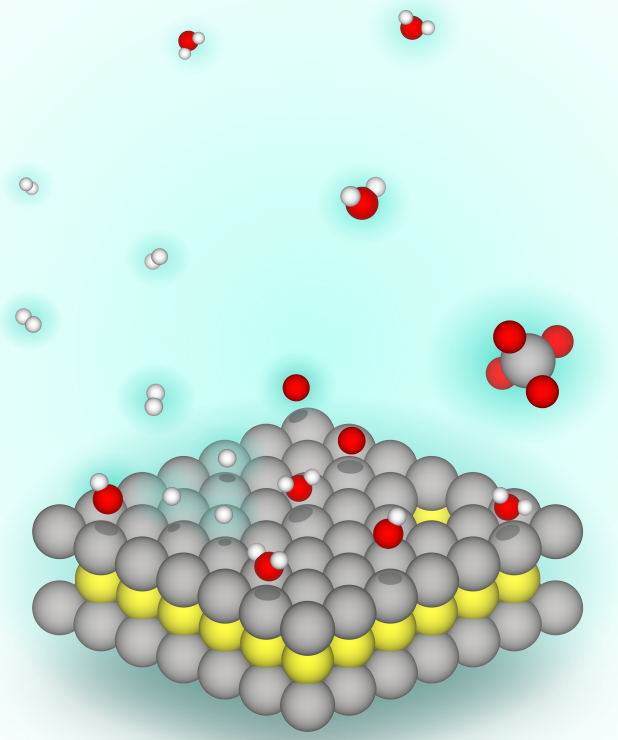

**DTU Physics**
Department of Physics

Ph.D. Thesis

# Electronic and catalytic properties of two-dimensional materials and van der Waals heterostructures

Stefano Americo

Kongens Lyngby, 2023

**Electronic and catalytic properties of two-dimensional materials and van der Waals heterostructures**

Ph.D. Thesis
Stefano Americo
September 30th, 2023



Cover: Artistic representation of a 2D material in contact with an acqueous solution, in presence of water molecules, various adsorbates and an ion originated from a surface vacancy.

Technical University of Denmark
DTU Physics
Department of Physics

Fysikvej 311
2800 Kongens Lyngby, Denmark
Phone: +45 4525 3344
info@fysik.dtu.dk

www.fysik.dtu.dk

# Preface

This thesis is submitted in candidacy for a Ph.D. degree in Physics from the Technical University of Denmark (DTU). The Ph.D project was carried out at the Center for Atomic-scale Materials Design (CAMD) at the DTU Department of Physics between August 2020 and September 2023. The project was supervised by Main Supervisor Professor Kristian S. Thygesen and Supervisor Associate Professor Thomas Olsen, while funded by the European Research Council (ERC) under the European Union's Horizon 2020 research and innovation program Grant No. 773122 (LIMA).

The thesis also includes work conducted at an external stay hosted by Ramon y Cajal researcher Sara Barja Martinez at the Centro the Fisica de Materiales (CFM) at the Universidad del Pais Vasco – Euskal Herriko Unibertsitatea (UPV/EHU) during the months of March, April and May 2023.

Stefano Americo

Kongens Lyngby, September 30th, 2023

# Abstract

Since the isolation of graphene back in 2004, two-dimensional (2D) materials have been at the cutting edge of materials research in both physics and chemistry. Their fascinating electronic structure, unique mechanical properties and unmatched versatility has made them them over the years an ideal platform for exploring a number of applications in electronics, optics, quantum technologies, catalysis and many more. In this thesis, we investigate the electronic and catalytic properties of a wide range of 2D materials by means of Density Functional Theory (DFT) calculations. We show how computational approaches can be employed in order to drive the discovery of novel 2D materials, make predictions on the catalytic activity, assess the stability in acqueous environment and reproduce fine hybridization effects.

One of the most interesting classes of 2D materials is represented by van der Waals heterostructures. By stacking different 2D monolayers one can obtain a virtually infinite number of new hybrid structures with unique properties. The latter are influenced not only by the nature of the individual layers, but also by their relative rotation angle, which can be freely modulated thanks to the dispersive nature of the layer-layer interactions. Herein, we first introduce a lattice matching procedure necessary for generating input structures of van der Waals heterobilayers for *ab-initio* calculations. Then, we implement a self-consistent scissors operator able to reproduce the quasi-particle electronic structure of large heterostructures at the cost of a PBE calculation. The method is benchmarked against experimental data, showing that twist angle-dependent interlayer hybridization effects can be effectively reproduced for a $MoSe_2$-$WS_2$ heterobilayer.

A less explored family of 2D materials is obtained by self-intercalation, *i.e.* incorporation of native metallic atoms in the van der Waals gap of the pristine layered structure. By adopting an automated workflow, we automatically generate a large number of self-intercalated bilayers (ic-2D) and evaluate their thermodynamic stability, identifying dozens of stable structures that have yet to be explored experimentally. We find that self-intercalation significantly enhances the metallic behaviour, completely eliminating the band gap in most materials that are semiconducting in their pristine form. Additionally, it can introduce a magnetic ground state in otherwise non-magnetic systems. After calculating the hydrogen adsorption energies, we find that the catalytic activity of the ic-2D can be tuned by varying the degree of intercalation. 7 of the newfound materials are predicted to be promising hydrogen evolution reaction catalysts.

The applicability of any material in electrocatalysis is often limited by its tendency to degrade in present of a solvent and electrolytes under applied potentials. Here, we address the problem by presenting a new Pourbaix diagram utility, coded in Python language and openly accessible through the software package ASE. This diagram construction method can directly utilize preexisting experimental or theoretical bulk phase data, without the necessity of performing any DFT calculations. The utility will soon be implemented in the Computational 2D Materials Database (C2DB).

Alternatively, the acqueuos stability problem can be tackled from a microscopic point of view by shifting the focus on the material surface, rather than relying on bulk phase properties. In this thesis, we introduce the concept of Extended Surface Pourbaix Diagram (ESPD). The ESPD expands the capabilities of existing surface Pourbaix diagram methods which aim to predict the status of a material surface in electrochemical environment in terms of coverage by water dissociation products. By including surface vacancies in the list of explored configurations, we are able to explicitly model the material dissolution into ions, completing the list of possible degradation processes. Furthermore, we improve the description of the chemical potential of ions by accounting for the surface excess. The resulting diagrams, calculated herein for a selected set of materials, provide useful mechanistic information on degradation processes and a remarkable agreement with experimental observations.

# Resumé

Siden isolationen af graphene tilbage i 2004 har todimensionale (2D) materialer været på forkanten af materialers forskning både inden for fysik og kemi. Deres fascinerende elektroniske struktur, unikke mekaniske egenskaber og uovertruffen alsidighed har gjort dem til det ideelle grundlag for udforskning af en række anvendelser inden for elektronik, optik, kvanteteknologi, katalyse og mange andre områder. I denne afhandling undersøger vi de elektroniske og katalytiske egenskaber af en bred vifte af 2D-materialer ved hjælp af Density Functional Theory (DFT). Vi viser, hvordan beregningsmetoder kan anvendes for at fremme opdagelsen af nye 2D-materialer, foretage forudsigelser om katalytisk aktivitet, vurdere stabiliteten i vandige miljøer og reproducere fine hybridiseringseffekter.

En af de mest interessante klasser af 2D-materialer repræsenteres af van der Waals heterostructures. Ved at stable forskellige 2D monolayers kan man opnå et næsten uendeligt antal nye hybride strukturer med unikke egenskaber. Disse påvirkes ikke kun af de enkelte lag, men også af deres relative rotationsvinkel, som frit kan justeres takket være layer-layer interaktionernes dispergerende karakter. Her introducerer vi først en gittermatchningsprocedure, der er nødvendig for at generere inputstrukturer af van der Waals heterobilayer til *ab initio* beregninger. Derefter implementerer vi en self-consistent scissors operator, der kan reproducere det quasi-particle elektroniske struktur af store heterostrukturer på bekostning af en PBE beregning. Metoden benchmarkes mod eksperimentelle data, hvilket viser, at twistvinkelafhængige interlagshybridiseringseffekter effektivt kan reproducere for en $MoSe_2$-$WS_2$ heterobilayer.

En mindre udforsket familie af 2D-materialer opnås ved selvinterkalation, dvs. indførelse af native metalliske atomer i van der Waals gap i den rene lagdelte struktur. Ved at bruge en automatiseret arbejdsgang genererer vi automatisk et stort antal selvinterkalerede bilayers (ic-2D) og vurderer deres termodynamiske stabilitet, hvor vi identificerer dusinvis af stabile strukturer, der endnu ikke er blevet udforsket eksperimentelt. Vi finder, at selvinterkalation markant forbedrer den metalliske adfærd og fuldstændigt eliminerer båndgabet i de fleste materialer, der er halvledende i deres rene form. Derudover kan det introducere en magnetisk grundtilstand i ellers ikke-magnetiske systemer. Efter at have beregnet hydrogenadsorptionsenergier finder vi, at den katalytiske aktivitet af ic-2D kan justeres ved at variere graden af selvinterkalation. 7 af de nyfundne materialer forudsiger vi at være lovende katalysatorer til hydrogen evolution.

Anvendeligheden af ethvert materiale inden for elektrokatalyse er ofte begrænset af dets tendens til at nedbrydes i nærværelse af en opløsningsmiddel og elektrolytter under

påtrykte potentialer. Her adresserer vi problemet ved at præsentere et nyt Pourbaix diagramværktøj, kodet i Python sprog og åbent tilgængeligt gennem softwarepakken ASE. Denne diagramkonstruktionsmetode kan direkte bruge eksisterende eksperimentelle eller teoretiske bulkfasedata uden behov for at udføre DFT beregninger. Værktøjet vil snart blive implementeret i Computational 2D Materials Database (C2DB).

Alternativt kan problemet med akvatisk stabilitet tackles fra et mikroskopisk synspunkt ved at skifte fokus til materialets overflade i stedet for at stole på bulkfaseegenskaber. I denne afhandling introducerer vi begrebet Extended Surface Pourbaix Diagram (ESPD). ESPD udvider mulighederne for eksisterende metoder til surface Pourbaix diagrams, som sigter mod at forudsige materialets overfladestatus i en elektrokemisk miljø i form af dækning af vanddissociationsprodukter. Ved at inkludere overfladevacancer i listen over udforskede konfigurationer er vi i stand til eksplicit at modellere materialets opløsning i ioner og fuldføre listen over mulige nedbrydningsprocesser. Derudover forbedrer vi beskrivelsen af ioners kemiske potential ved at tage højde for overfladeoverskuddet. De resulterende diagrammer, der er beregnet her for et udvalgt sæt materialer, giver nyttig mekanistisk information om nedbrydningsprocesser og en bemærkelsesværdig overensstemmelse med eksperimentelle observationer.

# Acknowledgments

On a good day, doing science can make you feel on top of the world. All the pieces come together, on that final plot you see months of hard work summarized in a (way too optimized) selection of data, colors and fonts. Aware that you just added a fundamental piece to the puzzle of the unknown, you celebrate your triumph by ordering Indian take-away.

On a bad day, that voice inside your head remembers you that, all considered, your work is just a drop in the ocean of books, papers, methods, code, theories realized by thousands of scientists before, during and after you (all of them definitely better than you at their job, the voice says).

Given that bad days tend to be much more frequent than the good ones, a Ph.D. can be an incredibly tough test to your mental strength and self esteem. During this experience, I have faced some personal and professional challenges that were completely new to me and often made me doubt whether, after all, I had made the right choice.

Every time I've asked myself this question, I've always found the same answer. Yes, it was worth it. Because science is not what this Ph.D. was all about. Don't get me wrong, having the opportunity to do science at this level is priceless and I'm proud of the results in this thesis. But I have to add that this experience has also given me the chance to surround myself - inside and outside the office - with incredible people that have provided invaluable support and, most importantly, that I've had a lot of fun with. These people are the reason I am still here despite the challenges, and I owe them way more than the few lines of acknowledgments that follow.

First of all, I would like to thank my supervisor, Kristian, for giving me this opportunity in the first place. Our vibrant discussions about reference electrodes and semi-reactions have indeed required an infinite reservoir of patience from both sides. I appreciate that you have always respected my scientific opinion, while at the same time encouraging me to question it (often with good reason, I admit).

Many thanks to Mark for the all the scientific and moral support during the first, delicate half of my PhD. Despite the worrying number of times you have been fired, you are one of the most scientifically talented people I've ever met. Somehow, you also happen to be one of the funniest.

Thanks to Sahar for the additional moral and scientific support. I can't believe I would ever find another color palette nerd like me. As you know, I will always be jealous of

your plants and your plots.

Thanks to the boys Cuau, Casper, Matthew, Julian, Kartik, Dario, Varun and Mikael for the fun times spent together out of the office, exclusively discussing the implementation details of state-of-the-art exchange-correlation functionals and never indulging in frivolous activities.

A special thanks to Jiban. You are not only a colleague, but also a true friend that I can talk to with no filters. Our conversations have really helped me deal with hard times in both research and personal life.

And of course, thanks to the remaining, present and past members of CAMD & staff that I shared my scientific journey with: Mads, Fabian, Thorbjørn, Manjari, Hadeel, Haiyuan, Urko, Sami, Simone, Sami, Pietro, Peder, Joachim, Ask, Martin, Nikolaj, Morten, Asbjørn, Jakob, Fredrik, John, Tara, Sajid, Jens Jorgen, Ole, Lone, Bettina. I sincerely apologize if I missed anyone.

Outside of the office, I would first like to thank all the fellow Campus villagers. Who needs a fancy place when you have a red container and a bunch of nice people? Thanks Subba, Annette, Stella, Zhao, Zeeshan, Braulio, Ruru, Song, Jinwen, Janos, Arvydas, Mostafa, Lea, Hesam. Thanks to my current, lovely roommates Meenakshi, Jay and Omid. It's a true miracle that after all those Catan games we can still talk to each other. Thanks to all of you for being my surrogate family for the past three years.

Un grazie speciale a Mamma, Papa', Nonna Teresa e Nonno Michele per avere sempre supportato le mie scelte, mai negandomi nessuna opportunita'. Perdonate i miei lunghi silenzi, cerchero' di rifarmi nei prossimi mesi. Sappiate che vi voglio un mondo di bene, e sempre ve ne vorro'.

To Javi: since that first meeting in the M container, with masks on our faces a few weeks after my arrival in Denmark, you have been like a brother to me. Thank you for all the fun times, the deep talks, the Indian Fridays, the dinners, the workouts. Past, present and future. You are an absolute science machine and I wish for you all the success you deserve. Also, I'm very impressed with your recent progress with carbonara.

And finally, to Michelle: I cannot even put into words how grateful I am for having spent these last two years in your company. I would have never made it so far without you. You understand me in ways that even I don't understand, and have always been there to help me when I most needed it. Thank you for all the fun, the goofiness, the motivation, the laughter, the tears. You are a rockstar, an artist, a brilliant psychomotor therapist and a great human being. We have shared something unique and I will never forget it.

# List of Publications

(I) S. Americo, S. Pakdel and K. S. Thigesen,
"Functionalised 2D materials: Enhancing metallicity and chemical reactivity *via* self-intercalation" *submitted*, ACS Nano (2023).

Printed in copy in chapter 8.

(II) M. K. Svendsen, S. Americo, A. C. Riis-Jensen, J. J. Mortensen and K. S. Thygesen,
"Ab initio many-body calculations of quasiparticles and excitons in twisted 2D bilayers" *in preparation*.

(III) S. Americo and K. S. Thygesen,
"Extended Surface Pourbaix Diagrams for simultaneous predictions of materials stability and surface coverage in acqueous environment" *in preparation*.

# Contents

# CHAPTER 1

# Introduction

Any object that we can see, touch, smell or taste can be considered as a material, or a collection of materials. One of the fundamental aspects that makes us human is the ability to manipulate and combine the materials found in nature, giving birth to a completely new object: a tool, or device. Devices allow us to perform tasks that are simply impossible to any other species, such as casting light, controlling the temperature, transmitting information, and producing energy.

The efficient construction of a device starts with the appropriate selection of its constituent materials. If a very powerful microscope is focused on a material, we will find that it is composed by a myriad of atoms. Their identity, and the way they are connected to each other, defines the atomic structure. In some substances, few atoms aggregate in small units called molecules. In other cases, they form a rigid network that extends indefinitely in all directions. Atoms are made of positively charged nuclei and negatively charged electrons. A given arrangement of their nuclei in space determines in turn the distribution in space and energy of the electrons, *i.e.* the electronic structure. The combination of atomic and electronic structure is responsible for the entire array of physical and chemical properties of a material.

Experimental methods can probe the electronic structure *e.g.* by applying electric fields or striking the sample with electromagnetic radiation. By measuring how the material responds to such perturbations, they are able to determine whether it is suitable or not for a particular application. On the other hand, the same problem can be approached theoretically by obtaining a model of the atomic structure, and then using powerful computers in order to calculate the electronic structure from first principles, *i.e.* without assumptions derived from external input. Once the electronic structure is known with sufficient accuracy, virtually any property can be predicted, a few examples being the ability to absorb light at specific wavelengths, to respond to magnetic fields and to chemically interact with other species.

One of the properties of our interest in this thesis is the ability of solid materials to facilitate chemical reactions, acting as catalysts. In particular, we focus on electrochemical processes, which involve the transfer of both atoms and electrons and can thus be controlled by means of electric potentials. Batteries are devices where such reactions are performed in order to obtain energy. Electrolyzers can, conversely, provide electric energy in order to realize chemical reactions. In both cases, the target reactions take place on the surface of an electrode that acts as a catalyst. Based on how well the electrode material binds to other species present in the device environment, it can be estimated whether it will efficiently promote the reaction or not. Herein, by means of

first-principles calculations we systematically investigate for a number of materials the catalytic activity towards the hydrogen evolution reaction[1].

Of course, the electrode material can undergo chemical reactions itself. Such processes are facilitated by the same conditions required for the correct functioning of the device, such as the presence of a solvent, ionic species and electric potentials. The undesired outcome is the degradation of the electrode, which compromises its role as a catalyst and thus the performance of the device. One of the main efforts of this thesis is the development of acqueous stability diagrams aimed at predicting the likelihood of such events.

In general, our focus is on the electronic, catalytic and chemical properties of two-dimensional (2D) materials, characterized by a few-atoms thick crystalline structure distributed on a plane. 2D materials can be obtained by mechanically isolating individual "sheets" from other materials that possess a layered structure in bulk phase, or by depositing molecular substances on a substrate and having them react on its surface. A very popular 2D material is graphene, the first 2D material to ever be isolated[2]. More recent examples of 2D materials explored in literature are Transition Metal Dichalcogenides (TMD) monolayers such as $MoS_2$, $WSe_2$ and $NbS_2$[3] and MXenes such as $Ti_3C_2$, $Mo_2C$ and $V_4C_3$[4]. Here we show how such materials can be stacked on top of each other in virtually infinite combinations, thanks to the weak van der Waals (vdW) interactions between the layers. The resulting composite materials, called vdW heterostructures, possess unique properties that combine the ones of the individual components[5]. We introduce a computationally inexpensive method able to capture the electronic hybridization between the layers.

## 1.1 Thesis outline

This Ph.D. thesis is structured as follows:

- In chapter 2, we define the electronic structure problem and describe how it is tackled by Density Functional Theory (DFT), which is the *ab initio* method of choice in this thesis.
- In chapter 3, we provide an extensive introduction about electrochemistry. Starting from the thermodynamics of chemical and electrochemical reactions in equilibrium, we will proceed by describing processes out of equilibrium and, finally, introduce some concepts of kinetics.
- In chapter 4, we will describe the water splitting process and discuss how the concepts from chapter 3 can be utilized to predict the catalytic activity of materials towards its semi-reactions: the Hydrogen evolution reaction (HER) and Oxygen Evolution Reaction (OER).
- In chapter 5, we describe the Pourbaix diagrams construction for predicting the stability of materials in electrochemical environment. Our computer implementation is shown, together with some of its inherent limitations.
- In chapter 6, we introduce the concept of Extended Surface Pourbaix Diagrams (ESPD), which tackles the acqueous stability problem by switching to a microscopic description of the material surface.
- Chapter 7 presents a summary of the main results obtained in this thesis, subdivided by topic.
- Chapter 8 contains the pre-print version of Publication (I) , currently under review.

# CHAPTER 2
# Electronic structure

A large part of this thesis is related to the ability of materials to conduct electricity and engage in chemical interactions. The electric conductivity, chemical reactivity and many other properties of materials are all tightly connected to the electronic structure, which links the arrangement of the atoms in any substance to the energy distribution of the electrons.

Every experimental observation inherently contains information regarding its microscopic origin. However, at present, very few techniques are capable of directly observing the atomic reconfigurations occurring during chemical and physical processes. Over the years, *ab-initio* methods have established themselves as an indispensable tool for supporting experimental observations, whenever a deeper comprehension to the underlying phenomena is needed. Thanks to the constant advancements in computer technologies, a future where material discovery is guided by theoretical predictions is rapidly turning into a present.

Among the many *ab-initio* methods, density functional theory (DFT) constitutes the absolute standard in literature and the method of choice in this thesis. In the following chapter, we will first introduce the electronic structure problem in general and then describe the principles and formalism behind the DFT theory.

## 2.1 The electronic structure problem

All the properties of atomic, molecular and periodic systems are contained in the *wave function* $\Psi$. Once the wave function is known, the value of any physical observable $O$ can be obtained through its expectation value $\langle\Psi|\hat{O}|\Psi\rangle$. Among all observables, the energy plays a major role since it enters the **Schrödinger equation** (SE), at the heart of every *ab-initio* method:

$$\boxed{\hat{H}\Psi(\vec{r},\vec{R}) = E\Psi(\vec{r},\vec{R})} \tag{2.1}$$

$r$ and $R$ represent the coordinates of electrons and nuclei. $\hat{H}$ is the total **hamiltonian** operator and yields the total energy $E$. By using atomic units, we set $e = \hbar = m_e = 1$ and the hamiltonian assumes the following general form:

$$\hat{H} = -\frac{1}{2M_I}\sum_{I=1}^{N}\nabla_I^2 + \sum_{I<J}^{N}\frac{Z_I Z_J}{R_{IJ}} - \frac{1}{2}\sum_{i=1}^{n}\nabla_i^2 + \sum_{i<j}^{n}\frac{1}{r_{ij}} + \sum_{i=1}^{n}\sum_{J=1}^{N}\frac{Z_J}{r_{iJ}} \tag{2.2}$$

where $M$ and $J$ are the nuclear charge and mass. $R_{IJ}$, $r_{ij}$ and $r_{iJ}$ are the nucleus-nucleus, electron-electron and electron-nucleus distances, respectively. The hamiltonian can be rewritten in compact form:

$$\boxed{\hat{H} = \hat{T}_N + \hat{V}_{NN} + \hat{T}_e + \hat{V}_{ee} + \hat{V}_{eN}} \tag{2.3}$$

Where $\hat{T}_N$ and $\hat{T}_e$ are the kinetic energy operators of nuclei and electrons, while $\hat{V}_{NN}$, $\hat{V}_{ee}$ and $\hat{V}_{eN}$ are the nucleus-nucleus, electron-electron and electron-nucleus electrostatic energy operators.

Evaluating these interactions simultaneously in systems containing three or more particles constitutes a so-called **many-body problem**, whose exact solution is impossible. Only approximate solutions to the SE are thus available for any system other than the H atom and its isoelectronic ions.

The first, necessary step towards addressing the many-body problem is to adopt the **Born-Oppenheimer approximation**. Given the large difference between their masses, the relative motion of electrons and nuclei is basically decoupled, since the former will adjust almost instantaneously to a change in the positions of the latter. The electrons can then be seen as moving inside the constant electrostatic potential generated by the nuclei in a fixed configuration. This allows to separate the global wave function into an electronic term $\psi(\vec{r};\vec{R})$ and a nuclear term $\chi(\vec{r};\vec{R})$

$$\Psi(\vec{r};\vec{R}) = \psi(\vec{r};\vec{R})\chi(\vec{R}) \tag{2.4}$$

Where the nuclear coordinates now enter both the wave function and the hamiltonian only parametrically. The electronic and nuclear problem can then be solved independently, with separate Schrödinger equations. The electronic one has the form:

$$\hat{H}^{el}\psi(\vec{r};\vec{R}) = E^{el}(\vec{R})\psi(\vec{r};\vec{R}) \tag{2.5}$$

where the electronic hamiltonian $\hat{H}^{el}$ is expressed as

$$\hat{H}^{el} = \hat{T}_e + \hat{V}_{ee} + \hat{V}_{eN} \tag{2.6}$$

$E^{el}(\vec{R})$ represents the electronic energy for a given configuration of the nuclear coordinates. The total energy can be obtained by summing to it the constant electrostatic potential of the nuclei:

$$E^{tot}(\vec{R}) = E^{el}(\vec{R}) + \sum_{I<J}^{N} \frac{Z_I Z_J}{R_{IJ}} \tag{2.7}$$

If evaluated as a function of the nuclear coordinates, $E^{tot}(\vec{R})$ defines a $3N-$dimensional **potential energy surface** (PES), which constitutes the potential for the nuclear motion and can be used for solving the nuclear SE. The PES is a key object for determining, for instance, the vibrational properties or the equilibrium configuration of an atomic structure.

## 2.2 Density functional theory

Over the years, a large variety of methods has been developed in order to obtain approximate solutions of the Schrödinger equation. The general approach is to define an initial guess of the wave function and then solve the electronic problem iteratively based on the variational principle. These methods are limited by either the large computational demand or the incapacity of fully capturing the electronic correlation effects.

Evaluating the electron-electron potential term in eq. 2.2 constitutes, in itself, a many-body problem. Its exact value includes the electronic exchange and correlation contributions to the energy, which are of quantum-mechanical origin and fundamental for accurate results. The problem can be addressed in a "mean field" fashion (*e.g.* in Hartree-Fock theory) by reducing the $N$-electron many-body problem to a set of $N$ single-particle problems. Each electron is assumed to interact with the average electrostatic potential generated by the other electrons, rather than with each one of them individually. This makes the calculation computationally accessible, although it determines a complete neglect of the correlation effects.

The **Density Functional Theory** (DFT) uses a similar underlying approach, although with important conceptual differences. The main idea is that the wave function, containing $3N$ variables, is a far too complicated object to manipulate directly during electronic structure calculations. The electronic problem can be reformulated in terms of the *electron density*, on object of only 3 variables:

$$n(\vec{r};\vec{R}) = N \int d^3\vec{r}_2 ... \int d^3\vec{r}_N |\psi(\vec{r},\vec{r}_2,...,\vec{r}_N;\vec{R})|^2 \tag{2.8}$$

The $\hat{V}_{eN}$ term in eq. 2.6 can be expressed as a *functional* of the electron density:

$$\hat{V}_{eN}[n] = \int V(\vec{r};\vec{R})\, n(\vec{r};\vec{R})\, d^3\vec{r} \tag{2.9}$$

where $V(\vec{r};\vec{R})$ is the external potential resulting from the electron-nucleus interactions. Since this term is determined by the positions and nature of the nuclei, it is unique of the system under investigation, and so is the hamiltonian where this term appears. The wave function obeys the Schrödinger equation, which is in turn uniquely determined by the hamiltonian.

### 2.2.1 The Kohn-Sham equations

In 1964, Hohenberg and Kohn proved the existence of a unique mapping between the external potential, the wave function and the electron density[6]. Accordingly, the wave function and the total hamiltonian are themselves functionals of the electron density. We then have

$$\hat{H}[n] = \hat{T}[n] + \hat{V}_{ee}[n] + \hat{V}_{eN}[n] \tag{2.10}$$

The electron-electron term still constitutes a complicated object to handle and the origin of the exchange and correlation contributions to the energy. One can imagine to construct an effective non-interacting potential $V_s[n]$ that reproduces the exact energy of the interacting system:

$$E = T[n] + V_s[n] = T[n] + V_{ee}[n] + V_{eN}[n] \tag{2.11}$$

Where $V_s[n]$ has the following form:

$$V_s[n] = V_{eN}[n] + V_H[n] + V_{xc}[n] \tag{2.12}$$

and the corresponding non-interacting hamiltonian is

$$\hat{H}_s[n] = \hat{T}[n] + \hat{V}_s[n] \tag{2.13}$$

The Hartree potential $V_H[n]$ in eq. 2.12 takes into account the electrostatic interactions between electrons in a mean-field fashion. $V_{xc}[n]$ represents the **exchange-correlation functional**, whose form is unknown and has to be approximated. Let us assume that an exact expression for $V_s[n]$ is found: the $N$-electron interacting picture can then be replaced with a fictitious system of $N$ non-interacting electrons, which move in an effective potential that reproduces the exact energy of the interacting system.

The non-interacting wave function $\psi_s$ can be expressed as a Slater determinant of single-particle orbitals $\phi_i(\vec{r})$:

$$\psi_s(\vec{r}_1, ..., \vec{r}_N) = \frac{1}{\sqrt{N!}} \det \begin{pmatrix} \phi_1(\vec{r}_1) & ... & \phi_N(\vec{r}_1) \\ \vdots & & \vdots \\ \phi_1(\vec{r}_N) & ... & \phi_N(\vec{r}_N) \end{pmatrix} \tag{2.14}$$

By inserting eq. 2.14 into the non-interacting SE, one finally obtains a set of one-particle **Kohn-Sham equations**:

$$\left( -\frac{\nabla^2}{2} + v_{eN}(\vec{r}) + v_H(\vec{r}) + v_{xc}(\vec{r}) \right) \phi_i(\vec{r}) = \varepsilon_i \, \phi_i(\vec{r}) \tag{2.15}$$

Where $v_{eN}$, $v_H$ and $v_{xc}$ are the one-particle equivalent of the terms in eq. 2.12. The non-interacting electron density can be easily obtained from the $\phi_i$:

$$n_s(\vec{r}) = \sum_{i=1}^{N} |\phi_i(\vec{r})|^2 \tag{2.16}$$

The total energy obtained by inserting this density in eq. 2.11 represents the energy of the interacting system, which obeys the variational principle. This allows the implementation of DFT in numerical algorithms that solve the Kohn-Sham equations with a self consistent procedure.

### 2.2.2 Approximations to the exchange-correlation functional

The main obstacle towards quantitative predictions from DFT theory is the unknown form of the exchange-correlation (XC) functional contained in eq. 2.12. Over the course of the years, large efforts have been carried by the scientific community in order to obtain different approximations for this essential contribution to the electronic energy. The available expressions of $v_{xc}$ can be ranked in order of increasing accuracy and, accordingly, increasing computational demand.

The first historical attempt of describing electron correlation[7] in DFT is the the *local density approximation* (LDA). The LDA is derived from the study of the ideal model of the homogeneous electron gas (HEG), which consists of an infinite distribution of electrons yielding a constant density $n$, balanced by a positive uniform charge background originated by the nuclei. In practical systems, where the electron density varies in space, the model can be applied locally by approximating every infinitesimal volume element to a HEG of equal density. The LDA functional is relatively straightforward to implement and computationally efficient, making it a useful starting point not only for computationally expensive DFT calculations, but also for the definition of more sophisticated XC functionals.

Significant improvements over the LDA description can be achieved by including the gradient of the electron density in the expression of the XC functional, in the **gener-**

**alized gradient expansion** (GGA). A universal recipe on how to do so is however missing. For this reason, a plethora of GGA functionals are available nowadays, with comparable accuracy although some have been shown to be more suitable for specific classes of materials. GGA functionals are, by far, the most widespread in the scientific community, the most popular example being the Perdew-Burke-Erzenhof functional (PBE)[8]. Their main limitations lie in the poor description of electron localization and the systematic underestimation of the electronic band gap.

A further step in accuracy is achieved with meta-GGA functionals, which include the laplacian of the electron density. State-of-the-art Hybrid functionals incorporate, on top of that, the exact exchange from Hartree-Fock theory. The efficiency of meta-GGA and hybrid functionals starts to become severely affected by the computational cost, which limits their applicability to relatively small systems.

# CHAPTER 3

# General Electrochemistry

The ability of any substance to interact and exchange matter with other substances belongs to the realm of chemistry. In chemistry, we normally associate one or more species which we call reactants with other species, different in nature, called products. The transformation of the former into the latter defines a chemical reaction. When looked at from the atomic scale, chemical reactions are incredibly dynamic processes where atoms are relentlessly exchanged back and forth between reactants and products at an unconceivable speed, from our eyes. On average - and depending on several environmental factors - these reactions choose a specific direction, producing the macroscopic changes that we finally observe.

Alongside with atoms, reactants and products can exchange electrons. These particular processes define the important subclass of electrochemical reactions, which are ubiquitous in nature. They constantly take place in our body, in the earth crust, in plants and algae during photosynthesis. Over the last four hundred years, humans have learned how to harness electrochemical processes in order to convert the energy stored in chemical bonds into electricity, and *vice versa*. The most remarkable outcome of these efforts is the battery, which nowadays powers most of the electronic devices that we are so dependent on.

These achievements wouldn't have been possible without the development of a solid theoretical background defining the discipline of electrochemistry. This incredibly powerful branch of chemistry often discourages students and scholars from delving deeper into it due to its complexity and intricacy. Since a large part of this thesis deals with the study of materials for electrochemical applications, the following chapter is an attempt to ease the reader into the subject. Starting from the very basic thermodynamic principles governing chemical reactions, the treatment is extended in order to describe electrochemical processes for practical applications, with a final overview on the reaction kinetics.

## 3.1 Thermodynamics of chemical reactions

Let us consider a generic chemical reaction of the form:

$$n_A A + n_B B \rightleftharpoons n_C C + n_D D \tag{3.1}$$

Where $n_i$ represents the stoichiometric coefficient of species $i$. The infinitesimal change in the Gibbs free energy of reaction is

$$dG = Vdp - SdT + \sum_i \mu_i dn_i + \sum_i X_i da_i + ... \tag{3.2}$$

Where $\mu_i$ represents the chemical potential of species $i$, $\nu_i$ its stoichiometric coefficient or the number of moles, if molar quantities are used. The $X_i da_i$ and subsequent terms represent the contribution coming from external forces. Typically, chemical reactions are realized at constant pressure and temperature. Hence, 3.2 reduces to:

$$dG = \sum_i \mu_i dn_i + \sum_i X_i da_i \tag{3.3}$$

In common synthesis conditions, there are no external forces acting on the system and the Gibbs free energy change depends uniquely on the chemical potentials $\mu_i$ and the changes in the amounts of reactants and products. The net reaction free energy is given by the finite difference between the free energies of products and reactants:

$$\Delta G = \sum_i \mu_i n_i \tag{3.4}$$

where the $n_i$ coincide with the stoichiometric coefficients in eq. 3.1, taken with positive sign for the products and negative sign for the reactants. The chemical potentials can be expanded in the following way:

$$\mu_i = \mu_i^0 + k_B T \ln a_i \tag{3.5}$$

where $a_i$ represents the **activity** of species $i$ and can be regarded as an "effective concentration" that quantifies its availability for chemical reactions. Assuming that the reaction is performed in a not too concentrated solution, the activity of ionic species can be approximated to their concentration. Solid species and the solvent can be considered at unit activity. $\mu_i^0$ represents the chemical potential of species $i$ in a conventional **standard state** (p=1 bar, T=298.15K, ions at unit activity), therefore the logarithmic term describes the deviation from it due to temperature and activity effects. If molar quantities are used for the chemical potentials, the Boltzmann constant $k_B$ has to be replaced with the gas constant $R = k_B N_{av}$. In the following, however, we will be using atomic units. Eq. 3.4 can now be expanded by using eq. 3.5:

$$\Delta G = \sum_i \mu_i^0 n_i + k_B T \sum_i \ln a_i n_i \tag{3.6}$$

which can be written as

$$\boxed{\Delta G = \Delta G^0 + k_B T \ln Q} \tag{3.7}$$

where the **standard reaction free energy** $\Delta G_0$ collects all the standard chemical potentials and the *reaction quotient* Q gathers all the activities. Any macroscopical chemical reaction is a collection of individual events that can proceed in both directions. Any **spontaneous** reaction will proceed, an average, in the direction that realizes a negative $\Delta G$. The reactants decrease their concentration over time, increasing it for the products. Eventually, the relative concentrations of the species involved reach a value such that no driving force pushes the reaction in either direction: **chemical equilibrium** is reached

$$\begin{aligned} \Delta G = 0 &= \Delta G^0 + k_B T \ln K \\ K &= \exp(-\frac{\Delta G^0}{k_B T}) \end{aligned} \tag{3.8}$$

where $K$ represents the equilibrium constant of the reaction.

## 3.2 The electrical double layer

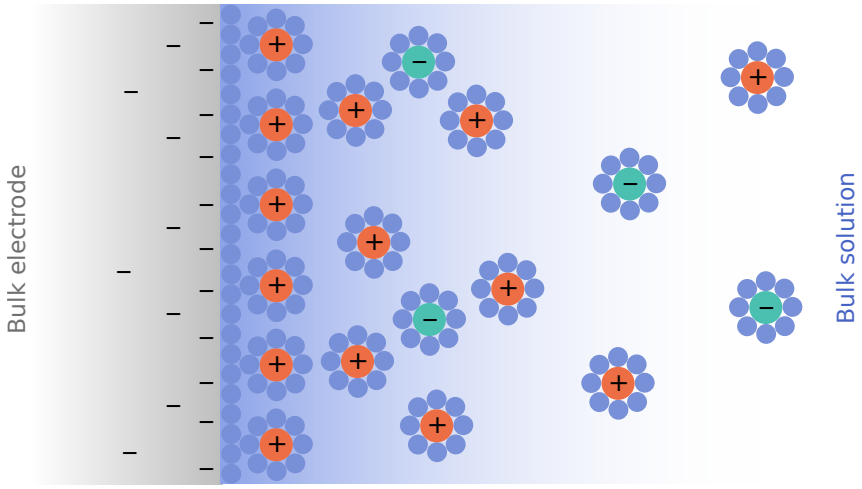


**Figure 3.1:** Graphical representation of the double layer structure. Blue spheres represent the solvent molecules, red spheres positive ions and green spheres negative ions.

Some chemical reactions, called *redox*, involve a net electron transfer between reactants. For instance, during the course of the reaction

$$\mathrm{Zn} + \mathrm{Cu}^{2+} \rightleftharpoons \mathrm{Zn}^{2+} + \mathrm{Cu} \tag{3.9}$$

two electrons are transferred from the electron donor Zn to the electron acceptor $\mathrm{Cu}^{2+}$. The global reaction equation can be decomposed into a **reduction semi-reaction**

$$\mathrm{Zn}^{2+} + 2e^- \longrightarrow \mathrm{Zn} \tag{3.10}$$

and an **oxidation semi-reaction**

$$\mathrm{Cu} \longrightarrow \mathrm{Cu}^{2+} + 2e^- \tag{3.11}$$

as the sum of the two will give back eq. 3.9. If the reactants are directly combined in solution in standard conditions, $\mathrm{Zn}^{2+}$ ions and metallic Cu will be produced while evolving heat.

Alternatively, it is possible to physically separate the two semi-reactions in two different reactors and drive the electrons through an external circuit, leading to the same global reaction. Since the species cannot combine directly, the electron transfer is mediated by two conducting **electrodes** in electrical contact, which may or may not be involved directly in the reaction. In this case, for example, a Zn electrode will dissolve into $\mathrm{Zn}^{2+}$ ions in one half-cell while $\mathrm{Cu}^{2+}$ions will deposit on the Cu electrode in the other half-cell. Otherwise the electrode acts purely as a **catalyst**. The electrode where the reduction reaction occurs is called a **cathode,** the other is called **anode.** Their combination defines an **electrochemical cell.**

The concept of a semi-reaction is purely practical and represents, as the name suggests, only half of the picture when discussing electrochemical reactions. It is indeed possible (as in the example just presented) to make the oxidation and reduction processes happen in two separate regions of space, however they cannot happen *independently.* No chemical processes involve the direct consumption or production of electrons: electroneutrality is preserved only when electrons are transferred from one chemical species to another.

Now, when a metallic electrode is immersed in a solution, an **interface** is created between the surface and the adjacent solvent layer. Due to the anisotropy in the electrostatic forces in proximity of the interface, the charged ions and the dipoles of the solvent molecules assume a different relative orientation and distribution compared to the bulk of the solution. Similarly, the mobile electrons on the electrode surface respond by running towards or away from the surface, altering its charge density. In this region of space, called **electrical double layer**, the charge and molecular distributions are different from the ones in the bulk of the two individual phases. Modeling its structure is complicated, as it is a compromise between electrostatic and dispersion forces in a very heterogeneous and dynamic chemical environment. The relevant aspects for our discussion are:

1. It results in charge separation at the interface. This causes in turn the build-up of a **potential difference** ${}^{M}\Delta^{S}\phi$ between the metallic surface and the solution. In proximity of the surface, this potential difference is in the order of magnitude of few volts. Since the surface atoms and the solvent layer are separated by atomic distances, the gradient of the potential, *i.e.* the electric field, is extremely large ($\sim 10^9$ V cm$^{-1}$) in this region.

2. If the two electrodes are in contact with solutions of dissimilar composition (which is true in any practical application), the structures of the respective double layers are different, hence the ${}^{M}\Delta^{S}\phi$'s. The result is a potential difference across the entire cell, i.e. between the cathode and the anode.

## 3.3 Thermodynamics of electrochemical reactions

The thermodynamic treatment in this scenario has some fundamental differences with respect to the "traditional" way of performing chemical reaction. Since there are now electric fields in the system, the charged particles involved can produce **electrical work** alongside of chemical work. The expression for the reaction Gibbs free energy at constant $T$ and $p$ now becomes:

$$\Delta G = \sum_i (\mu_i + z_i\phi_i)\ n_i \tag{3.12}$$

where $\phi_i$ is the inner potential (or Galvani potential) of the phase where the species is found. It represents the electric potential inside the bulk of a conducting phase. Consequently, $z_i\phi_i$ represents the work required to bring a test charge $z_i$ into the bulk of phase $i$. The two terms in eq. 3.12 can be grouped together in the following way

$$\Delta G = \sum_i \widetilde{\mu}_i\ n_i \tag{3.13}$$

where

$$\boxed{\widetilde{\mu}_i = \mu_i + z_i\phi_i = \mu_i^0 + k_B T \ln a_i + z_i\phi_i} \tag{3.14}$$

is the **electrochemical potential** of the species $i$[1]. Let us discuss the shape of the electrochemical potential for different kinds of species:

[1]Note that we are expressing energies in electronvolts, so we don't have to include the charge explicitly. If we were using molar quantities, for example, we would have

$$\widetilde{\mu}_i = \mu_i + z_i F\phi_i = \mu_i^0 + RT \ln a_i + z_i F\phi_i$$

where $F$ is the Faraday constant, *i.e.* the total charge in a mole of electrons.

- **Solid species** are uncharged and considered at unit activity, hence $\widetilde{\mu} = \mu^0$
- for **solvated ions** with charge $z$ at activity $a$, we have $\widetilde{\mu} = \mu^0 + k_B T \ln a + z\phi_s$, where $\phi_s$ is the inner potential of the solution.
- for **uncharged solvated species** at activity $a$, we have $\widetilde{\mu} = \mu^0 + k_B T \ln a$
- The **solvent** is taken at unit activity. Since it is uncharged, $\widetilde{\mu} = \mu^0$
- For an **electron** in a metal, $\widetilde{\mu}_e = \mu_e^0 - \phi_M$. $\mu_e^0$ represent the chemical potential of an electron at rest in vacuum, which constitutes the reference state of electronic energies and is thus set to zero. The concentration of electrons in a metal doesn't change appreciably during the course of a reaction, hence electrons are considered at unit activity. Thus, $\widetilde{\mu}_e = -\phi_M$, where $\phi_M$ is the Galvani potential of the metal.

By inserting eq. 3.14 into 3.13 we obtain

$$\Delta G = \sum_i (\mu_i^0 + k_B T \ln a_i + z_i \phi_i) n_i \tag{3.15}$$

The first two terms in the summation can be rearranged as in eq. 3.7:

$$\Delta G = \Delta G^0 + k_B T \ln Q + \sum_i z_i \phi_i n_i \tag{3.16}$$

It can be shown that, for a balanced chemical reaction that respects electroneutrality, $\sum_i z_i \phi_i \Delta\nu_i = -n_e U$, where $U = \sum_i \phi_i$ collects all the relevant potential terms and represents the potential difference across the entire cell, leading to

$$\boxed{\Delta G = \Delta G^0 + k_B T \ln Q - n_e U} \tag{3.17}$$

$n_e$ is the number of electrons exchanged in the reaction and has a sign. If positive sign is chosen, then $U = \phi_{anode} - \phi_{cathode}$, otherwise $U = \phi_{cathode} - \phi_{anode}$.

## 3.4 Electrochemical systems in thermodynamic equilibrium

The condition for thermodynamic equilibrium in an electrochemical system is:

$$\Delta G = \sum_i \widetilde{\mu}_i n_i = 0 \tag{3.18}$$

When the condition is satisfied, eq. 3.17 reduces to:

$$\boxed{U_{eq} = U^0 + \frac{k_B T}{n_e} \ln Q} \tag{3.19}$$

Where $U^0 = \Delta G^0/n_e$ represents the potential difference across the cell in standard conditions. Eq. 3.19 is the **Nernst equation** of the cell. In an electrochemical system at equilibrium the net current flow across the cell is zero, meaning that the conversion of reactants into products and the inverse process occur at the same rate.

We now look back at our example, assuming that semi-reactions 3.10 and 3.11 are forced to take place at two separate metal-solution interfaces, and apply the equilibrium conditions to the reduction process:

$$\begin{gathered} \mathrm{Cu}^{2+} + 2e^- \rightleftharpoons \mathrm{Cu} \\ \widetilde{\mu}_{\mathrm{Cu}} - \widetilde{\mu}_{\mathrm{Cu}^{2+}} - 2\widetilde{\mu}_e = 0 \end{gathered} \tag{3.20}$$

Expanding with eq. 3.14 gives

$$\begin{aligned} \mu^0_{\mathrm{Cu}} - \mu^0_{\mathrm{Cu}^{2+}} - k_B T \ln a_{\mathrm{Cu}^{2+}} - 2\phi_S - 2\mu^0_e + 2\phi_M = 0 \\ -2(\phi_M - \phi_S) = \mu^0_{\mathrm{Cu}} - \mu^0_{\mathrm{Cu}^{2+}} - 2\mu^0_e - k_B T \ln a_{\mathrm{Cu}^{2+}} \end{aligned} \tag{3.21}$$

which can be rearranged into

$$-2^M\Delta^S\phi = \Delta G^0_{red} - k_B T \ln a_{\mathrm{Cu}^{2+}} \tag{3.22}$$

where ${}^M\Delta^S\phi = \phi_M - \phi_S$ represents the metal-solution potential difference at the cathode in equilibrium conditions. $\Delta G^0_{red}$ groups all the standard chemical potentials and represents the standard Gibbs free energy change for the reduction semi-reaction. Similarly, the equilibrium condition for the oxidation reaction is:

$$\begin{gathered} Zn \rightleftharpoons \mathrm{Zn}^{2+} + 2e^- \\ \widetilde{\mu}_{\mathrm{Zn}^{2+}} + 2\widetilde{\mu}_e - \widetilde{\mu}_{\mathrm{Zn}} = 0 \\ \mu^0_{\mathrm{Zn}^{2+}} + k_B T \ln a_{\mathrm{Zn}^{2+}} + 2\phi_{S'} + 2\mu^{0'}_e - 2\phi_{M'} - \mu^0_{\mathrm{Zn}} = 0 \\ 2^{M'}\Delta^{S'}\phi = 2(\phi_{M'} - \phi_{S'}) = \Delta G^0_{ox} + k_B T \ln a_{\mathrm{Zn}^{2+}} \end{gathered} \tag{3.23}$$

Here the metal and the solution phase have been marked as $M'$ and $S'$ since they have a different potential and a different composition, respectively, compared to the other electrode. We now sum eqn. 3.22 and 3.23 in order to obtain the global equilibrium conditions:

$$\begin{aligned} -2(\phi_M - \phi_{M'} - \phi_S + \phi_{S'}) = \Delta G^0_{red} + \Delta G^0_{ox} - k_B T \ln \frac{a_{\mathrm{Cu}^{2+}}}{a_{\mathrm{Zn}^{2+}}} \\ -2({}^M\Delta^{M'}\phi - {}^S\Delta^{S'}\phi) = \Delta G^0 + k_B T \ln \frac{a_{\mathrm{Zn}^{2+}}}{a_{\mathrm{Cu}^{2+}}} \\ -2U_{eq} = \Delta G^0 + k_B T \ln \frac{a_{\mathrm{Zn}^{2+}}}{a_{\mathrm{Cu}^{2+}}} \end{aligned} \tag{3.24}$$

Where $\Delta G^0 = \Delta G^0_{red} + \Delta G^0_{ox}$ is the global reaction free energy change and $U_{eq}$ represents the total potential difference across the cell in zero-current conditions. The latter is the combination of the potential difference ${}^{M}\Delta^{M'}\phi$ between the two metallic terminals of the cell and a liquid junction potential ${}^{S}\Delta^{S'}\phi$ between two solutions of dissimilar composition and/or concentration in contact, which give rise to a third interface. We will assume that this potential has been minimized by, e.g., a salt bridge linking the two solutions, such that

$$ {}^{S}\Delta^{S'}\phi \simeq 0 $$

$$ U_{eq} \simeq {}^{M}\Delta^{M'}\phi = \phi_M - \phi_{M'} \tag{3.25} $$

The equilibrium cell potential $U_{eq}$ can be finally obtained by rearranging eq. 3.24 into

$$ U_{eq} = U^0 - \frac{k_B T}{2} \ln \frac{a_{\mathrm{Cu}^{2+}}}{a_{\mathrm{Zn}^{2+}}} $$

Which represents the specific Nernst equation of reaction 3.9.

When two electrode-solution interfaces of dissimilar composition are linked together through a conductor, electrons will spontaneously flow from the electrode sitting at a lower potential towards the one at a higher potential as the reactants are converted into the products. The source of electrons is the oxidized species at the anode, while the electron acceptor is the reduced species at the cathode. This determines an electric current "fueled" by chemical reaction. Batteries (or *galvanic cells*) are devices that take advantage of spontaneous electrochemical processes in order to generate electric energy. Note that if a current spontaneously flows across the system, then the system is *not* in thermodynamic equilibrium. The zero-current equilibrium condition described by the Nernst equation can be practically realized only by external intervention, in two ways:

- by imposing a potential difference equal in magnitude and opposite in sign to the one output by the cell itself though an external power source. This requires withdrawing electrons from the cathode (suppressing the reduction semi-reaction) while pumping them into the anode (suppressing the oxidation), until zero current is measured. A potentiometer will read that the anode is negative while the cathode is positive, since the former has been charged negatively, and the latter positively.
- By coupling the two electrodes through a high-impedance voltmeter, which prevents any appreciable charge transfer. The reading of the voltmeter would be equivalent to the previous case.

We can then say that eq. 3.19 predicts the potential that has to be applied to a cell of a given composition in order to realize the equilibrium (zero-current) conditions or, analogously, the opposite of the potential U output by a cell away from equilibrium. The latter gives the maximum electrical work that can be made by the system if the reaction happens in **reveresible conditions**, i.e. over an infinite amount of time:

$$\Delta G = n_e U \tag{3.26}$$

In real systems, the cell discharges at finite rate and part of this work is lost as heat. The ratio between heat and electrical work is of kinetic origin, and depends on the rate of discharge. If no external potential is applied and current is allowed to pass through the external circuit as in a galvanic cell, electron transfer reactions will work to equilibrate the ${}^{M}\Delta^{S}\phi$ of the two interfaces, altering over time the relative activities of the chemical species and, accordingly, the cell potential. At any time, the reaction can be stopped by opening the circuit or applying an external potential difference, realizing the zero-current conditions described by the Nernst equation (where $Q$ will be different from the initial one). A completely discharged cell is at chemical equilibrium and shows zero potential difference ($U_{eq} = 0$). in these conditions, $Q$ reduces to the equilibrium constant $K$ and the Nernst equation reduces to eq. 3.8:

$$U^0 = -\frac{k_B T}{n_e} \ln K \tag{3.27}$$

## 3.5 The need for a reference electrode

Let us define a general Nernst equation for semi-reactions:

$${}^{M}\Delta^{S}\phi = \phi_M - \phi_S = {}^{M}\Delta^{S}\phi^0 + \frac{k_B T}{n_e} \ln Q \tag{3.28}$$

The absolute electrode potential ${}^{M}\Delta^{S}\phi$ on the left hand side of eq. 3.28 represents the potential difference across an individual metal-solution interface. Unfortunately, this quantity cannot be directly accessed by experiments, as the measuring process requires to introduce a metallic probe into the solution, causing the formation of a second metal-solution interface: the measured potential difference would then be the combination of two metal-solution potential differences.

This limitation can be partially bypassed by coupling the working electrode to an universal reference electrode, whose absolute potential in standard conditions is arbitrarily set to zero. The scientific community adopted the **standard hydrogen electrode (SHE)** as the universal standard. An SHE performs the reversible conversion of protons into gaseous hydrogen:

$$\mathrm{H^+} + e^- \rightleftharpoons 1/2\ \mathrm{H_2}$$

$${}^{M}\Delta^{S}\phi^0\ (\mathrm{SHE}) = 0\ \mathrm{V}$$

The SHE is a platinum electrode in contact with an acidic solution where the $\mathrm{H^+}$ ions have unit activity and $\mathrm{H_2}$ gas at unit fugacity (equivalent of activity for gaseous species) is bubbled. This device can be realized only theoretically, as molecular and ionic interactions in a real solution will cause $\mathrm{H^+}$ activity and $\mathrm{H_2}$ fugacity to deviate

from unity. In practice, a **normal hydrogen electrode (NHE)** is used for the actual measuring process, then the electrode potential relative to the SHE is obtained by extrapolation for an ideal solution and ideal gas. The NHE follows the design principles of the SHE, with the practical difference that the Pt electrode is in contact with a 1 $\mathrm{mol\,l^{-1}}$ HCl or KCl solution where $H_2$ is bubbled at 1 atm pressure.

Since the NHE is an unpractical device to use in routine measurements, other standard, more compact although less robust electrodes such as the saturated calomel electrode (SCE) or the Ag/AgCl electrode are commonly used. The measurements can then be referred back to the SHE scale by accounting for the potential difference between the reference electrode in use and the SHE. Note that an electrode potential tabulated on a reference scale still represents the potential difference measured across a complete electrochemical system, and not an absolute metal-solution potential difference.

## 3.6 Electrochemical systems away from equilibrium

As discussed in section 3.4, the zero-current conditions predicted by the Nernst equation are reached when cathodic and anodic currents at each electrode balance each other, resulting in zero net current flow across the electrochemical cell. We also mentioned that an external power source can be connected to the system in order to reach these conditions, implying that the cell potential can be controlled externally, moving it towards or away from the equilibrium value. Whenever the equilibrium conditions are not met, cathodic currents will prevail at the cathode and anodic currents will prevail at the anode. Let's define a phase-specific **overpotential** $\eta_i$ as the deviation of the absolute potential $\phi_i$ of phase $i$ from its equilibrium value $\phi_{i,eq}$:

$$\eta_i = \phi_i - \phi_{i,eq} \tag{3.29}$$

We can now rewrite eq. 3.12 as

$$\Delta G = \sum_i \mu_i n_i + \sum_i z_i(\phi_{i,eq} + \eta_i)n_i \tag{3.30}$$

As previously seen, the above expression can be rewritten as:

$$\Delta G = \Delta G^0 + k_B T \ln Q - n_e U_{eq} - n_e \eta \tag{3.31}$$

where the cell overpotential $\eta$ represent the deviation of the cell potential from the equilibrium value

$$\eta = \sum_i \eta_i = U - U_{eq} \tag{3.32}$$

Given that $\Delta G^0 + k_B T \ln Q - nE_{eq} = 0$, we are left with

$$\Delta G = -n_e \eta \tag{3.33}$$

As expected, any deviation from equilibrium ($\Delta G \neq 0$) is entirely given by the cell overpotential $\eta$. The sign of the latter controls the sign of the Gibbs free energy change, thus the direction of the reaction. The magnitude of the overpotential determines the rate of the reaction which. As the reaction proceeds, a net **current** flows across the cell. Since the cell is globally electroneutral and the anode provides all the electrons consumed at the cathode, the currents at the individual electrodes have to be equal in magnitude and opposite in sign (the net current flowing from the solution to the anode has the same magnitude as the one flowing from the cathode to the solution). For this reason, it is often sufficient to look at an individual metal-solution interface in order to determine a quantitative overpotential-current relation.

Let us consider a generic one-electron semi-reaction between an oxidized species $O$ and a reduced species $R$:

$$O + e^- \underset{k_{ox}}{\overset{k_{red}}{\rightleftharpoons}} R \tag{3.34}$$

$k_{red}$ and $k_{ox}$ represent the reduction and oxidation rate constants, respectively. At the equilibrium, $k_{red} = k_{ox} = k_{eq}$, with

$$k_{eq} \propto e^{-\Delta G_0^{\ddagger}/k_b T} \tag{3.35}$$

$\Delta G_0^{\ddagger}$ is the **equilibrium activation energy** of the semi-reaction. Out of equilibrium, the activation energies of the reduction and oxidation processes depend exponentially on the overpotential:

$$\Delta G_{red}^{\ddagger} = \Delta G_0^{\ddagger} \, e^{-\beta f \eta} \tag{3.36}$$

$$\Delta G_{ox}^{\ddagger} = \Delta G_0^{\ddagger} \, e^{(1-\beta) f \eta} \tag{3.37}$$

with $f = 1/k_B T$. A positive $\eta$ will lower the chemical potential of the electrons on the left side of eq. 3.34 by an amount $\Delta U = -e\eta$, making the reduction harder and the oxidation easier. The *symmetry factor* $\beta$ quantifies the symmetry of the activation barrier in the energy landscape of the reaction and is equal to 0.5 for a perfectly symmetrical barrier. We can then write $k_{red}$ and $k_{ox}$ as a function of $k_{eq}$:

$$k_{red} = k_{eq} \, e^{-\beta f \eta} \tag{3.38}$$

$$k_{ox} = k_{eq}\, e^{(1-\beta) f \eta} \tag{3.39}$$

The reaction rates for a one-electron transfer reaction with first-order kinetics are

$$\nu_{red}(t) = k_{red}\, a_R(x = 0, t) \tag{3.40}$$

$$\nu_{ox}(t) = k_{ox}\, a_O(x = 0, t) \tag{3.41}$$

where $a_R(x = 0, t)$ and $a_O(x = 0, t)$ are the surface activities ($x = 0$) of the reduced and the oxidized species at time $t$. The total **current density** at the electrode is given by

$$j = ne(\nu_{red} - \nu_{ox}) \tag{3.42}$$

Where $n$ is the number of electrons transferred by the reaction (in our case, $n = 1$). According to this definition, the sign of the current density follows the sign of the overpotential. Eq. 3.43 can be rewritten in terms of equilibrium quantities by combining eqn. 3.38–3.41, leading to the **Butler-Volmer equation**

$$j = j_0 \left[ \frac{a_O(0,t)}{a_{O,bulk}} e^{-\beta f \eta} - \frac{a_R(0,t)}{a_{R,bulk}} e^{(1-\beta) f \eta} \right] \tag{3.43}$$

with the **exchange current density** $j_0$ given by

$$j_0 = e\ k_{eq}\ a_{O,bulk}^{1-\beta}\ a_{R,bulk}^{\beta} \propto e^{-\Delta G_0^{\ddagger}/k_b T}\ a_{O,bulk}^{1-\beta}\ a_{R,bulk}^{\beta} \tag{3.44}$$

$j_0$ is characteristic of each metal-solution interface and is a good measure of the catalytic activity of the electrode material. The Butler-Volmer equation applies to systems where the reaction rate is limited by the kinetics of the electron transfer and not by the transport of species towards and from the electrode, *i.e.* when the reactants are readily available and the products readily leave the electrode surface. Also, the equations above hold quantitatively for one-step, one-electron transfer reactions, but can be extended qualitatively to more complex processes. In general, any electrochemical system at equilibrium will produce an exchange current density, whose magnitude is proportional to the observed current under an applied overpotential.

CHAPTER 4

# Computational electrocatalysis

Nowadays, electrochemical processes constitute a sustainable alternative for the production of chemicals and energy, as well as the conversion of pollutants into valuable products. In recent years, the scientific community to carry out large efforts into either the improvement of existing electrode materials, or their replacement with cheaper, sustainable and more electroactive alternatives.

Searching for new electrode materials experimentally is a laborious process. In absence of an external input, the most time-efficient approach would be to start from an already existing material and modify it by nano-structuring, nano-engineering, alloying, doping and so on[9–12]. Alternatively, it is possible to investigate other materials that belong to the same class, but have not been tested yet for the same application. Although this approach can be adopted successfully, it requires a significant amount of trial-and-error and precludes the possibility of exploring emerging classes of materials for which no previous experimental record is available.

On the other hand, generating atomic structures (or obtaining them from available databases) and calculating their electronic structure by means of *ab-initio* methods takes a fraction of the time. First-principle calculations allow to compute a series of descriptors for the electrocatalytic activity of any given material, whether it has been realized experimentally or its existence has only been theorized. This allows to rapidly explore a large material space and reduce it to a limited set of promising candidates[13–15], whose electrochemical performance can then be evaluated in a laboratory.

In the following, we will first describe the electrochemistry of probably the most relevant electrochemical process in the recent literature: the water splitting reaction. We will then discuss how the catalytic effect of the electrode surface on the hydrogen evolution and oxygen evolution semi-reactions is modeled theoretically, providing simple descriptors that can be utilized for material screening purposes.

## 4.1 Electrochemical water splitting

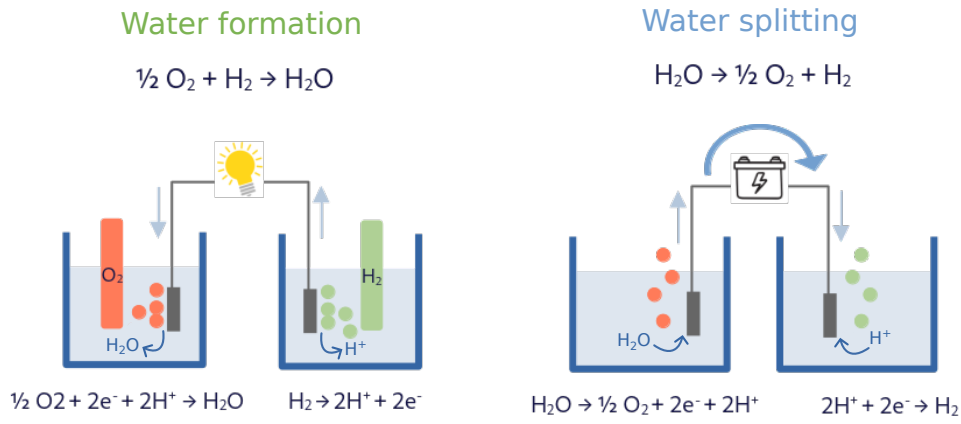


**Figure 4.1:** Graphical representation of the water formation and water splitting processes in an electrochemical setup.

The water formation reaction is defined as:

$$H_2 + 1/2\,O_2 \longrightarrow H_2O \tag{4.1}$$

Since a change in the oxidation state of both $H_2$ and $O_2$ is involved, water formation constitutes an electrochemical reaction which can be split into the two semi-reactions:

$$1/2\,H_2 \longrightarrow H^+ + e^- \tag{4.2}$$

$$1/2\,O_2 + 2H^+ + 2e^- \longrightarrow H_2O \tag{4.3}$$

In standard conditions the process is exoergonic, meaning that the reactions defined so far will spontaneously proceed from left to right. Fuel cells realize $H_2$ oxidation and $O_2$ reduction in an electrochemical setup, taking advantage of the spontaneous water formation in order to produce electric energy[16]. Given the standard equilibrium potential of 1.23 V, the reaction releases 1.23 eV per electron exchanged or, analogously, 2.46 eV per water molecule produced.

As explained in section 3.6, electrical energy can otherwise be externally provided to an electrochemical system in order to control the direction and rate of a reaction. When two metallic electrodes are immersed in water in standard conditions and a potential larger than 1.23 V is applied between the two, the water formation reaction is reversed into the electrolysis of water, alternatively called **water splitting reaction**:

$$H_2O \longrightarrow H_2 + 1/2\,O_2 \tag{4.4}$$

The semi-reaction taking place at the anode is the **oxygen evolution reaction** (OER)

$$H_2O + 2H^+ + 2e^- \longrightarrow 1/2\,O_2 \tag{4.5}$$

And the one at the cathode is the **hydrogen evolution reaction** (HER)

$$H^+ + e^- \longrightarrow 1/2\,H_2 \tag{4.6}$$

The HER in particular is a process of fundamental industrial relevance in modern days. The hazards posed by climate change are pushing more than ever the research towards sustainable energy production and storage. Hydrogen constitutes at the same time a clean fuel, a useful chemical and a potential energy storage vessel.

Nowadays, 96% of the commercial hydrogen is produced from fossil sources, with only the remaining 4% obtained from electrochemical water splitting[17]. The main obstacle towards a more widespread adoption of the latter are the associated costs. Although water splitting may be thermodynamically favourable in certain conditions, the reaction rate, thus the amount of hydrogen produced, is negligible in absence of a proper **catalyst**. Large kinetic barriers affect in particular the OER semi-reaction. The current state-of-the-art HER and OER catalysts are based on noble metals such as Pt, Ir, Ru and Rh or other scarcely available elements (*e.g.* Ni, Co)[18–20], making their cost prohibitive for a large-scale adoption. Less active - although more earth-abundant - alternatives are available[21, 22]. The reduced cost of the electrode material is compensated in this case by the increased energy requirements for reaching overpotentials large enough to observe sufficient hydrogen production.

Finding electrode materials that are both catalytically active and economically inexpensive constitutes a major challenge in the materials science community. Of the most promising approaches towards boosting this search is the computational screening of large material databases. The theoretical models described in the following sections introduce simple descriptors of the HER/OER catalytic activity of a material, which can be obtained by first-principle calculations and used for screening purposes[23].

A simple graphical representation of the water formation and water splitting processes in an electrochemical setup is shown in Fig. 4.1.

## 4.2 The computational hydrogen electrode

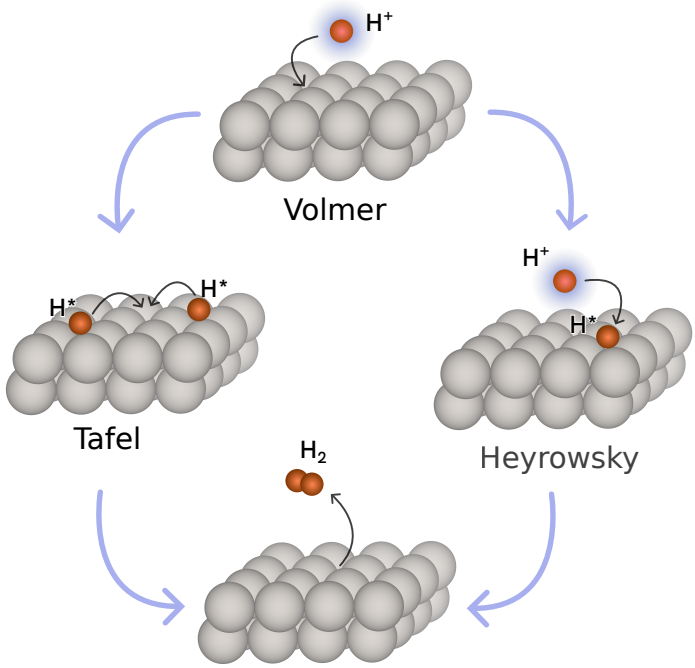


**Figure 4.2:** Mechanism of the hydrogen evolution reaction in presence of an heterogeneous catalyst.

The role of a catalyst in chemical processes is to reduce the kinetic barriers connecting reactants and products, significantly increasing the reaction rate without affecting the reaction thermodynamics. A catalyst does not take part in the reaction directly, meaning that its state before and after the reaction is identical, so that it can be utilized for a virtually infinite number of cycles. The kinetic barriers are lowered by stabilizing transition states and reaction intermediates and/or by providing an alternative reaction pathway with overall faster kinetics. In any case, the catalyst acts as a reaction substrate rather than a reactant.

In presence of a heterogeneous catalyst such as a metallic surface, the hydrogen evolution reaction has been modeled as a two-step process initiated by the **Volmer step**:

$$\mathrm{H}^+ + e^- + * \longrightarrow \mathrm{H}^* \tag{4.7}$$

where $*$ denotes a surface site, and $\mathrm{H}^*$ a hydrogen atom adsorbed on that site. The adsorbed hydrogen can then recombine into a gaseous $\mathrm{H}_2$ molecule in two possible ways:

- In the **Heyrovsky step**, the adsorbed hydrogen reacts electrochemically with a solvated proton:
$$H^* + H^+ + e^- \longrightarrow H_2 + * \tag{4.8}$$
- In the **Tafel step**, two separate adsorbed H atoms combine directly at the surface:
$$2H^* + \longrightarrow H_2 + 2* \tag{4.9}$$

Overall, both steps lead to the same product. The Volmer-Heyrowsky and Volmer-Tafel mechanism, illustrated in Fig. 4.2, thus constitute two competing processes whose relative prevalence over the other can be determined by several experimental factors. Both mechanisms share the Volmer step, which describes the formation of the only reaction intermediate involving the catalyst surface.

### 4.2.1 The activity volcano

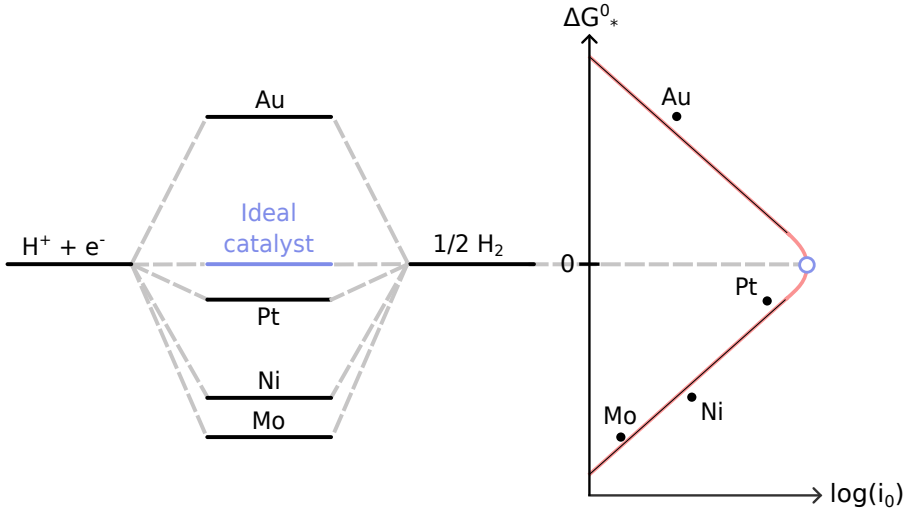


**Figure 4.3:** Mechanism of the hydrogen evolution reaction in presence of an heterogeneous catalyst(b) Qualitative energy diagram of the $\Delta G^0_* = 0$ of different metals, relative to $H^+$ and $H_2$ in standard state. The energies are linked to a qualitative volcano plot, where the red curve represents Parsons' model.

When attempting to predict the performance of a HER catalyst by means of first-principles calculations, it is necessary to link one or more electronic properties of the catalyst to a particular quantity that can be measured experimentally.

From a thermodynamic standpoint, the HER process is determined by the electrochemical reduction of solvated protons into hydrogen described by eq. 4.6. In standard conditions (pH 0, $p(H_2) = 1$ bar) and at $U = 0$ vs. SHE, this process is at equilibrium ($\Delta G^0 = 0$), leading to the equivalence

$$E(\mathrm{H}^+) + E(e^-) = 1/2\ E(\mathrm{H}_2) \tag{4.10}$$

which reduces the Volmer step to:

$$1/2\,\mathrm{H}_2 + * \longrightarrow \mathrm{H}^* \tag{4.11}$$

Back in 1958, Parsons defined a kinetic model for the HER process[24] and found an expression linking the exchange current $i_0$ at the electrode with the Gibbs free energy change $\Delta G^0_*$ of reaction 4.11 (corresponding to the Volmer step in standard conditions):

$$i_0 \propto \left(p^{1/2}_{\mathrm{H}_2} \exp \frac{-\Delta G^0_*}{2k_B T}\right)^{\alpha} \left(1 + p^{1/2}_{\mathrm{H}_2} \exp \frac{-\Delta G^0_*}{2k_B T}\right)^{-1} \tag{4.12}$$

where $\alpha$ is analogous to the symmetry factor described in section 3.6. If plotted against $\Delta G^0_*$, the logarithm of $i_0$ determines a volcano-like curve as illustrated in Fig. 4.3 (red curve). The peak of the volcano is centered around $\Delta G^0_* = 0$, suggesting that the higher catalytic performance is observed for materials that bind hydrogen thermoneutrally. This behaviour is qualitatively described by the **Sabatier principle**: if the adorbate binds too weakly to the substrate, on average it will not stay on the surface long and close enough to undergo chemical reactions. If it binds too strongly, it will not desorb at a fast enough rate to ensure a constant replenishment of the reaction sites.

In the early 2000's, Nørskov and collaborators popularized $\Delta G^0_*$ as the standard descriptor for HER activity predictions in the computational communityi[1]. This quantity can be inexpensively obtained from first-principle calculations:

$$\Delta G^0_* = E^{TOT}(\mathrm{H}^*) - E^{TOT}(*) - 1/2\,E(\mathrm{H}_2) + \Delta E_{ZPE} - T\Delta S \tag{4.13}$$

where $E^{TOT}(\mathrm{H}^*)$ and $E^{TOT}(*)$ are the calculated (usually with DFT) total energies of the material surface including a H adsorbate and of the pristine surface, respectively. The energy of the $\mathrm{H}_2$ molecule $E(\mathrm{H}_2)$ can be obtained either from an *ab-initio* calculation or from thermodynamic data. $\Delta E_{ZPE}$ is the difference in the zero-point energies of products and reactants and, finally, $\Delta S$ is the change in vibrational energy. It it common practice to neglect the contributions to $\Delta S$ from the surface, and to assume that the contribution from the adsorbed hydrogen is small compared to the one from $\mathrm{H}_2$ in gas phase, thus approximating $\Delta S \simeq 1/2\,S^0(\mathrm{H}_2)$

When plotting the $i_0$ against the calculated $\Delta G^0_* = 0$ for a number of metals, Nørskov *et al.* found a good qualitative agreement with Parsons' theoretical predictions[1]. This simple model is often referred to in literature as the **computational hydrogen electrode**, since it links properties that can be calculated from first principles to the experimental activity of HER catalysts.

## 4.3 The computational oxygen electrode

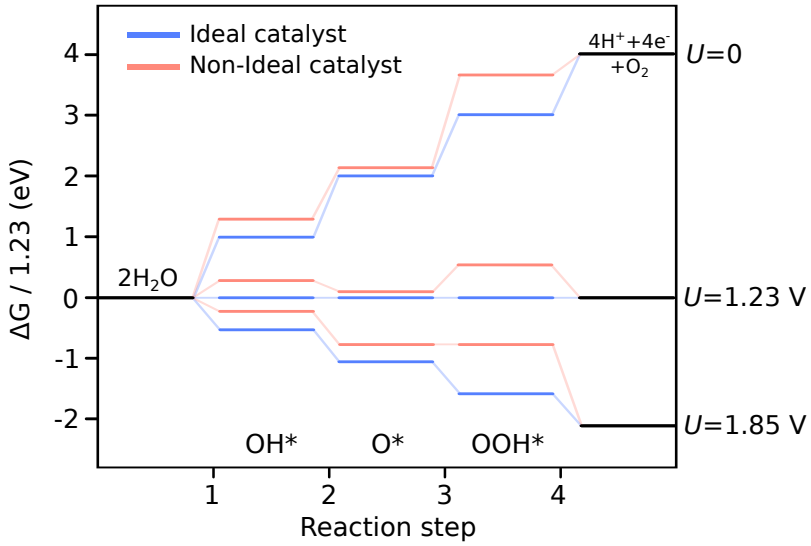


**Figure 4.4:** Energy diagram connecting the OER reaction steps for an ideal catalyst (blue bars) and a non-ideal catalyst(red bars) at applied potentials of 0, 1.23 and 1.85 V. .

Similar considerations to the ones just made for the hydrogen evolution reaction at the cathode can be made for the parallel oxidation process at the anode, the oxygen evolution reaction described by eq. 4.5.

Despite $H_2$ production being the main target of the water splitting reaction, the process is often limited by the OER, a more complex semi-reaction involving a larger number of reaction intermediates. In order to to produce a $O_2$ molecule, two water molecules have to be consumed in a four-electron transfer process. The proposed reaction mechanism in acidic environment is the following[25–27]:

1. Water dissociation on the electrode surface
$$H_2O + * \longrightarrow OH^* + H^+ + e^-$$
2. Dissociation of the OH adsorbate
$$OH^* \longrightarrow O^* + H^+ + e^-$$
3. Formation of the OOH complex
$$H_2O + O^* \longrightarrow OOH^* + H^+ + e^-$$
4. $O_2$ formation
$$OOH^* \longrightarrow O_2(g) + H^+ + e^-$$

The energetics of steps 1-4 are evaluated by modeling the atomic structures of the different surface-adsorbate complexes and obtaining separate Gibbs equations similar to eq. 4.13:

$$\Delta G_{(1)} = E^{TOT}(\mathrm{OH}^*) - E^{TOT}(*) + 1/2\, E(\mathrm{H_2}) - E(\mathrm{H_2O}) + \Delta E_{ZPE} - T\Delta S \quad (4.14)$$

$$\Delta G_{(2)} = E^{TOT}(\mathrm{O}^*) - E^{TOT}(\mathrm{OH}^*) + 1/2\, E(\mathrm{H_2}) + \Delta E_{ZPE} - T\Delta S \quad (4.15)$$

$$\Delta G_{(3)} = E^{TOT}(\mathrm{OOH}^*) - E^{TOT}(\mathrm{O}^*) + 1/2\, E(\mathrm{H_2}) - E(\mathrm{H_2O}) + \Delta E_{ZPE} - T\Delta S \quad (4.16)$$

$$\Delta G_{(4)} = E^{TOT}(\mathrm{O_2}) - E^{TOT}(\mathrm{OOH}^*) + 1/2\, E(\mathrm{H_2}) + \Delta E_{ZPE} - T\Delta S \quad (4.17)$$

As in the computational hydrogen electrode, at $U$=0 vs. SHE the equivalence 4.10 can be utilized. The sum of steps 1-4 leads yields the chemical equation and the Gibbs free energy of the OER:

$$2\,\mathrm{H_2O} \longrightarrow \mathrm{O_2}(g) + 4\,\mathrm{H^+} + 4\,e^-$$

$$\Delta G_{OER} = \sum_{i=1,2,3,4} \Delta G_{(i)} = 4e\, U^0_{\mathrm{O_2/H_2O}} = 4.96 \text{ eV} \quad (4.18)$$

Where $U^0_{\mathrm{O_2/H_2O}} = 1.23$ V is the standard electrode potential of the oxygen reduction reaction (inverse of the OER). As expected, the OER is uphill in energy at $U$=0 vs. SHE, meaning that in order to make the process spontaneous the potential of the OER electrode has to be raised above the SHE potential by an amount

$$U = U^0_{\mathrm{O_2/H_2O}} + \eta \quad (4.19)$$

Where $\eta$ is the overpotential. By neglecting the reaction kinetics - or, equivalently, by assuming that the kinetics barriers are small - the OER is limited only by the thermodynamic barriers connecting steps 1-4, represented by the $\Delta G_{(i)}$. Accordingly, the overpotential of the complete reaction is given by:

$$\eta = -\frac{1}{e} \max_i \Delta G_{(i)} - U^0_{\mathrm{O_2/H_2O}} \quad (4.20)$$

When this overpotential is applied to the OER electrode on top of $U^0_{\mathrm{O_2/H_2O}}$, all the reaction steps presented above are downhill in energy. The ideal OER catalyst has $\eta$=0, which according to eq. 4.20 can be obtained only if $\Delta G_{(i)}$=1.23 eV for all the individual reaction steps. Fig.4.4 shows the energy diagram of the OER, subdivided in its individual reaction steps, for an ideal and a non-ideal catalyst. At $U$>1.23 V ($\eta$=0 V), all the reaction steps become downhill in energy for the ideal catalyst. The potential has to be raised above 1.85 V ($\eta$=0.65 V) in order to achieve the same result for the non-ideal catalyst.

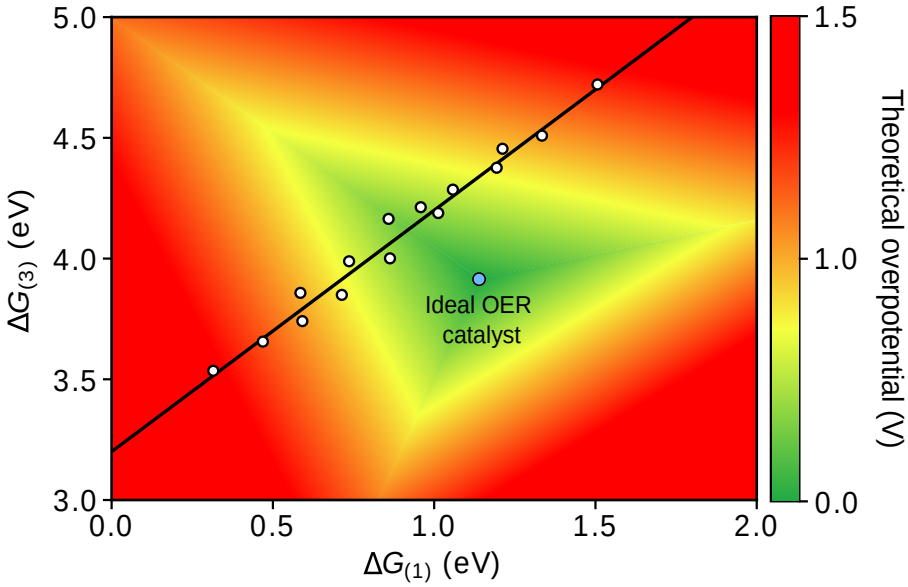


**Figure 4.5:** Qualitative volcano plot showing the scaling relation in eq. 4.21 (black line). The points represent the qualitative behaviour of different materials and do not correspond to real data. The colormap shows the theoretical overpotential .

### 4.3.1 scaling relations

The ideal scenario just presented is, in practice, virtually impossible to obtain. The $\eta$=0 condition can be realized only for a catalyst able to optimally stabilize all the reaction intermediates independently. What is instead commonly observed in heterogeneous catalysis is that the relative energies of the O, OH and OOH adsorbates are linearly dependent on each other in the so-called **scaling relations**. For example, on (111) and (100) surfaces of fcc metals the reaction steps (1) and (3) universally satisfy the relation

$$\Delta G_{(3)} = \Delta G_{(1)} + 3.2 \pm 0.02 \text{ eV} \tag{4.21}$$

These scaling relations never cross the activity optimum predicted by combining eqn. 4.14 - 4.17, as illustrated by Fig. 4.5. Even an optimal catalyst under such restrictions would have a theoretical overpotential of 0.3-0.4 V[28].

Furthermore, some of the best OER catalysts according to theoretical predictions are susceptible to oxidative degradation processes at the relatively large potentials required by the reaction. For this reason, the current state-of-the-art OER catalysts are metal oxides which combine reasonably low overpotentials, high current densities and good thermodynamic stability[29]. Finding electrode materials able to escape the scaling relations and realize the zero overpotential conditions would mark a milestone in electro-

catalysis and a significant stride towards the large-scale hydrogen production through water splitting.

# CHAPTER 5

# Pourbaix Diagrams

In a practical electrochemical setup, a particular electron transfer reaction between two redox couples is performed, without involving the electrode material or other species that may be present in the environment. Unfortunately, electrode materials that are thermodynamically stable in working conditions are relatively rare, as most of them are susceptible to corrosion and passivation in acidic or alkaline solutions under applied potentials.

Almost all electrode materials contain metallic elements that can be transferred to the solution by conversion into solvated (usually ionic) species. It is also possible for the electrode surface to become passivated by an oxide layer which can inactivate or significantly slow down electron transfer processes. The likelihood of these events depends on the tendency of the material to bind molecular and ionic species, its tendency to dissolve and, in general, the relative stability of the material and its degradation products.

The Nernst equation provides a convenient way to assess the stabilty domain of different species as a function of the pH of the solution and the applied potential. The resulting potential-pH diagrams are nowadays named after Marcel Pourbaix who, with collaborators, carried out the monumental effort of collecting thermochemical data and calculating potential-pH diagrams for all the metallic elements in his *"Atlas of electrochemical equilibria in acqueous solution"* (1966)[30]. The original formulation is purely based on considerations about electrochemical equilibrium, where the Nernst equation applies.

If interpreted correctly, potential-pH diagrams provide a surprising amount of information about the qualitative behaviour of materials in electrochemical environment. Pourbaix elegantly used them in order to not only comment on the stability of metals, but also relate his observations to industrially relevant phenomena such as corrosion and passivation.

In the right hands, the diagrams constitutes a powerful tool. However, their purely thermodynamic description comes with several limitations that the user must be aware of. These will be discussed later in this chapter. As stated by Pourbaix himself in the *atlas*:

> "*...We cannot insist too much on the fact that the equilibrium diagrams discussed here can only, by themselves, solve a very limited number of problems...They are only tools at the disposal of the electrochemist and they*

> *must always be used in conjunction with other means of investigation...A bright future can be predicted for groups of investigators who are competent at the same time in thermodynamics, kinetics, and physics and physical chemistry of metals.*"

In the following, we will discuss the theoretical principles behind the construction of Pourbaix diagrams. Starting with the original formulation, we will then describe our implementation into the Atomic Simulation Environment (ASE)[31].

## 5.1 The original formulation

Potential-pH diagrams were originally aimed at predicting stable electrocatalysts for applications such as the electrochemical water splitting. Due to their generality, their scope was rapidly extended to other technologically relevant problems involving the electrochemistry of electrode surfaces, such as corrosion, passivation and electrodeposition.

The original diagram construction was meant to assess the acqueous stability of metallic elements and their reduced/oxidized forms based on fundamental principles of electrochemistry. Given a target electrode material, a list of known solid and ionic compounds containing its compositional elements is laid out. Then, the user determines all the possible chemical reactions between these compounds, evaluates the equilibrium conditions and compares them in order to define their stability domains. Since the reactions are assumed to take place in acqueous environment, the species can exchange oxygen and hydrogen with the surrounding solution in the form of $H_2O$, $OH^-$ ions and $H^+$ ions. However, as explained later in these chapter (section 5.1.3), including $OH^-$ explicitly is not necessary. The availability of $H^+$ is regulated by the pH:

$$\mathrm{pH} = -\log a_{\mathrm{H}^+} \tag{5.1}$$

We now define a general semi-reaction in acqueous environment at equilibrium:

$$aA + n_w \mathrm{H_2O} + n_h \mathrm{H}^+ + n_e e^- \rightleftharpoons bB \tag{5.2}$$

Where the coefficients of $H_2O$, $H^+$ and electrons can be positive or negative depending on their role as a reactant or product, respectively. The corresponding Nernst equation is

$$\Delta\phi_{eq} = \Delta\phi^0 + \frac{k_B T}{n_e}(n_w \ln a_{\mathrm{H_2O}} + n_h \ln a_{\mathrm{H}^+} + a \ln a_A + b \ln a_B) \tag{5.3}$$

where $\Delta\phi$ represents a metal-solution potential difference. In order to describe a complete electrochemical process while still keeping the focus on the target interface, the contributions from the counter electrode have to be included.

For simplicity, in the following derivation we will adopt the standard hydrogen electrode (SHE) as the counter electrode. By construction, the SHE metal-solution potential is identical at any pH and conventionally set to zero, hence any contribution from the SHE to the cell potential $U$ drops:

$$U_{eq} = \Delta\phi_{eq} + \Delta\phi_{SHE} = \Delta\phi_{eq} \tag{5.4}$$

Accordingly, eq. 5.3 now describes the equilibrium potential of a complete electrochemical system. By switching to base-10 logarithms and grouping the activity terms ($H^+$ excluded) into $Q^{'} = \prod_{i \neq H^+} a_i^{n_i}$ we obtain

$$\boxed{U_{eq} = U^0 + \frac{\alpha}{n_e}(Q^{'} - n_H \text{ pH})} \tag{5.5}$$

with $\alpha = k_B T \ln 10 = 0.059$ V at T=298.15 K. Note that the solvent and the solid phases are considered at unit activity (see section 3.3), hence the only relevant terms in $Q^{'}$ are the ones related to the solvated species. The activity of the latter is arbitrary and is set to a value (typically $10^{-6}$) that defines the presence of the species in a small, although measurable, amount.

### 5.1.1 Definition of the standard chemical potentials

The standard cell potential is defined as

$$U^0 = 1/n_e \sum_i \mu_i^0 = \Delta G^0 / n_e \tag{5.6}$$

Where the standard chemical potential $\mu_i^0$ of a given species can be seen as a measure of the energy stored in its chemical bonds. This quantity can only be expressed on a relative scale and several choices, such as the sum of the bond enthalpies or the internal energy, are viable options. Conventionally, the chemical potential of elements in their standard state is set to zero. In this case the definition of the chemical potential becomes equivalent to a **formation enthalpy**. Formation enthalpies have been directly measured for a large amount of compounds, and can be obtained indirectly from electrochemical measurements when not available. For instance, standard electrode potential values can be used in order to determine the chemical potentials of two key species for the establishment of Pourbaix diagrams: $H_2O$ and $H^+$.

The reaction of formation of water, i.e. the inverse of the water splitting reaction

$$H_2 + 1/2\ O_2 \longrightarrow H_2O$$

involves an exchange of two electrons and can be performed electrochemically. In standard conditions, the measured cell potential versus SHE (reported as $\phi_{cathode} - \phi_{anode}$, hence $n_e = -2$) is 1.23 V. By expanding it as in eq. 5.6 we obtain

$$\Delta G^0 = -2(\mu^0_{H_2O} - \mu^0_{H_2} - 1/2\mu^0_{O_2}) = -2U^0 = -2.46 \text{ eV} \tag{5.7}$$

Since $H_2$ and $O_2$ are elemental substances in their standard state, we have $\mu^0_{H_2} = \mu^0_{O_2} = 0$, which means

$$\mu^0_{H_2O} = -2.46 \text{ eV}$$

The chemical potential of solvated protons can be obtained in a similar way. The reversible conversion of protons into gaseous hydrogen performed by the SHE defines the zero of the relative potential scale:

$$H^+ + e^- \rightleftharpoons 1/2\ H_2$$

$$\delta G^0 = 1/2\mu^0_{H_2} - \mu^0_{H^+} - \mu^0_e = 0 \tag{5.8}$$

where $\delta G^0$ denotes the standard free energy of a semi-reaction. Again, since $\mu^0_{H_2} = \mu^0_e = 0$, we have

$$\mu^0_{H^+} = 0 \text{ eV}$$

### 5.1.2 Diagram construction

Having all the ingredients necessary to define an equilibrium potential, an expression of the form of eq. 5.5 is obtained for every possible reaction pathway between the available phases, leading to a set of equilibrium lines that can be drawn on a potential-pH coordinate system. Every oxidation process is thermodynamically allowed at potentials above the corresponding equilibrium line, and *vice versa* for reduction processes. This allows one to define stability domains for all the considered phases.

As an example, we now apply the procedure described so far in order to obtain the Pourbaix diagram of lithium, where we consider three phases of different oxidation states (OS): metallic Li (OS=0), lithium hydride LiH (OS=−1) and $Li^+$ (OS=+1). We now write down the possible equilibria:

(i) $-1 \longrightarrow 0$

$$LiH \rightleftharpoons Li + H^+ + e^-$$

$$U_{eq} = 0.726 \text{ V} - \alpha \text{ pH}$$

(ii) $-1 \longrightarrow +1$

$$LiH \rightleftharpoons Li^+ + H^+ + 2e^-$$

$$U_{eq} = -1.16 \text{ V} - \alpha/2 \text{ pH} + \alpha/2 \log a_{Li^+}$$

(iii) $0 \longrightarrow +1$

$$Li \rightleftharpoons Li^+ + e^-$$

$$U_{eq} = -3.05 \text{ V} + \alpha \log a_{Li^+}$$

The equilibrium lines have been plotted in Fig. 5.1a. In order to construct the final diagram, the following considerations have to be made:

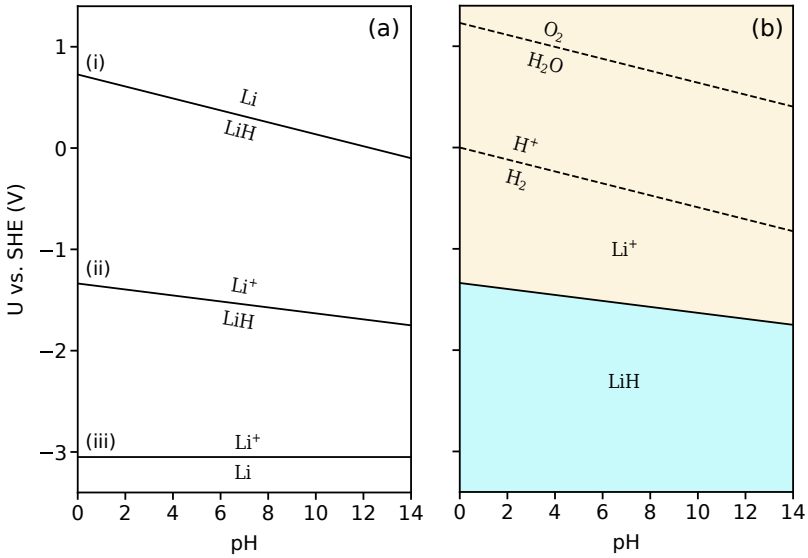


**Figure 5.1:** a) Equilibrium potentials for reactions (i), (ii) and (iii) described in section 5.1. Above and below each line are reported the stable phases at potentials higher and lower than the equilibrium value. b) Pourbaix diagram of Li, with the stability domain of water superimposed. .

- At potentials below line (i), LiH is more stable than metallic Li
- At potentials above line (ii), $Li^+$ is more stable than LiH, and *vice versa*.

By combining the two, the stability domains of the considered species can finally be drawn, as seen in Fig. 5.1b. It turns out that metallic Li is not stable at all in acqueous environment. This is an expected conclusion, as it is known that when alkali metals are immersed in an acqueous solution they react violently with water, with production of hydrogen.

Note that the working electrode is always in contact with the solvent, which provides a constant supply of $H^+$ and $H_2O$. This means that an applied potential against the SHE may trigger hydrogen evolution at the working electrode. When building Pourbaix diagrams, it is customary to superimpose the stability domain of water, comprised between the equilibrium lines - shown in Fig. 5.1b - of the hydrogen evolution reaction (HER):

$$\begin{aligned} \mathrm{H}^+ + e^- &\longrightarrow 1/2\ \mathrm{H}_2 \\ U_{eq} &= -\alpha\ \mathrm{pH} \end{aligned} \tag{5.9}$$

and the oxygen evolution reaction (OER):

$$\mathrm{H_2O} \longrightarrow 1/2\ \mathrm{O_2} + 2\ \mathrm{H^+} + 2e^-$$
$$U_{eq} = 1.23 - \alpha\ \mathrm{pH} \tag{5.10}$$

At any potential lower than eq. 5.9, The working electrode will convert $H^+$ into $H_2$ while the SHE realizes the inverse reaction. At potentials higher than eq. 5.9 and lower than 5.10, the working electrode and the SHE would swap roles, in principle. In practice, unless the working electrode is supplied by $H_2$, none of the above semi-reactions can take place. When the potential is raised above eq. 5.10, the working electrode spontaneously evolves oxygen through the OER while the SHE performs the HER (hence, globally, the water splitting reaction takes place). Consequently, the region of the potential-pH diagram comprised between the equilibrium lines defined by eq. 5.9 and 5.10 determines the stability domain of $H_2O$.

### 5.1.3 Thermodynamic equivalence of acidic and alkaline reactions

In our definition of a generic electrochemical reaction (eq. 5.2), only the protons $H^+$ were included explicitly. One may argue that, when describing reactions taking place at pH larger than 7, $OH^-$ ions will be the prevailing acqueous ion in solution and the preferred species to be consumed as a reactant or generated as a product.

This is conceptually correct. However, we will now show how the chemical potentials of $H^+$, $OH^-$ and $H_2O$ are linked to each other in a way such that it makes no practical difference, from a thermodynamic standpoint, to replace protons with $OH^-$ when evaluating reaction energetics.

We start by writing down the water dissociation reaction at equilibrium:

$$\mathrm{H_2O} \rightleftharpoons \mathrm{H^+} + \mathrm{OH^-}$$
$$\mu^0_{\mathrm{H_2O}} = \mu^0_{\mathrm{H^+}} + \mu^0_{\mathrm{OH^-}} + \alpha \log(a_{\mathrm{H^+}} a_{\mathrm{OH^-}}) \tag{5.11}$$

At equilibrium, the activity of $H^+$ and $OH^-$ are connected through the water dissociation constant:

$$K_w = a_{\mathrm{H^+}} a_{\mathrm{OH^-}} = 10^{-14}$$
$$\mathrm{pH} + \mathrm{pOH} = 14 \tag{5.12}$$

and eq. 5.11 can be rearranged into

$$\mu^0_{\mathrm{H_2O}} = \mu^0_{\mathrm{H^+}} + \mu^0_{\mathrm{OH^-}} - 14\alpha \tag{5.13}$$

Since $\mu^0_{\mathrm{H^+}} = 0$ eV, and $\mu^0_{\mathrm{H_2O}} = -2.46$ eV (see section 5.1.1), we obtain

$$\mu^0_{\mathrm{OH^-}} = \mu^0_{\mathrm{H_2O}} + 14\alpha = -1.632 \text{ eV} \tag{5.14}$$

We now define a generic oxidation semi-reaction in acidic environment:

$$A + n_w H_2O \longrightarrow B + n_h H^+ + n_e e^- \tag{5.15}$$

Any acidic semi-reaction can be converted to its alkaline equivalent by summing the water dissociation reaction $n_h$ times in the direction that cancels out the contribution from the protons:

$$n_h H^+ + n_h OH^- \longrightarrow n_h H_2O \tag{5.16}$$

So that the sum of reactions 5.15 and 5.16 still corresponds to the oxidation of $A$ into $B$, although this time in alkaline conditions:

$$A + n_h OH^- \longrightarrow B + n_e e^- + (n_h - n_w) H_2O \tag{5.17}$$

The overall reaction free energy corresponds, accordingly, to the sum between the contributions from reaction 5.15 and reaction 5.16, the latter being:

$$\begin{aligned} \Delta G_w &= n_h(\mu^0_{H_2O} - \mu^0_{OH^-} + \alpha \mathrm{pH} + \alpha(14 - \mathrm{pH})) \\ &= n_h(\mu^0_{H_2O} - \mu^0_{OH^-} + 14\alpha) \end{aligned} \tag{5.18}$$

Expanding $\mu^0_{OH^-}$ as in eq. 5.14 yields

$$\Delta G_w = 0$$

determining the equivalence of reactions 5.15 and 5.17 . In other words, converting any acidic semi-reaction into its alkaline equivalent comes at no cost on the free energy, hence explicitly considering $OH^-$ ions at alkaline pH values is not necessary. The pH term in the Gibbs equation automatically accounts for the abundance of $H^+$ at low pH and their scarcity at high pH, and *vice versa* for $OH^-$. It is therefore possible to obtain complete Pourbaix diagrams by only considering reaction pathways that involve consumption or production of protons.

Note that no information of kinetic nature has been provided so far. Despite the equivalence from a thermodynamic standpoint, acidic conditions may provide faster reaction kinetics than alkaline conditions - or *vice versa* - depending on the nature of the electrode material, the presence of electrolytes, the applied potential and the temperature. Accounting for such effects is beyond the scope of Pourbaix diagrams, which rely on a purely thermodynamic description.

## 5.2 Implementation into ASE

The compilation of the *atlas* was a significant advancement in the field of corrosion science and electrochemistry, establishing Pourbaix diagrams as an essential tool for understanding corrosion mechanisms, designing corrosion-resistant materials and evaluating the performance of protective coatings. Furthermore, the large amount of data collected in the process makes the *atlas*, to date, one of the most valuable sources of experimental formation energies of acqueous ions and solid materials for the scientific community.

Nevertheless, the manual construction of the diagrams was a laborious process that required a significant amount of time and effort. Nowadays, large material databases collecting structural and thermodynamic properties are digitally accessible. Experimental databases include the Inorganic Crystal Structure Database (ICSD)[32], the Crystallography Open Database (COD)[33] and the NIST WebBook[34]. Properties predicted through *ab-initio* methods can be found *e.g* in the Open Quantum Materials Database (OQMD)[35], the Materials Project Database[36] and the Computational 2D Materials Database (C2DB)[37, 38]. As seen in the previous section, the formulation of Pourbaix diagrams is based on simple thermodynamic principles and, with few modifications, can be automated. An example is the Materials Project Pourbaix diagram utility[39]. One of the main efforts of this Ph.D. project has been the implementation of the method into the ASE software package[31], with the initial goal of assessing the acqueous stability of the two-dimensional materials collected in C2DB. In this section, we will first discuss the thermodynamic background, and then proceed towards the details of our implementation. A final section discusses some limitations and *caveats* that have to be taken into account when interpreting acqueous stability diagrams.

### 5.2.1 Thermodynamic background

As seen in section 5.1, potential-pH diagrams can be obtained starting from the Nernst equation, describing the equilibrium potential of redox processes in thermodynamic equilibrium. We will shift our focus on the more general Gibbs equation, that applies both in equilibrium and non-equilibrium conditions. The pH and potential dependence can be made explicit in the following way:

$$\boxed{\Delta G = \Delta G^0 + \alpha \log Q' - n_h \alpha \text{ pH} - n_e U} \tag{5.19}$$

Where $U$ represents the potential difference between the working electrode and the reference electrode. At the equilibrium, $\Delta G = 0$, $U = U_{eq}$ and eq. 5.19 reduces to eq. 5.5.

Let us look again at the general semi-reaction:

$$aA + n_w \mathrm{H_2O} + n_H \mathrm{H^+} + n_e e^- \rightleftharpoons bB + ... \tag{5.20}$$

In our formulation, species $A$ is always the electrode material (which will often be referred to as the *target* material), while the main product(s) is one or more reduced/oxidized forms such as an oxide, a hydride, an ion. Since we aim to extend the method beyond metallic elements, the number of products depends on the stoichiometry of the electrode material, so that the reaction is correctly balanced. For instance, every reaction pathway of $MoS_2$ has to include a Mo-containing species such as $MoO_2$ and a S-containing species such as $HSO_4{}^-$.

Once all the reactions between the target material and the possible decomposition products have been laid out, their associated free energy changes $\Delta G_i$ can be computed as in eq. 5.19 at any point in the potential-pH space. This allows to simultaneously determine the most stable phase in a given region of the diagram (*i.e.* the one associated to the lowest $\Delta G$) and determine the energy of the target material relative to this phase, which we call *Pourbaix energy* $\Delta G_{pbx}$:

$$\Delta G_{pbx}(\mathrm{pH}, U) = -\min_i \Delta G_i(\mathrm{pH}, U) \tag{5.21}$$

The special case where the target material $T$ does not undergo any reaction defines the zero of the energy scale:

$$T \longrightarrow T$$
$$\Delta G = 0 \tag{5.22}$$

The reactions with positive $\Delta G$ cannot proceed in the direction that causes the decomposition of the target material and are automatically discarded. If, in a given region, $\Delta G > 0$ for all the decomposition pathways, then $\Delta G_{pbx} = 0$ and the target material can be considered as thermodynamically stable.

As previously stated, no reaction kinetics are explicitly taken into account. Nevertheless, as discussed in section 3.6, reactions with small $\Delta G$ are associated to a small overpotential $\eta$:

$$\Delta G = -n_e \eta \tag{5.23}$$

Given the exponential dependence of the current density $j$ on the overpotential described in eq. 3.43, it is reasonable to assume that reactions producting a small free energy change[1] will proceed at a negligible rate. Thus, a threshold can be set on $\Delta G_{pbx}$ in order to define a metastability region for the target material.

Note that this formulation of the diagram is formally equivalent to the original one. Let us define, again, the Pourbaix diagram of Li, this time with the current formulation. We now consider metallic Li as the target material, which can decompose into the two products LiH and $Li^+$, defining a set of two equations:

(i) $\mathrm{Li} \longrightarrow \mathrm{LiH}$

$$\mathrm{Li} + \mathrm{H}^+ + e^- \longrightarrow \mathrm{LiH}$$
$$\Delta G_1 = -0.726\ \mathrm{V} + \alpha\ \mathrm{pH} + U$$

[1] Or even large $\Delta G$, provided that the exchange current density $j_0$ is small.

(ii) $\mathrm{Li} \longrightarrow \mathrm{Li}^+$

$$\mathrm{Li} \longrightarrow \mathrm{Li}^+ + e^-$$
$$\Delta G_2 = -3.05\ \mathrm{V} + \alpha \log a_{\mathrm{Li}^+} - U$$

Reaction (i) will proceed towards the formation of LiH ($\Delta G < 0$) when

$$U < 0.726 - \alpha\ \mathrm{pH}$$

and reaction (ii) will proceed towards the formation of $\mathrm{Li}^+$ when

$$U > 3.05 - \alpha \log a_{\mathrm{Li}^+}$$

It can already be seen that there is no region where metallic Li is thermodynamically stable ($\Delta G > 0$ for both reactions). Given the opposite dependence of the two reaction on the potential $U$, there has to be a boundary defined by the equilibrium between reaction (i) and (ii):

$$\Delta G_1 = \Delta G_2$$
$$-0.726\ \mathrm{V} + \alpha\ \mathrm{pH} + U_{eq} = -3.05\ \mathrm{V} + \alpha \log a_{\mathrm{Li}^+} - U_{eq}$$
$$U_{eq} = -1.16\ \mathrm{V} - \alpha/2\ \mathrm{pH} + \alpha/2 \log a_{\mathrm{Li}^+}$$

Corresponding to the equilibrium condition for the difference between reaction (i) and (ii):

$$\mathrm{LiH} \rightleftharpoons \mathrm{Li}^+ + \mathrm{H}^+ + 2e^-$$

which is in turn equivalent to reaction (ii) in section 5.1.2.

### 5.2.2 Implementation Details

The thermodynamic framework just described has been implemented into the Atomic Simulation Environment (ASE) Python package[31], and is currently available in the `pourbaix` module (`pourbaix` branch). The following is a brief introduction about the main functionalities of the module, and how to set up a Pourbaix diagram construction.

The initial required step for using the module consist in collecting a set of solid and aqueous species representing the target material and its decomposition products. Each species is represented by its chemical formula and formation energy, obtained by combining the total energy of the species with the ones of the compositional elements. Simple utilities can be written in order to automate the reference collection from available databases according to the chemical composition of the target material. Alternatively, it is possible to provide a custom set of species and formation energies, *e.g.* from experimental data. In the ASE implementation, the references (including the target material) are provided as a Python dictionary of the form `'formula': formation_energy`.

The reference dictionary - together with parameters such as the temperature, the ion concentration and the desired counter electrode - is then used to initialize a `Pourbaix` object, which takes care of the actual diagram construction with minimal user input.

The `Pourbaix` object first converts all the references into the `Species` class, which collects information about the material composition and automatically determines the number of protons, electrons and $H_2O$ "carried" by the species when entered in a chemical equation.

These species are then recursively combined with the target material in order to obtain all the possible decomposition pathways, described by balanced chemical equations. Each reaction is represented by a `RedOx` object, which pre-calculates $\Delta G^0$ and coefficients for the pH and $U$ term from eq. 5.19, including the contributions from the counter-electrode. Four counter-electrodes are currently implemented:

- The **standard hydrogen electrode** (keyword: `'SHE'`). The potential of the SHE is zero independently of pH and $U$, hence it has a null contribution to the reaction energetics. The SHE can perform the HER reversibly.
- The **reversible hydrogen electrode** (keyword: `'RHE'`) can as well perform the HER reversibly, however its potential depends on the pH. Its contribution to the reaction energetics is $\delta G = n_e \, \alpha \, \mathrm{pH}$, where $n_e$ is the positive(negative) number of electrons produced(consumed) at the working electrode.
- The **Ag/AgCl** electrode (keyword: `'AgCl'`) performs, reversibly, the reaction

  $$\mathrm{AgCl}(s) + e^- \longleftrightarrow \mathrm{Ag}(s) + \mathrm{Cl}^-$$

  Its contribution to the reaction energetics is independent of the pH and given by $\delta G = -n_e \, \delta G^0$, where $\delta G^0 = 0.222$ V is the standard electrode potential as recommended by IUPAC[40].
- The *platinum* electrode behaves similarly to the RHE, with the difference that it is not supplied by $H_2$. This means that during reduction processes at the working electrode it cannot perform the oxidation of $H_2$ into $H^+$. The only oxidation process available at the Pt electrode is the oxygen evolution reaction:

  $$\mathrm{H_2O} \longleftrightarrow 1/2 \, \mathrm{O_2} + 2 \, \mathrm{H}^+ + 2e^-$$

  Practically, during oxidation processes at the working electrode the Pt counter behaves identically to the RHE. All the reduction processes, on the other hand, are shifted up in energy by $1/2 \times 1.23 \text{ V} \times |n_e|$

An initialized `Pourbaix` object collects all the decomposition pathways of the target material, which we call "phases". The diagram can then be evaluated by calling the `Pourbaix.plot()` method in the desired window of pH and potential. During the plotting phase, $\Delta G_{pbx}$ is evaluated at each (pH, $U$) point according to the procedure described in the previous section. The resulting diagram reports at the same time the stability domains of the most stable phases and $\Delta G_{pbx}$, the latter as a color map.

## 5.3 Limitations of Pourbaix diagrams

Automatic Pourbaix diagram generation utilities such as the one just described constitute a double-edged sword when it comes to material stability predictions. On one hand, the simplicity of the method allows for generating large amounts of data in virtually no time. On the other hand, a poor understanding of the theoretical background and its inherent limitations can lead to misjudging the results. Citing the *Atlas*:

> "*In electrochemistry as in chemistry, the fact that a reaction is thermodynamically possible does not entail that this reaction actually takes place. Such a conformity between theoretical possibility and reality exists only for reactions which are practically reversible; the world of electrochemical reactions is full of irreversible changes which, like many chemical reactions, can take place only on the condition that there is an appreciable affinity, and their speed is influenced by the presence of a catalyst.*"

The main limitation of Pourbaix diagrams is that they do not carry information about the reaction mechanism and kinetics of the described electrochemical processes. For instance, when building the Pourbaix diagram of Ag, we will encounter the reaction

$$2\mathrm{Ag} + \mathrm{H_2O} \longrightarrow \mathrm{Ag_2O} + 2\mathrm{H}^+ + 2e^-$$

A comparison between the chemical potentials of reactants and products will determine the direction of the reaction according to the pH and potential conditions. The contributions to the free energy coming from Ag and $\mathrm{Ag_2O}$ depend entirely on the relative stability of their bulk phases in crystalline form, which exhibit radical structural differences.

Let us focus on a region of the diagram where the complete conversion of Ag into $\mathrm{Ag_2O}$ is determined to be spontaneous: although thermodynamically allowed, the reaction would reasonably over a myriad of microscopic and interconnected steps, involving the migration of oxygen from the surface into the deep bulk material and drastic rearrangements of the global bond network. Large thermodynamic and kinetic barriers associated with the reaction intermediates may arise, trapping the system into a metastable configuration. We can then say that traditional Pourbaix diagrams provide a time-averaged description of the degradation processes. The indefinite time scale corresponds to the time required to overcome all the kinetic barriers and obtain the thermodynamically most stable product.

The limitations of Pourbaix diagrams are particularly pronounced in the case of materials containing two or more elements other than O and H (which we call binaries, ternaries and so on...). As an example Fig. 5.2 displays the Pourbaix diagram of $\mathrm{MoS_2}$, which is predicted to be unstable over the whole spanned pH-potential region. This is an already alarming signal, since $\mathrm{MoS_2}$ stability in acqueous environment (at least in mild oxidizing/reducing conditions) has been confirmed in several experimental reports[41–43].

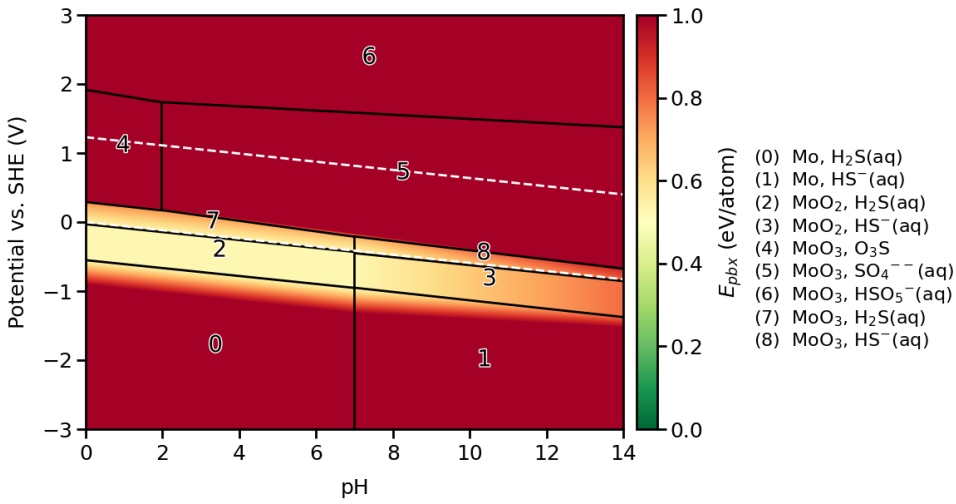


**Figure 5.2:** Conventional Pourbaix diagram of $MoS_2$ obtained with the procedure described in chapter 5. .

Let us investigate an arbitrary region of the diagram. For instance, the semi-reaction defining domain number (5) is the following:

$$MoS_2 + 11\,H_2O \longrightarrow MoO_3 + 2\,{SO_4}^{2-} + 22\,H^+ + 20\,e^- \tag{5.24}$$

Its expression describes the formation of not one, but two products radically different from $MoS_2$. Additionally, a very large number of electrons, $H^+$ and $H_2O$ is required in order to balance this semi-reaction. The corresponding Gibbs equation

$$\Delta G\,(pH, U) = \Delta G^0 - 11\,\alpha\,\mathrm{pH} - 20\,U \tag{5.25}$$

shows how $\Delta G$ decreases very rapidly with the pH, and even more rapidly with the potential. This applies in general to oxidation processes associated with large numbers of protons and electrons , which can rapidly take over the pristine material as the prevailing species. At the same time, a large number of electron transfer steps implies an equal amount of thermodynamic and kinetic barriers.

By examining the prevailing species in the different domains of the diagram, we will always find both a Mo-containing species and a S-containing species. This is required by the diagram generation procedure, where $MoS_2$ is always considered as the reactant. Accordingly, any balanced electrochemical reaction defined by the procedure has to satisfy its stoichiometry. The more elements in the material composition, the more

products have to be combined, leading to semi-reactions that can easily produce 50 or more protons/electrons for ternary or quaternary materials.

As a final note, the formation of solid products such as crystalline oxides can occur by nucleation and precipitation of the species dissolved in solution, which very often constitutes the preferred synthetic route for these materials[44]. These processes generally do not involve any change in the oxidation state. Consequently, they do not constitute electrochemical reactions and should not be considered in the diagram construction, besides the formation of the precursor solvated species.

In general, we recommend to interpret the acqueous stability predictions with a grain of salt. As said, the picture provided by Pourbaix diagrams can be seen as averaged over an indefinite amount of time, necessary to fully convert the electrode material into the thermodynamically most stable product. In the real scenario, competing reactions with lower thermodynamic driving force, but faster kinetics, may prevail and block the system in a metastable state. Comparison with the available experimental data is always encouraged.

In the following chapter we will show how we can switch to a microscopic description in order to provide, at the same time, mechanistic information and stability predictions, while abandoning the expectation of making exact predictions about the nature of the final products.

CHAPTER 6

# Extended surface Pourbaix diagrams

The dynamics of electrochemical processes, as elucidated in chapter 3, are intricately influenced by the characteristics of the electrical double layer that forms at the interface between the electrode surface and the adjacent solution phase. The surface side of the double layer serves as the gateway for electron transfer reactions, playing a crucial role in all electrochemical phenomena. These phenomena include not only desired reactions but also inadvertent side reactions that can lead to material deterioration. Given that solid materials are only able to engage in chemical interactions with the surroundings through their surface, the initial few atomic layers of a material surface encapsulate its entire array of chemical properties.

In recent years, the Pourbaix diagram framework has been adopted to characterize the state of different material surfaces in terms of coverage by water dissociation products[45–47]. Notably, the focus here shifts towards elucidating microscopic processes taking place at the atomic scale, made possible by the development of *ab initio* methods which were unavailable when the *Atlas* was formulated.

This microscopic description, however, is generally abandoned when describing irreversible oxidation and reduction processes compromising the structural stability of the electrode material, such as the material dissolution into ions. Alternatively, the bulk description is superimposed to the surface one, as done, e.g., in a work by Hansen *et al.*[48] in the attempt of describing both the surface coverage by O/OH and the formation of monoatomic ions from noble metals.

In this chapter, we show how the microscopic surface formulation can be improved in order to take into account of most fundamental material degradation processes. These include irreversible transformations that provoke the loss of electrode material and consequent changes in the stoichiometry, described by accounting for the formation of surface vacancies. We also improve the formulation of the chemical potential of the ions, by adjusting the concentration term in order to account for the surface excess caused by the strong electric field gradient at the double layer region.

The resulting diagrams are referred to as **extended surface Pourbaix diagrams** (ESPD), since their formulation covers both adsorption and dissolution processes. With the exception of the standard chemical potentials of the solvated species (which are

obtained from experimental data), the method relies entirely on an atomic-scale description of the surface electrochemical processes.

## 6.1 Background

From a chemical standpoint, a solid material behaves differently than a molecule. It interacts with the environment through a collection of independent reaction sites present on its surface, rather than as a unit. For example, the reaction paths leading to the formation of Mo- and S-containing species from $MoS_2$ are reasonably decoupled from each other at the atomic scale and can take place independently in two different regions of the surface. Hence, they are better described as two separate processes rather than one concerted mechanism. The original Pourbaix diagram formulation cannot deal with such independent processes, since it needs to consider the global stoichiometry of the material in order to obtain valid chemical equations.

Furthermore, the reason why any chemical process is determined to be spontaneous is that the free energy of the products is lower than the one of the reactants. According to the same principle, one can argue that if any of the elementary steps leading to the formation of the products is uphill in free energy, the process will be stopped to the last downhill reaction step.

In an extended surface Pourbaix diagram we model with DFT the pristine electrode surface and connect it, through chemical reactions, with a set of representative configurations describing the surface in an oxidized or reduced state. These configurations describe the most relevant intermediate states of the possible electrochemical degradation processes. The set of cases covered by the existing surface Pourbaix diagram formulation is expanded by including the material dissolution into solvated ions with consequent formation of vacancies. If any of these elementary steps is found to be energetically favourable in a given window of pH and applied potential, the pristine state of the electrode can be considered as compromised.

The resulting surface configuration constitutes a hint - rather than a precise prediction - of the final state of the material and the actual degradation mechanism. No experimental or theoretical technique can provide, alone, such type of information. We believe that a combination of multiple experimental and theoretical techniques is the key towards understanding the detailed dynamics of complex processes such as material degradation.

## 6.2 Surface degradation processes

For an electrode immersed in water in absence of interfering electrolytes in solution, we consider the following scenarios:

**O/OH/H adsorption.** This case is described by the following semi-reactions:

$$* + n\,\mathrm{H_2O} \longrightarrow n\,\mathrm{O}^* + 2n\,\mathrm{H}^+ + 2n\,e^-$$

$$* + n\,\mathrm{H_2O} \longrightarrow n\,\mathrm{OH}^* + n\,\mathrm{H}^+ + n\,e^-$$

$$* + n\,\mathrm{H}^+ + n\,e^- \longrightarrow n\,\mathrm{H}^*$$

where * represents the surface, while $n\,\mathrm{O}^*$, $n\,\mathrm{OH}^*$and $n\,\mathrm{H}^*$ represent a surface with $n$ units of O, OH and H adsorbed, respectively. The associated Gibbs equations are:

$$\Delta G = \mu[n\mathrm{O}^*] - \mu[*] - 2n\,\alpha\,\mathrm{pH} - n\,\mu^0_{\mathrm{H_2O}} - 2\,n\,U$$

$$\Delta G = \mu[n\mathrm{OH}^*] - \mu[*] - n\,\alpha\,\mathrm{pH} - n\,\mu^0_{\mathrm{H_2O}} - n\,U$$

$$\Delta G = \mu[n\mathrm{H}^*] - \mu[*] + n\,\alpha\,\mathrm{pH} + n\,U$$

where $\mu[n\mathrm{O}^*]$ is the chemical potential of a surface with $n$ O adsorbates (and similarly for OH adsorption). It is described as a formation energy, obtained by combining the DFT total energy of the surface with the energies of the elements in their standard state (which can be obtained from both experimental and computational references). $\mu[*]$ is the DFT total energy of the pristine surface, obtained in the same way. Since the surface configurations constitute solid phases, activity corrections are not necessary. O and OH adsorption are oxidation processes, while H adsorption is a reduction process.

Different numbers of adsorbates describe different surface coverages, hence by only considering this scenario we recover the typical surface Pourbaix diagram description. All these adsorption processes do not affect the chemical composition of the target material and can be chemically reversible, hence they can be labeled as “mild” oxidation (O, OH) and reduction (H) steps. By inspecting the length of the surface-adsorbate bonds in the optimized atomic structures, it can be inferred whether the adsorbate layer is permanent, *i.e.* it constitutes a passivation layer.

Note that all these cases represent key reaction intermediates in the oxygen evolution reaction (OER) and the hydrogen evolution reaction (HER). A close inspection of the diagram, its stability domains and the associated surface configurations can provide useful information about the suitability of the material as a HER or OER catalyst.

**Material dissolution.** The other considered scenario is represented by the release of electrode material towards the solution. Under oxidizing or reducing conditions, lattice atoms can be attacked by the acqueous species at the interface. These atoms are converted into ions, which move towards the solution phase and leave a vacancy behind.

The expression of the resulting chemical equation depends on the composition of the electrode and the specific ion under consideration. For a given material, we model a set of surface configurations containing a single vacancy at any of the inequivalent atomic positions. For each of these configurations, the diagram construction procedure first determines the nature of the missing atomic species, then it defines an electrochemical semi-reaction for each of the available ions containing that species.

Two examples are the dissolution process of $MoS_2$ into ${MoO_4}^{2-}$ and $HS^-$, with formation of a Mo and a S vacancy , respectively:

$$* + 4\,H_2O \longrightarrow V^*_{Mo} + {MoO_4}^{2-} + 8\,H^+ + 6\,e^-$$

$$* + H^+ + e^- \longrightarrow V^*_S + HS^-$$

where $V^*_S$ and $V^*_{Mo}$ represent the surface with a sulphur and molybdenum vacancy, respectively. The general Gibbs equations describing dissolution processes as such is

$$\Delta G = \mu[V^*_X] - \mu[*] - \mu[I_X] - n_h\,\alpha\,\mathrm{pH} - n_w\,\mu^0_{H_2O} - n_e\,U \tag{6.1}$$

where $\mu[V^*_X]$ is the formation energy a surface containing a vacancy of element $X$, and $\mu[I_X] = \mu^0[I_X] + k_B T \log a$ is the chemical potential of a solvated species containing the same element, corrected for the activity. $n_h$, $n_w$ and $n_e$ are automatically determined in order to obtain a balanced chemical reaction.

We choose to not consider the cases where a surface atom has been substituted by O or OH. These configurations can be obtained by forming a vacancy and subsequently adsorbing O/OH in the corresponding site. Hence, they describe a two-step process requiring vacancy formation as the necessary initial step.

## 6.3 Accounting for the surface excess of ionic species

The chemical potential of an ion in the solution phase is given by:

$$\mu = \mu^0 + k_B T \ln a \tag{6.2}$$

where $a$ is the activity of the ion. The activity can be seen as a dimensionless “effective concentration” that accounts for ion-ion interactions in non-ideal solutions.

In every availble Pourbaix diagram formulation, the ion activity is set to a small value (typically $10^{-6}$), equivalent to an arbitrary threshold determining the presence of the ion in a small, although appreciable, amount. Out of equilibrium, the material dissolution causes further production of ions, which eventually exceed this threshold activity. In these conditions, the material is labeled as subject to dissolution an thus unstable (according to the same arbitrary criterion).

The exchange of species in the double layer region involves the first few atomic layers of the electrode and the molecules or ions found in their close proximity on the solution side. In particular, the concentration (thus the activity) of a given ionic species in

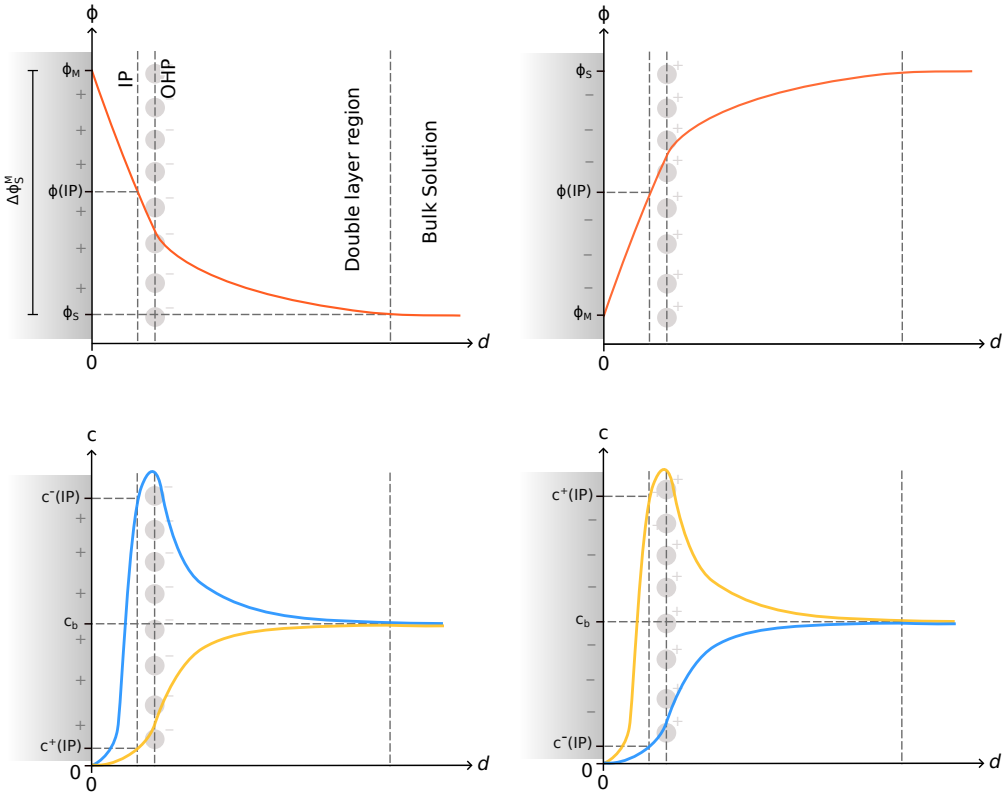


**Figure 6.1:** Top panels: qualitative behaviour of the electric potential $\phi$ as a function of the distance $d$ from the surface of a positively charged (left) and negatively charged(right) electrode. $\phi(IP) = (\phi_M + \phi_S)/2$ is the potential at the interaction plane (IP). Bottom panels: qualitative behaviour of the concentration of positive (yellow) and negative (blue) ions in the double layer region. $c^+(IP)$ denotes the concentration of a positive ion at the IP, while $c^-(IP)$ is the equivalent for a negative ion. $c_b$ is the bulk concentration..

this region may be larger or smaller than the one in the bulk solution depending on the relative charge state of the electrode and the ion itself. The difference between the surface and bulk concentration is called **surface excess**, which can be positive or negative depending on the electrical state and composition of the double layer.

By using the Boltzmann distribution law, the concentration of an ion $i$ at a given point $r$ in space, $c_i(r)$ can be related to the one in the bulk phase $c_i^b$ through the expression

$$c_i(r) = c_i^b e^{-W/k_B T} \tag{6.3}$$

where $W$ is the work necessary for moving the ion from the bulk solution to point $r$. In

absence of short-range ion-ion interactions, this work is purely electrostatic, and given by

$$W = z_i e(\phi^S(r) - \phi_b^S) \tag{6.4}$$

where $z_i$ is the charge of the ion, $\phi^S(r)$ is the electrostatic potential in the solution at point $r$ and $\phi_b^S$ is the electrostatic potential in the bulk solution.

If not directly adsorbed on the surface, the ions that sit the closest to the surface are found at an imaginary plane parallel to the electrode surface, called the *outer Helmholtz plane* (OHP). As illustrated in Fig. 6.1, a large part of the overall metal-solution potential difference $\Delta_S^M\phi$ builds up in the thin solution layer delimited by the electrode surface and the OHP. The distance of the OHP from the electrode surface cannot be determined accurately. In order to obtain a qualitatively correct description, We will assume that the ions able to engage in chemical interactions with the electrode sit at the **interaction plane (IP)**, which pinpoints half of the overall metal-solution potential difference:

$$\phi(IP) - \phi_b^S = 1/2\,\Delta_S^M\phi \tag{6.5}$$

By combining this expression with equation 6.3 and 6.4, the ion concentration of ion $i$ at the IP is given by

$$c_i(IP) = c_i^b \exp(-\frac{z_i e\Delta_S^M\phi}{2k_BT}) \tag{6.6}$$

According to Trasatti[49], the absolute potential of an electrode $M$ can be expressed as

$$\phi_M^{abs} = \Phi_M + \Delta_S^M\phi \tag{6.7}$$

where $\Phi_M$ is the work function of the electrode material(in volt). The experimental value for the standard hydrogen electrode is $\phi_{SHE}^{abs} = 4.44$ V, which can be used in order to obtain the absolute potential of any other electrode through:

$$\phi_M^{abs} = U + \phi_{SHE}^{abs} \tag{6.8}$$

where $U$ is the applied cell potential referred to the SHE. By combining eq. 6.7 and 6.8 the metal-solution potential different can finally be expressed in terms of known quantities:

$$\Delta_S^M\phi = U + \phi_{SHE}^{abs} - \Phi_M \tag{6.9}$$

and eq. 6.6 becomes

$$c_i(IP) = c_i^b \exp\left[-\frac{z_i e}{2k_BT}\left(U + \phi_{SHE}^{abs} - \Phi_M\right)\right] \tag{6.10}$$

By approximating the ion activity to its concentration, eq. 6.10 can be introduced in the expression of the chemical potential (eq. 6.2):

$$\boxed{\mu_i = \mu_i^0 + k_B T \ln c_i^b - \frac{z_i}{2}\left(U + \phi_{SHE}^{abs} - \Phi_M\right)} \tag{6.11}$$

As expected, since the electrode potential affects the surface ions concentration, which in turn affects the reaction energetics, the chemical potential now includes a potential-dependent term.

Note that, if an ionic species is not present in solution prior to the material dissolution producing the ion itself, its bulk concentration $c_i^b$ is entirely determined to the number of vacancies generated by the process. A realistic value can be obtained by combining quantities relative to the simulated structure with parameters relative to the geometry of the real electrochemical cell:

$$c_i^b \simeq \frac{A_{el}}{A_{sc} N_{av} V_{sol}} \tag{6.12}$$

Where $A_{el}$ is the geometrical area of the electrode, $A_{sc}$ is the area of the simulation cell hosting a single vacancy, $N_{av}$ is the Avogadro constant and $V_{sol}$ is the volume of the solution. For example, a 1 $cm^2$ Pt electrode with a vacancy every four unit cells immersed in 1L of solution produces a bulk ion concentration of approximately $2.6 \cdot 10^{-10}$ mol $L^{-1}$.

As an example, we consider a Pt surface. The work function of Pt is 5.65 eV. At an applied potential of 1V, the concentration of ions with $z_i = -2$ and $z_i = +2$ at the surface of this electrode (as calculated from eq. 6.10) is 5.8 $\cdot 10^{-14}$ mol $L^{-1}$ and 1.15 $\cdot 10^{-6}$ mol $L^{-1}$, respectively. This translates into a difference of about 0.4 eV between their concentration contributions to the reaction free energy. We can see how the surface excess can depend dramatically on the relative charge state of ion and surface. Assuming one arbitrary concentration for all ionic species may result in significant underestimation or overestimation of their chemical potential and, thus of the overall reaction energetics.

Figure 6.1 shows the qualitative profile of the electrostatic potential and concentration in the double layer region for electrode surfaces in different charge states.

## 6.4 Diagram evaluation

Evaluating a complete surface Pourbaix diagram starts by generating the pristine surface, plus all the relevant adsorption and vacancy configurations. These are generally obtained in a supercell, whose size depends on

- The desired spacial separation between vacancies. Our recommendation is to choose a supercell large enough to prevent lateral interactions between neighboring vacancies.
- The number of surface coverage states considered for the adsorption configurations.
- The computational cost of the calculations.

The structures are first optimized. In our case, the calculations are performed at the PBE level, including van der Waals D3 corrections[50] in order to correctly describe the dispersive interactions in adsorption configurations. A ground state calculation is then performed for each configuration in order to obtain The total energy, necessary for determining the chemical potential, and the work function, necessary for determining the ionic surface excess.

In some cases, the optimized structure exhibits significant rearrangements in the bond network of the adsorbates. For instance, two adsorbed OH units can recombined into two adsorbed O atom and a desorbed $H_2$ molecule, or an adsorbed O atom and a desorbed $H_2O$ molecule. These cases no longer represent the surface configuration that was modeled in the first place, for which no local minimum was found, and are thus discarded.

The accuracy of the results can be improved in several ways for quantitative or semi-quantitative predictions, at the expense of the computational cost. For instance, a cheap exchange-correlation functional can be replaced by a more accurate one. Solvent effects can be accounted for by including one or more layers of explicit solvent. It is also possible to include mixed surface coverages of *e.g.* both O and OH.

According to the material composition, a list of acqueous species with experimental formation energies is extracted from a database. The pristine surface, its adsorption and vacancy configurations and the acqueous species are then combined with each other in order to obtain valid electrochemical semi-reactions. The chemical potentials of the ions are corrected for the surface excess according to the scheme described in the previous section.

This set of semi-reactions, automatically completed with the parallel process at the counter-electrode, is able to describe the first step of most elementary electrochemical processes leading to the degradation of the target material.

From this point, the procedure is equivalent to the one used for constructing traditional Pourbaix diagrams (see section 5.1): the Gibbs free energy of all these reactions is

evaluated as a function of the pH and applied potential against the reference electrode of choice, then the stability domains of the predominant species are drawn.

# CHAPTER 7

# Results

## 7.1 Inter-layer hybridization effects in Van der Waals heterostructures

The exfoliation of monolayer graphene in 2004[2] opened a new paradigm of materials science by introducing the class of two-dimensional (2D) materials, characterized by their atomically thin extension in the out-of-plane direction. Since then, the discovery of monolayer $MoS_2$[51], the first 2D semiconducting material showing extraordinary strong excitonic effects[52, 53] and the discovery that any set of 2D monolayers can be stacked into so-called van der Waals heterostructures[54–56] (vdWHs) opened up new pathways and potentials for the world of 2D materials.

Thanks to the dispersive nature of the inter-layer interactions, a virtually infinite number of heterostructures can be obtained by playing with the composition and number of monolayers. On top of that, the latter can be freely and independently rotated ("twisted") in plane relative to each other. Depending on the **twist angle**, a specific periodic superlattice called **moiré pattern** is originated in the composite structure, shaping the inter-layer interaction landscape and thus the orbital hybridization.

In recent years special attention have been paid to experimentally investigate and map out intra- and interlayer exciton energies[57–60] and their twist-angle dependence in few-layer semiconducting vdWHs[60–62]. Despite the vdWHs being characterized by weak interlayer van der Waals bonds and only little interlayer orbital hybridization, the above experiments prove that it becomes increasingly important to accurately incorporate such effects into *ab-initio* calculations.

Herein, we first describe the lattice matching procedure necessary in the first place to obtain computable atomic structures of vdWHs. We then describe our computational framework, based on a self-consistent scissors operator (SO) able to reproduce with great accuracy the quasi-particle band gap of the heterostructure at the DFT level. Using this framework, we investigate interlayer hybridization effects on the band gap of a $MoSe_2-WS_2$ heterostructure as a function of the twist angle between the $MoSe_2$ and $WS_2$ layers.

### 7.1.1 Lattice matching of twisted vdW heterobilayers

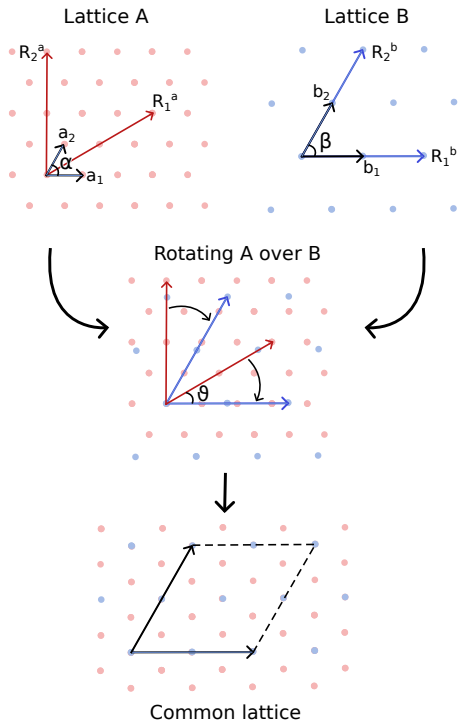


**Figure 7.1:** Illustration of the lattice matching procedure. .

Twisted vdWHs are particularly challenging systems to describe from first principles. Virtually any relative rotation of the individual monolayers is possible, although some specific twist angles may result in more favourable configurations and thus be preferred. The resulting moire pattern may manifest at the microscopic scale, with a periodicity of several thousands of atoms. Such lattices are impossible to treat with most *ab-initio* methods, which are restricted by the periodic boundary conditions and thus the huge computational cost of large unit cells.

The first step towards making vdWHs accessible to DFT consists in finding a set of twist angles that provides unit cells of limited size (few hundreds of atoms at most). This becomes particularly important for systems that are not "lattice matched", *i.e.* the lattice constants of the individual layers are significantly different from each other and a vdWHs cannot be obtained by trivially stacking their unit cells on top of each other, without introducing significant strain in the overall structure. In order to do so, we implemented in ASR a lattice matching routine based on the coincidence lattice method[63].

Let us consider a pair of two-dimensional monolayers A and B with in-plane primitive

basis vectors ($\mathbf{a}_1$, $\mathbf{a}_2$) and ($\mathbf{b}_1$, $\mathbf{b}_2$), respectively. Any linear combination of these basis vectors of the form

$$\mathbf{R}^a = m_1\mathbf{a}_1 + m_2\mathbf{a}_2$$
$$\mathbf{R}^b = n_1\mathbf{b}_1 + n_2\mathbf{b}_2$$

where $m_1$, $m_2$, $n_1$, $n_2$ are integers, constitutes a new basis vector which connects the origin **O** to a specific point of each lattice. Any pair of distinct basis vectors $\mathbf{R}_1^a$, $\mathbf{R}_2^a$ defines a valid 2D unit cell for lattice A, and similarly for lattice B.

In order to find a common unit cell, one needs to identify two sets of basis vectors - one for lattice A, one for lattice B - of similar lengths and spanning a similar angle, within a tolerance:

$$||\mathbf{R}_1^a| - |\mathbf{R}_1^b|| < \varepsilon$$
$$||\mathbf{R}_2^a| - |\mathbf{R}_2^b|| < \varepsilon$$
$$|\alpha - \beta| < \chi$$

Where $\alpha$ is the angle between $\mathbf{R}_1^a$ and $\mathbf{R}_2^a$, $\beta$ the angle between $\mathbf{R}_1^b$ and $\mathbf{R}_2^b$, $\varepsilon$ the length tolerance and $\chi$ the angle tolerance. A perfect match can be expected only for homobilayers (*e.g.* twisted bilayer graphene), where A and B are two identical copies of the same lattice. Once the above conditions are met, a common unit cell able to host the heterostructure can be finally obtained by

1. Rotating A over B by the twist angle $\theta$ between $\mathbf{R}_1^a$ and $\mathbf{R}_1^b$, or *vice versa*.
2. Finding a common point between between $\mathbf{R}_1^a$ and $\mathbf{R}_1^b$ and one between $\mathbf{R}_2^a$ and $\mathbf{R}_2^b$ by applying compressive strain to one lattice and tensile strain to the other, or a combination of both.

This method, implemented during the course of this project in the Atomic Simulation Recipes (ASR) software package[64], is able to determine at once a number of matching unit cells with different twist angles. The number and size of the unit cells depends on the maximum allowed size of the coefficients $m_1$, $m_2$, $n_1$ and $n_2$ and the maximum allowed strain. Fig. 7.1 provides a graphical representation of the lattice matching procedure.

### 7.1.2 Computational framework

As illustrated schematically in Fig. 7.2, most DFT functionals tend to overestimate hybridization and charge transfer between the layers in a van der Waals heterostructures. These delocalization errors are tied to the systematic underestimation of the band gap

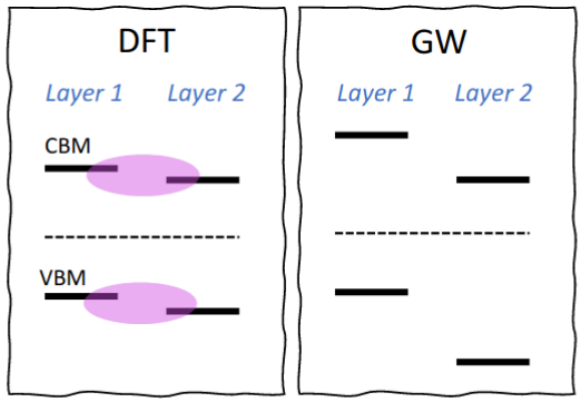


**Figure 7.2:** Illustration of the delocalization errors in vdWHs related to the incorrect band alignment produced by DFT. .

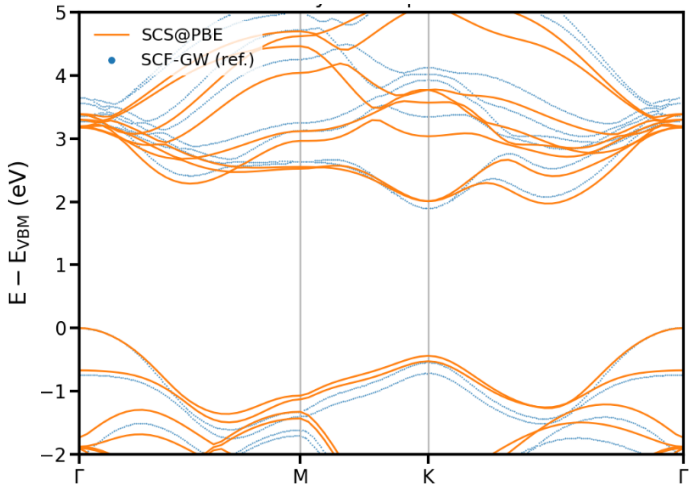


**Figure 7.3:** In orange: electronic band structure of a $MoS_2$ homobilayer obtained with the SCS operator on top of the PBE functional. In blue: self-consistent GW band structure of the same homobilayer, reproduced from ref. [65] .

and, accordingly, of the absolute and relative positions of the band edges, resulting in an incorrect relative band alignment between the layers. We address this issue by adopting the GPAW implementation of the **self-consistent scissors operator** (SCS), which shifts the valence and conduction states of the individual monolayers to match the G0W0Γ quasi-particle band edges. Then, a full self-consistent DFT calculation is performed for the whole heterostructure. By operating on a LCAO basis naturally localized on the individual atoms, the SCS is able to distinguish states of the individual

layers. Conceptually, the SCS of a vdWHS composed by two layers A and B can be expressed as $\hat{S} = \hat{S}_A + \hat{S}_B$, with

$$\hat{S}_A = \sum_{c_A} s_A^c |c_A\rangle\langle c_A| + \sum_{v_A} s_A^v |v_A\rangle\langle v_A|$$
$$\hat{S}_B = \sum_{c_B} s_B^c |c_B\rangle\langle c_B| + \sum_{v_B} s_B^v |v_B\rangle\langle v_B| \tag{7.1}$$

where $|c_A\rangle$ and $|v_A\rangle$ represent the conduction and valence states of layer A, and similarly for layer B. $s_A^c$, $s_A^v$, $s_B^c$ and $s_B^v$ are the conduction and valence band **SCS shifts** of layer A and B. They are obtained as the simple difference between the PBE and G0W0Γ band edges relative to the vacuum level. Both are extracted at no cost from the C2DB database[37]. By using the SCS, we obtain a very good approximation of the quasiparticle electronic structure of a $MoS_2$ bilayer at the cost of a PBE calculation, as illustrated in Fig. 7.3. This encouraging result suggests that the framework is able to correctly describe the interlayer hybridization as well in larger vdVHs, unaccessible by expensive G0W0Γ calculations.

### 7.1.3 Benchmarks against experiments

In order to benchmark the method, we obtain a set of 11 $MoSe_2$-$WS_2$ vdWHs at twist angles between 8° and 52°, according to the previously described procedure. These structures consist of at most 246 atoms and can be computed at the PBE level. Twist angles closer to 0° and 60° determine significantly larger structures, unaccessible by our computational framework.

The method is benchmarked against the experimental results by Alexeev *et al.*, who find a twist angle-dependent variation in the interlayer exciton peaks of the vdVHs due to a change in the interlayer orbital hybridization[60, 62]. At a future stage of the project, we will be able to obtain the interlayer exciton binding energies in order to obtain a closer comparison with the experiments. Nevertheless, we expect the electronic band gap to be affected by the same hybridization effects and thus provide a good qualitative agreement.

First, we need to verify that in absence of interlayer interactions the band gap value is independent of the twist angle. We artificially suppress the interlayer hybridization by keeping the $MoSe_2$ and $WS_2$ layer separated by a fixed 10 Å distance. The preliminary results, shown in Fig. 7.4a (blue data points), yield a poor qualitative behaviour of the band gap. The reason is that the small strain (generally below 1%) applied to the different vdWHs during the lattice matching procedure is sufficient to shift the monolayer band edges by a significant amount, compared to the magnitude of the variations observed experimentally (few meV in the flat region, ca. 50 meV at twist angles close to 0° and 60°). For instance, the valence band maximum of $MoSe_2$ shifts downwards in energy by ca. 60 meV upon 1% strain along the $x$ direction.

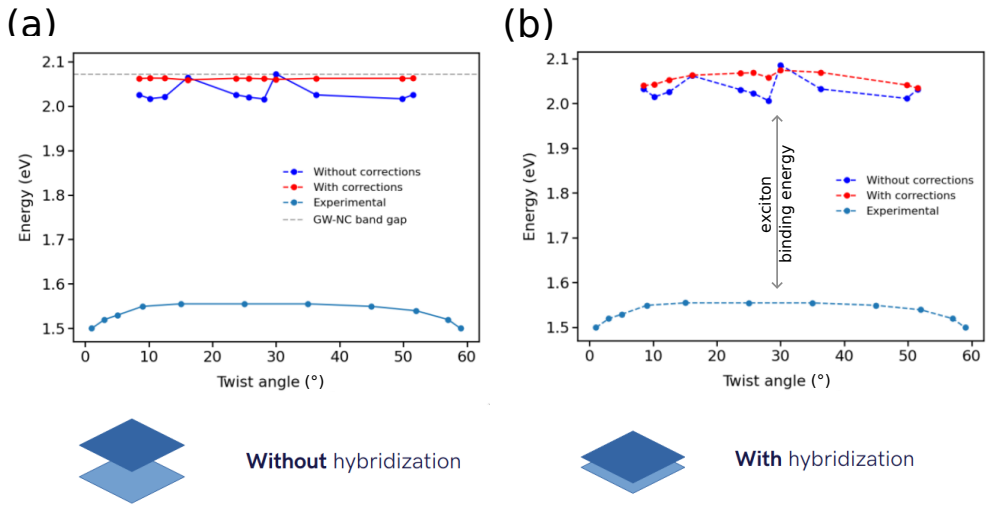


**Figure 7.4:** (a) Band gap of a $MoSe_2$-$WS_2$ heterobilayer as a function of the twist angle. The monolayers in the heterostructure are kept at a fixed distance of 10 Å in order to suppress the interlayer hybridization. The dashed grey line pinpoints the band gap obtained by simply combining the GW band edges of the individual monolayers. The blue (red) data points represent the DFT band gap before (after) applying the strain corrections to the SO. The experimental exciton energies (lower blue line) are reproduced from ref. [62]. (b) Band gap of a $MoSe_2$-$WS_2$ heterobilayer as a function of the twist angle. In this case the heterostructures are in their relaxed configurations, hence inter-layer hybridization effects are included. .

It is then necessary to include a correction into the SCS shifts based on the **deformation potentials** of the monolayers, the latter expressed as:

$$D_i^k = \frac{\partial E_i}{\partial \varepsilon_k} \tag{7.2}$$

Where $E_i$ is a generic eigenvalue and $\varepsilon_K$ the applied strain along a generic component $k$ ($xx$, $yy$, $xy$, ...). For instance, the strain correction to the valence band SCS shift of layer A is obtained as:

$$\delta_A^v = [D_{VBM,A}^{xx}, D_{VBM,A}^{xy}, D_{VBM,A}^{yy}] \cdot [\varepsilon_{xx}^A, \varepsilon_{xy}^A, \varepsilon_{yy}^A]^T \tag{7.3}$$

The strain corrections to the SCS shifts are applied in the direction that compensates for the applied strain:

$$s_A^v{}' = s_A^v - \delta_A^v \tag{7.4}$$

The red data points in Fig. 7.4a show the band gaps of the vdVHs after applying the strain corrections, now distributed along a straight line without hybridization effects. Expectedly, this line lies very close to the value obtained by simply combining the G0W0Γ band edges of the isolated monolayers (dashed grey line). Hybridization effects are then "switched on" by considering the vdWHs in their optimized configuration (structural relaxations are performed with D3 corrections). The band gaps, shown in Fig. 7.4b now present a downward bend at angles close to 0° and 60°, qualitatively reproducing the experimental behaviour.

The results presented herein will be included in Publication (II) , currently in preparation.

## 7.2 Tunable electronic and catalytic properties of self-intercalated 2D bilayers

Self-intercalation, *i.e.* intercalation of native metal atoms in the van der Waals gap of 2D materials, has recently emerged as an effective technique to produce new types of covalently bonded, crystalline phases with stoichiometry dependent properties, which we refer to as ic-2D.

So far, the ic-2D family is limited to few members that have been realized experimentally and/or modeled from first principles[66–71]. The existing literature has demonstrated that, indeed, these materials can present emerging new properties compared to the host structure. In particular, self-intercalation has been shown to alter the conduction behaviour (*n*-type to *p-type*)[67], induce ferromagnetism[68, 69, 71], improve the catalytic activity[72], modulate interlayer exchange interactions and enhance the magnetic anisotropy[73–75].

During the course of this project, we performed a systematic exploration of novel ic-2D materials using density functional theory calculations in a high-throughput approach. Out of the initial 1348 configurations we identified 95 ic-2D with high thermodynamic stability, calculated their electronic properties and assessed their suitability as HER catalysts. We found that self-intercalation generally enhances the metallic behaviour compared to the host material, and can promote tunable catalytic properties and magnetism. With this work we aim to expand the family of ic-2D materials, opening new pathways for further exploration by theory and experiments towards applications in electronics and catalysis.

This section presents a brief summary of the main results discussed in greater detail in Publication (I) , printed in copy in Chapter 8.

### 7.2.1 Intercalation workflow

We first select from C2DB 77 non-magnetic, binary host systems characterized by high thermodynamic and dynamic stability and small unit cells (6 atoms at most). All of these hosts are known experimentally in few-layer or bulk form and do not contain toxic or rare elements.

Using a series of utilities implemented in ASE[31], we automatically generate 1348 ic-2D of different composition and concentration of intercalated atoms (ic-concentration). The ic-concentration is defined as the number of intercalated atoms per primitive unit cell of the bilayer host, and can be expressed as a fraction or percentage. These atomic structures are passed to a thermodynamic stability workflow which performs a structural optimization and a ground state calculation. The ground state energies are then used for determining the position of the ic-2D phases on the convex hull, obtained by including the bulk phases that belong to the same compositional space. If any ic-2D structure lies within 200 meV from the convex hull, it is passed to two separate workflows, executed in parallel:

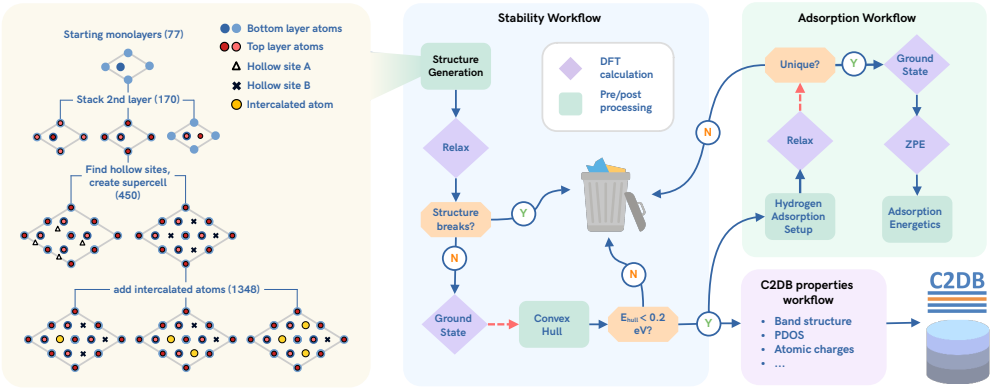


**Figure 7.5:** Workflow for calculation of the ic-2D properties, including a schematic representation of the structure generation procedure. The numbers in parentheses represent the number of structures generated at each step. Red dashed arrow represent bottlenecks in the workflow, where all the previous steps have to be completed for the related ic-2D structures before proceeding to the following steps. .

- The *properties workflow* evaluates basic properties of the ic-2D materials including electronic band structure, projected density of states, Fermi surface, Bader charges, magnetic moments and stiffness tensor. This workflow is a part of the full property workflow used to characterize 2D materials in the C2DB.
- The *adsorption workflow* generates hydrogen adsorption configurations at the inequivalent surface sites, calculates their ground state and determines the hydrogen adsorption free energies.

The complete workflow, together with the structure generation procedure, is illustrated in Fig. 7.5.

### 7.2.2 Electronic and magnetic properties

The first outstanding observation resulting from our screening process is that, when the host bilayer exhibits a finite band gap, this is either fully eliminated or significantly reduced in its ic-2D phases already at low ic-concentrations. Self-intercalation always preserves the metallic nature when already present in the pristine bilayer, and generally results in an increase in the density of states at the Fermi level. These observations are highlighted by Fig. 7.6, which compares the electronic band gap of the 95 ic-2D structures (blue lines) with the one of the pristine bilayers (red lines). The enhanced metallicity is caused by the introduction inside the band gap of metallic states partially localized on the intercalated atoms, as shown in Fig. 7.7 for 33%-intercalated $MoS_2$.

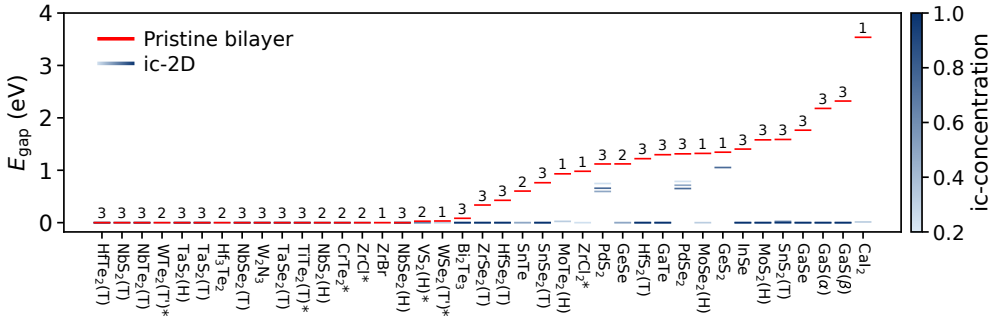


**Figure 7.6:** Band gap ($E_g$) of the pristine bilayer host systems (in red) and their ic-2D counterparts (in shades of blue). The x-axis displays the monolayer unit formulas and, in parenthesis, the crystalline phase (when available). Sytems with the same stoichiometry are labelled with greek letters when a reported crystalline phase is missing. An asterisk is appended to the label for systems with at least one magnetic ic-2D configuration. The ic-2D are reported in shades of blue according to the ic-concentration, following the color map on the side. Only ic-2D with $\Delta H_{hull} \leq 0.2$ eV/atom are considered. For each starting bilayer, the number of ic-2D configurations that satisfy this condition is reported above the pristine bilayer line. .

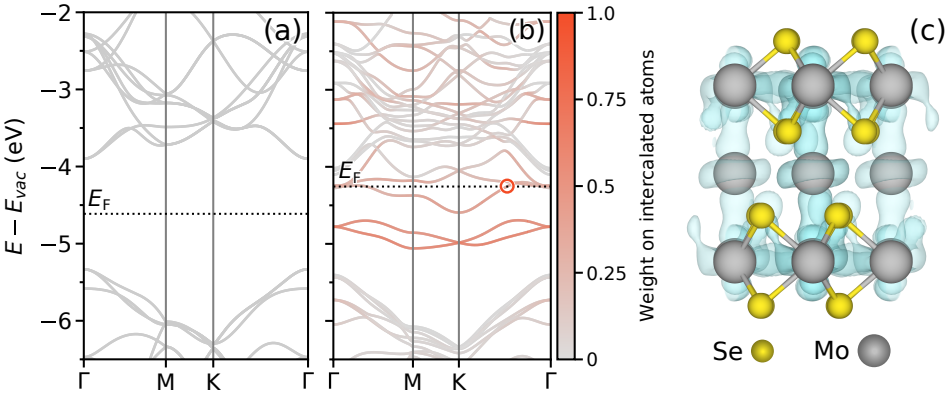


**Figure 7.7:** a) Band structure of a pristine $MoSe_2$ monolayer in a $(\sqrt{3} \times \sqrt{3})$R30 supercell. Energies are relative to the vacuum level, the Fermi energy is represented by a dashed line. b) Band structure of 33% self-intercalated $MoSe_2$, in the same supercell as for panel a). The color scale shows the projections of the eigenstates on the intercalated atoms. c) Real space distribution of the states highlighted by the red circle in panel b). .

Additionally, we observe that self-intercalation induces magnetism as an emergent property for the five different, initially non-magnetic, ic-2D materials (see table S1-2): 100%-ic TiTe2, 33% and 50%-ic W2Se4, 33%-ic ZrCl and 25%-ic ZrCl2. The corresponding host systems are marked with an asterisk in Fig. 7.6.

### 7.2.3 Catalytic properties

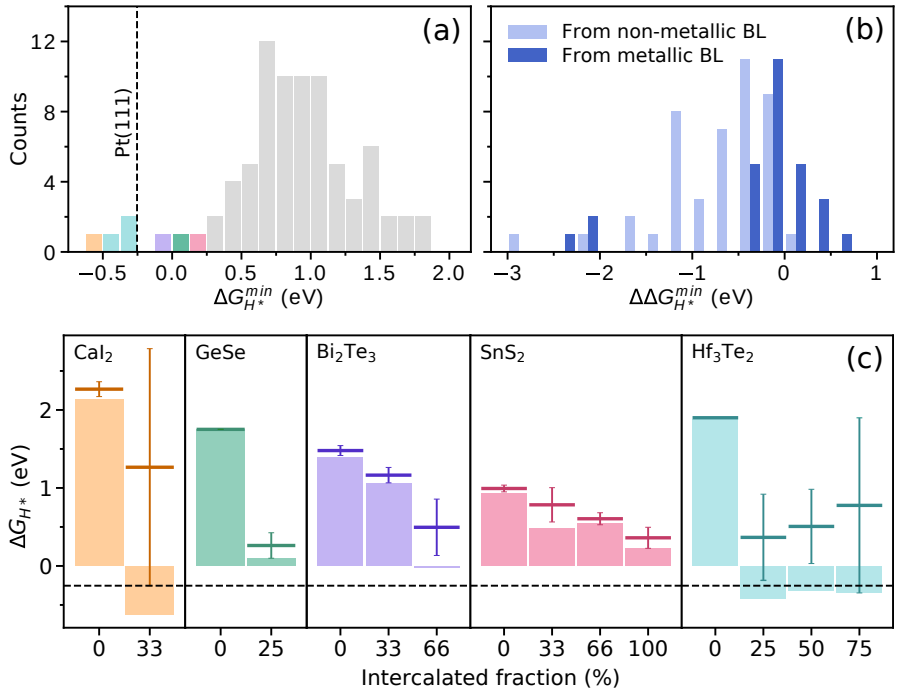


**Figure 7.8:** a) Distribution of the hydrogen adsorption energies on the lowest-energy site ($\Delta G^{min}_{H*}$) for the thermodynamically stable ic-2D. The colored bars correspond to the four ic-2D with $\Delta G^{min}_{H*}$ within 0.3 eV from the one calculated for a Pt(111) surface (-0.25 eV, dashed line). b) Distribution of the $\Delta G^{min}_{H*}$ of the ic-2D relative to the ones calculated for the pristine bilayers. light blue and dark blue bars gather the ic-2D obtained from non-metallic and metallic bilayers, respectively. c) Hydrogen adsorption energies $\Delta G_{H*}$ as a function of the ic-concentration. We selected the four systems having at least one ic-2D configuration that satisfies the criterion described for panel a). The filled bars represent $\Delta G^{min}_{H*}$, while the darker, horizontal lines correspond to the H adsorption energy averaged between all the adsorption sites. The error bars show the corresponding standard deviation. The horizontal dashed line shows, again, $\Delta G^{min}_{H*}$ of Pt(111). Colors are consistent with panel a). .

As previously anticipated, we computed the hydrogen adsorption free energies $\Delta G_{\mathrm{H}^*}$ at different surface sites for each of the 95 selected ic-2D structures, as a measure of their activity as HER catalyst according to the computational hydrogen electrode model illustrated in section 4.2.

We expect the site with the lowest $\Delta G_{H^*}$ to dominate the overall reaction dynamics, and we denote the corresponding H adsorption energy as $\Delta G_{H^*}^{min}$. Fig. 7.8a shows the distribution of the calculated $\Delta G_{H^*}^{min}$. Despite the distribution being centered around 1.0 eV, seven ic-2D structures show adsorption energies within 0.5 eV from the near-thermoneutral value calculated for a Pt(111) surface (-250 meV), here used as a model for the ideal HER catalyst. These seven systems are $CaI_2$ (33%-ic), GeSe (25%-ic), $Bi_2Te_3$ (66%-ic), $SnS_2$ (100%-ic) and $Hf_3Te_2$ (25, 50 and 75%-ic).

Fig. 7.8b shows the change in $\Delta G_{H^*}^{min}$ between the ic-2D structures and their parent pristine bilayers. In general, the chemical reactivity tends to increase in ic-2D structures obtained from non-metallic host systems (red bars). This observation correlates well with the observed enhanced metallicity, which is expected to increase the chemical reactivity. With the notable exception of ic-$Hf_3Te_2$, self-intercalation seems to leave the reactivity either unaffected or slightly decreased in intrinsically metallic host materials (blue bars).

Fig. 7.8c shows the hydrogen adsorption energies as a function of the intercalated fraction for $CaI_2$, GeSe, $Bi_2Te_3$, $SnS_2$ and $Hf_3Te_2$. The colored bars represent $\Delta G_{H*}^{min}$ while the horizontal (vertical) lines represent the average (standard deviation) of the distribution of $\Delta G_{H*}$ over all adsorption sites. The variation in $\Delta G_{H*}$ among the different adsorption sites highlights how the presence of the intercalated atoms affects the local environment, resulting in a number of diverse and generally more reactive adsorption sites rather than the few, chemically equivalent sites present on the pristine host systems.

## 7.3 ASE implementation of Pourbaix diagrams

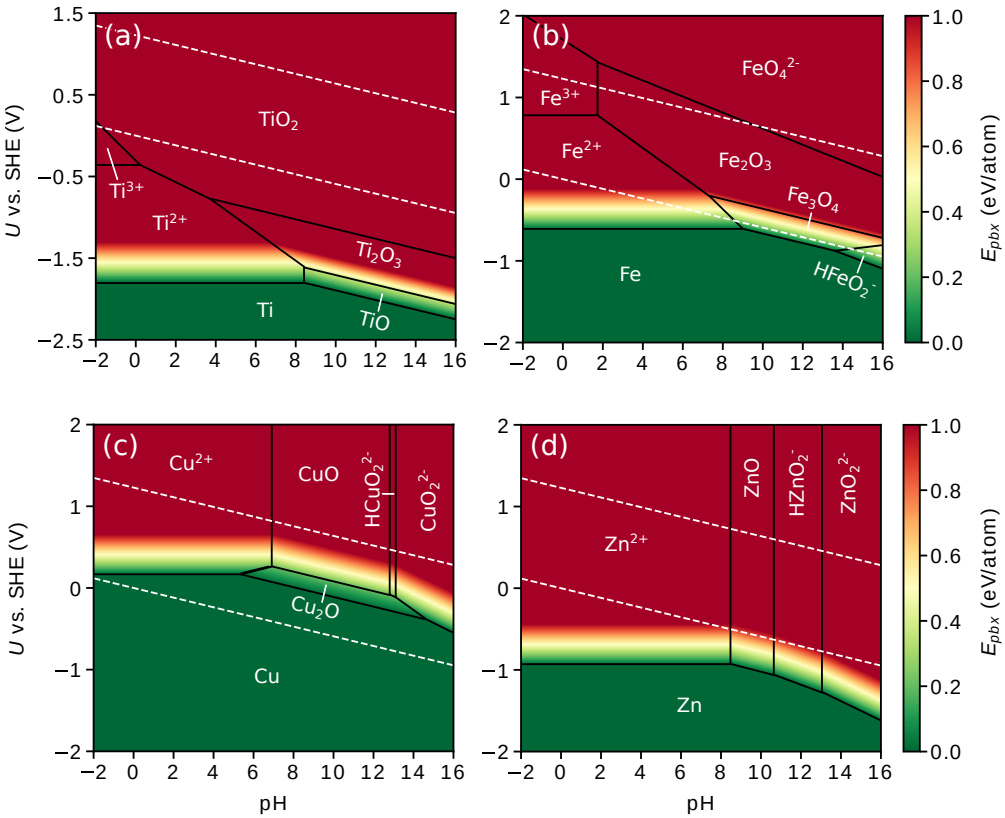


**Figure 7.9:** Pourbaix diagrams of (a) Ti, (b) Fe, (c) Cu, (d) Zn obtained with the same formation energies as used by Pourbaix in the *atlas*[30]. The concentration of all ionic species has been set to $10^{-6}$ M. The dashed white lines represent the HER and OER equilibrium potentials. Potentials are referred to the SHE.

As discussed in section 5.1, we implemented in the atomic simulation environment (ASE)[31] a Pourbaix diagram construction method based on the original formulation. In order to assess whether the utility functions correctly, we benchmarked the calculated diagrams against Pourbaix's result for a representative set of metals. Fig. 7.9 shows the diagrams calculated for Ti (panel a), Fe (panel b), Cu (panel c) and Zn (panel d) by including the same solid and acqueous phases originally used by Pourbaix, as well as the same formation energies. All four diagrams, obtained by setting the concentration of the ionic species to $10^{-6}$ M, show a perfect agreement with the corresponding diagrams in the *atlas*[30] when comparing the equilibrium lines corresponding to the same ionic concentration.

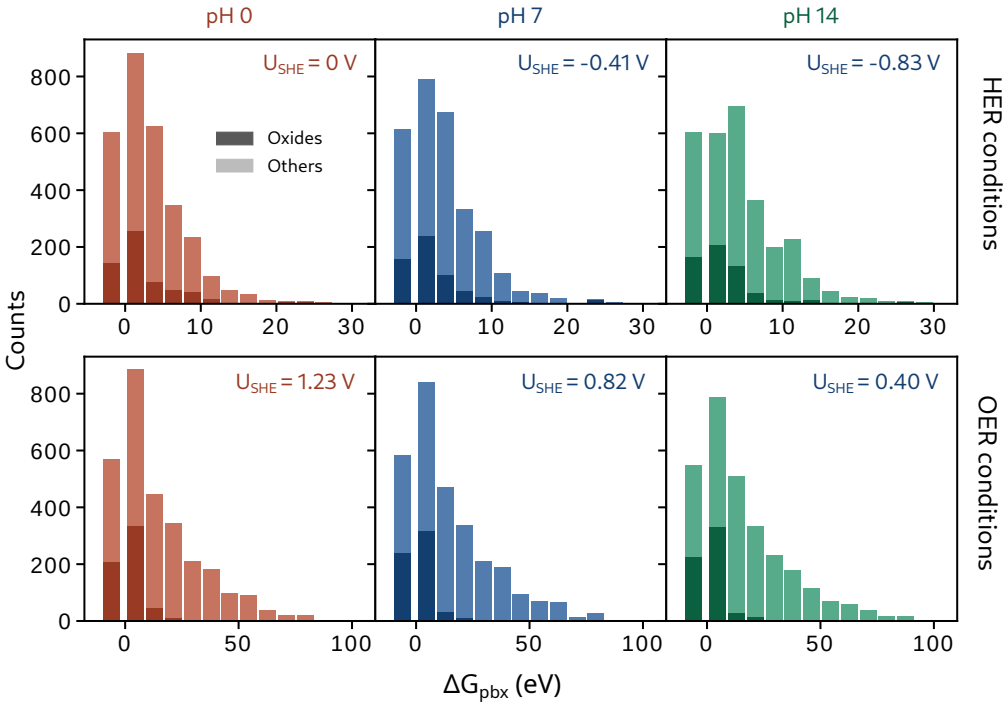


**Figure 7.10:** Distribution of the Pourbaix energy $\Delta G_{pbx}$ calculated for 2902 2D materials with $E_{hull}$<50 meV/atom in different conditions of pH and applied potentials vs. SHE relevant for the HER and OER processes. The dataset is split between oxides (darker color) and non-oxides (brighter color). In each subplot, the column to the far left gathers all the materials with $\Delta G_{pbx}$=0.

Once the utility is implemented in the computational workflow of the Computational 2D Materials Database (C2DB)[37], Pourbaix diagrams will enrich the list of properties already available for each material in the database. As a preliminary assessment of the acqueous stability of 2D materials, we ran the diagram generation utility on the entire set of thermodynamically stable entries[1] in the C2DB database which, as of 30/11/2022, consists of 2902 materials. The solid references necessary for the diagram construction are automatically fetched from the OQMD database[35], while the acqueous references are obtained from a database implemented in ASE.

Fig. 7.10 displays the distribution of the Pourbaix energy $\Delta G_{pbx}$ obtained at six different points of the diagram, representative of the conditions required to perform the HER and the OER in acidic, neutral or alkaline environment with the SHE as the counter electrode.

[1]According to the criterion $E_{hull}$<50 meV, where $E_{hull}$ is the energy above the convex hull.

| Conditions | $U$ (V) | pH | % stable materials | % stable oxides |
|---|---|---|---|---|
| Acidic HER | 0 | 0 | 20.2 | 23.5 (22.8) |
| Neutral HER | -0.41 | 7 | 20.1 | 25.1 (24.2) |
| Alkaline HER | -0.83 | 14 | 20.0 | 26.5 (25.5) |
| Acidic OER | 1.23 | 0 | 17.2 | 30.8 (25.5) |
| Neutral OER | 0.82 | 7 | 17.5 | 34.6 (29.1) |
| Alkaline OER | 0.40 | 14 | 16.5 | 34.9 (27.8) |

**Table 7.1:** Stable 2D materials in different conditions of pH and applied potential vs. SHE. The column "% stable materials" shows the global percentage of materials with $\Delta G_{pbx}$=0 over the total of 2902 selected materials, in each condition. Among the materials with $\Delta G_{pbx}$=0, the column "% stable oxides" shows, in percentage, how many are oxides. The numbers in parentheses show the percentage of stable oxides relative to the total number of oxides (604) in the same conditions.

Very large $\Delta G_{pbx}$ values are found at the tail of each distribution due to the occasional presence of reaction pathways with extreme number of electrons and protons. For instance, one of the decomposition pathways determined for $Pt_3Se_3Ta_3S_{14}$ is:

$$Pt_3Ta_3S_{14} + 139/2\,H_2O \longrightarrow 3\,PtO_2 + 3/2\,Ta_2O_5 + 14\,{SO_4}^{2-} + 139\,H^+ + 111\,e^-$$

Which, in alkaline OER conditions yields a $\Delta G_{pbx}$ of 131 eV. This, as explained in section 5.3, stems from the inherent limitations of the traditional Pourbaix diagram formulation.

Since oxides are known to generally show good stability in electrochemical environment, we split the dataset into non-oxides and oxides, the latter constituting 21% of the entire material pool. The stable materials ($\Delta G_{pbx}$=0) are represented by the column on the far left of each subplot. It is immediately evident that $\Delta G_{pbx}$ is distributed over a significantly wider energy interval in OER conditions due to the larger electrostatic contribution ($U$ term in eq. 5.19) to the reaction free energy of the decomposition pathways. Although most materials are predicted to decompose under all the explored conditions, between 17% and 20% of them shows good thermodynamic stability, as reported in table 7.1.

In HER conditions, about 20% of the materials are predicted to be stable at acidic, neutral as well as alkaline pH. Among them, 23% are oxides at pH 0. This percentage increases to 27% at alkaline pH. In OER conditions, the fraction of stable materials decreases to about 17%, about one third of which are oxides. Overall, while the fraction of stable oxides tends to increase when moving from HER to OER conditions, the stability of the rest of the materials points towards a general decrease.

The generally higher stability of oxides in HER/OER conditions compared to other materials is due to the fact that the oxides, on average, have a lower amount of decomposition products in higher oxidation state as they are "already oxidized". Since oxidation processes are favoured at positive applied potentials and - generally - alkaline pH, these materials naturally have a lower amount of available reaction pathways that benefit from such conditions. Conversely, they are more susceptible to reduction processes, which are favoured at negative potentials and - also generally - acidic pH. These "ideal" conditions are never met at the evaluation points in Fig. 7.10, since the lowest potential values coincide with the most alkaline pH conditions. With the SHE as the counter-electrode, "Ideal" reduction conditions are rarely met at the explored potential and pH values: moving the pH towards alkaline values is accompanied by a negative shift in the equilibrium potential of the global reaction, causing the pH and $U$ contributions to the Gibbs free energy to compensate each other.

The results presented herein will be included in Publication (III) , currently in preparation.

## 7.4 Extended surface Pourbaix diagrams

In this section we present a series of benchmarks for the extended surface Pourbaix diagram (ESPD) method described in chapter 6 against experimental and theoretical data on a selected set of materials. We show how the diagrams can not only provide a good qualitative comparison with experimental observations, but can also support them by providing additional mechanistic information about the electrochemical process at hand. The following results will be included as well in Publication (III) , currently under preparation.

### 7.4.1 $MoS_2$

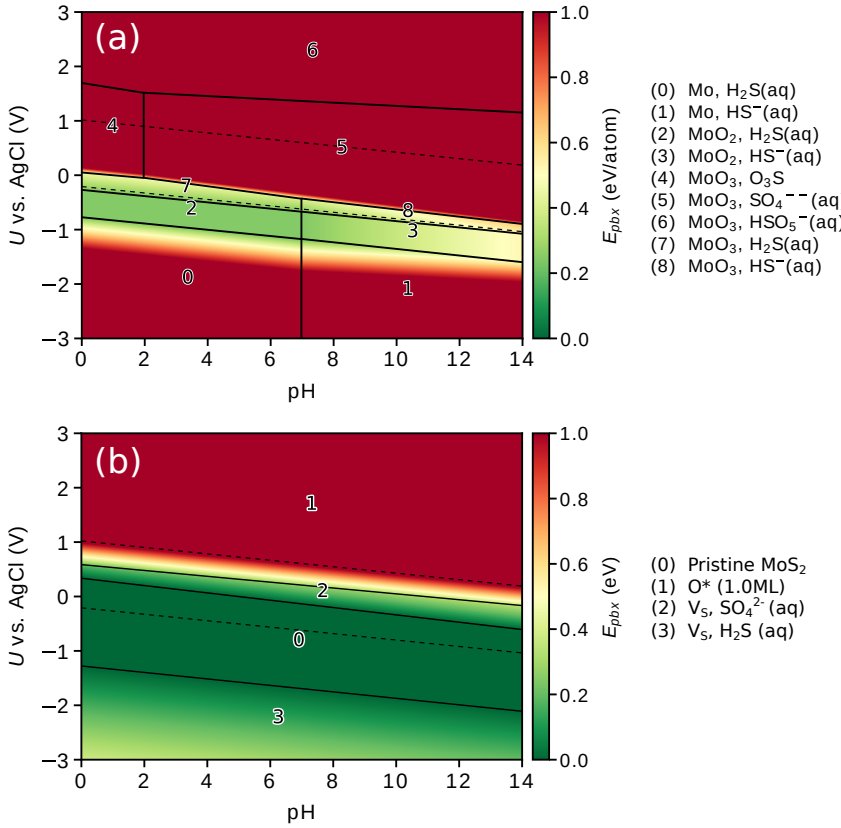


**Figure 7.11:** a) Conventional Pourbaix diagram of $MoS_2$, with Ag/AgCl as the counter-electrode. The upper and lower dashed lines represent the $H^+/H_2$ and $O_2/H_2O$ equilibrium potential, respectively. b) ESPD of $MoS_2$ with Ag/AgCl as the counter-electrode.

Molybdenum disulphide $MoS_2$ is among the most extensively studied materials among the class of transition metal dichalcogenides (TMDs) due to its unique properties and potential applications in various fields, including electronics, optoelectronics, catalysis, and more[76]. One of the reasons for its success in several fields of application is its structural stability in a wide range of experimental conditions. In particular, $MoS_2$ suitability towards HER catalysis and water treatment applications implies the stability of the material in acqueous environment in a wide range of pH conditions and, at least, at the moderate potentials required for the HER.

Existing studies on $MoS_2$ for supercapacitor applications[77, 78] provide useful cyclic voltammetry (CV) profiles at pH 0 and applied potentials ranging between +0.5 V and -1.1 V against the saturated calomel electrode (SCE). No oxidation or reduction peaks are found, confirming the material stability in the explored potential range. The standard potential of the SCE is +0.27 V against SHE and +0.05 V against Ag/AgCl. Hence, comparison with our calculated ESPD against Ag/AgCl should provide at least a good qualitative agreement with the experimental observations.

As shown in Fig. 7.11a, the traditional Pourbaix diagram predicts $MoS_2$ to be thermodynamically unstable across all pH conditions and potentials in the +0.5 to -1.1 V range, in contradiction with the experimental observations. By including more relevant intermediate states in the ESPD description, we aim to overcome the limitations discussed in section 5.3 and find the expected stability window for $MoS_2$ in acqueous environment.

Fig. 7.11b shows the ESPD calculated against the Ag/AgCl electrode. A large stability domain is found, spanning both positive and negative potentials around the HER equilibrium potential. The newfound stability of $MoS_2$ is due to the large vacancy formation energies and O/OH adsorption energies. The ESPD shows excellent qualitative agreement with the aforementioned CV scans, defining a stability window at pH 0 between +0.3 and -1.25 V against Ag/AgCl. Above 0.3 V, $MoS_2$ dissolution into $SO_4^{2-}$ is predicted to be favourable, diverging from the experimental observations which assess the material stability at least up to 0.5 V.

In both the cited references the CV scan is performed in presence of 1M $Na_2SO_4$ electrolyte, whose dissociation produces $SO_4^{2-}$ ions at the same concentration in the bulk solution. The ESPD in Fig. 7.11b uses the $SO_4^{2-}$ bulk concentration value obtained from eq. 6.12, which amounts to $2.1 \cdot 10^{-10}$ mol $L^{-1}$ assuming the absence of $SO_4^{2-}$ in solution prior to the dissolution process.

Fig. 7.12a shows the ESPD of $MoS_2$ (in the 0.3-0.7 V potential range and 0-1 pH range) obtained by setting the bulk concentration of $SO_4^{2-}$ to the experimental value of 1.0 mol $L^{-1}$ . This, according to eq. 6.11, causes a 0.56 eV increase in the chemical potential of $SO_4^{2-}$ and, consequently, in the free energy of the related dissolution processes. As expected, the latter are shifted towards higher pH and potential values and do not constitute anymore a competitive degradation pathway at pH 0. Fig. 7.12b displays a slice of the diagram at pH 0, highlighting the effect of the applied correction to the $SO_4^{2-}$ bulk concentration on $MoS_2$ stability.

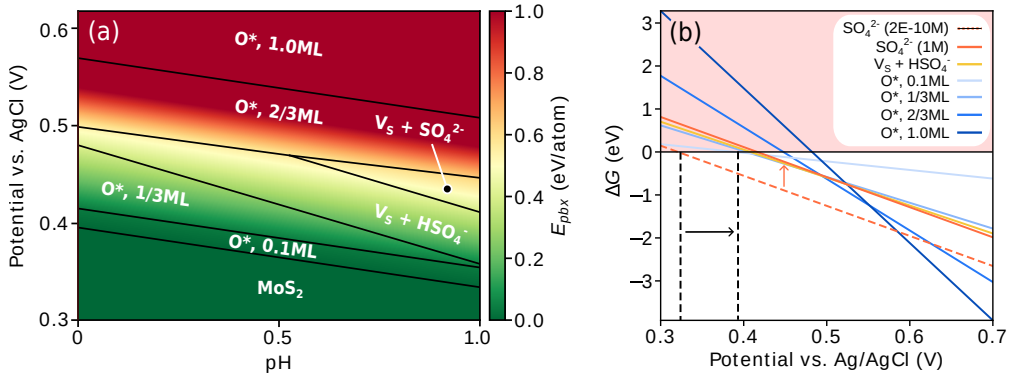


**Figure 7.12:** a) ESPD of $MoS_2$ obtained by setting the bulk concentration of $SO_4^{2-}$ to 1M. Potentials are reported against the Ag/AgCl electrode. b) Slice of the diagram in panel (a) at pH 0. The colored lines represent the Gibbs free energy of the available reaction pathways as a function of the potential. Above 0 eV, the processes are thermodynamically unstable. The dashed orange line shows the free energy profile of $MoS_2$ dissolution into $SO_4^{2-}$ by using the default bulk concentration (ca $2{\cdot}10^{-10}$M), determined by the surface vacancy concentration. The continuous orange line describes the same process in presence of 1M $SO_4^{2-}$ in the solution. The dashed black lines represent the upper bound of the stability domain of $MoS_2$ before and after correcting the $SO_4^{2-}$ bulk concentration value.

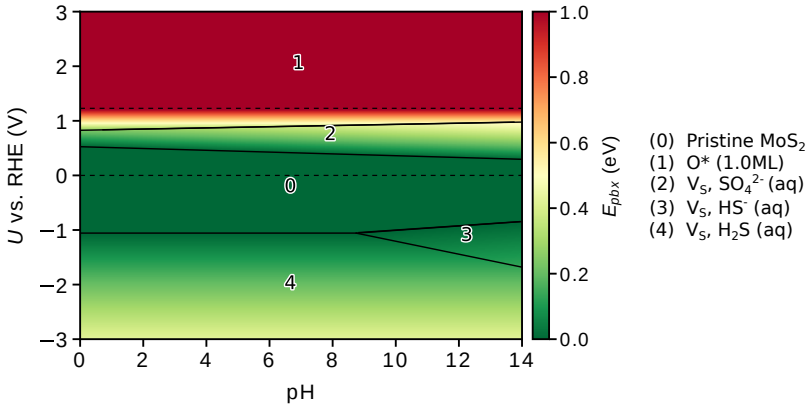


**Figure 7.13:** ESPD of $MoS_2$ with RHE as the counter-electrode.

Compared to the diagram in Fig. 7.11b, the upper limit of the stability domain of $MoS_2$ at pH 0 is expanded, now extended from 0.3 V up to ca. 0.4 V. At this potential, oxygen adsorption becomes the thermodynamically most favourable process. If the latter is reversible, $MoS_2$ stability is further increased to 0.48 V, until the material is predicted to dissolve into $HSO_4^-$. Note that, at pH 0, this ionic species is stable only in a very narrow potential window of ca. 30 mV. At the same potentials its formation

competing with oxygen adsorption at 0.1ML coverage, which has negative $\Delta G$ as well and, reasonably, a lower kinetic barrier. All things considered, this dissolution process is not expected to constitute a serious threat to the material stability.

Finally, a study by Tsai *et al.* investigates the effect of sulphur vacancies at the basal plane of $MoS_2$ on the HER catalytic activity[79]. In their work, the experimental onset of the desulphurization process is observed around -1.0 V against RHE and confirmed by theoretical predictions. These results are in good agreement with the ESPD reported in figure 7.13 where $MoS_2$ is predicted to dissolve into $H_2S$ at the same applied potential.

## 7.4.2 Phosphorene

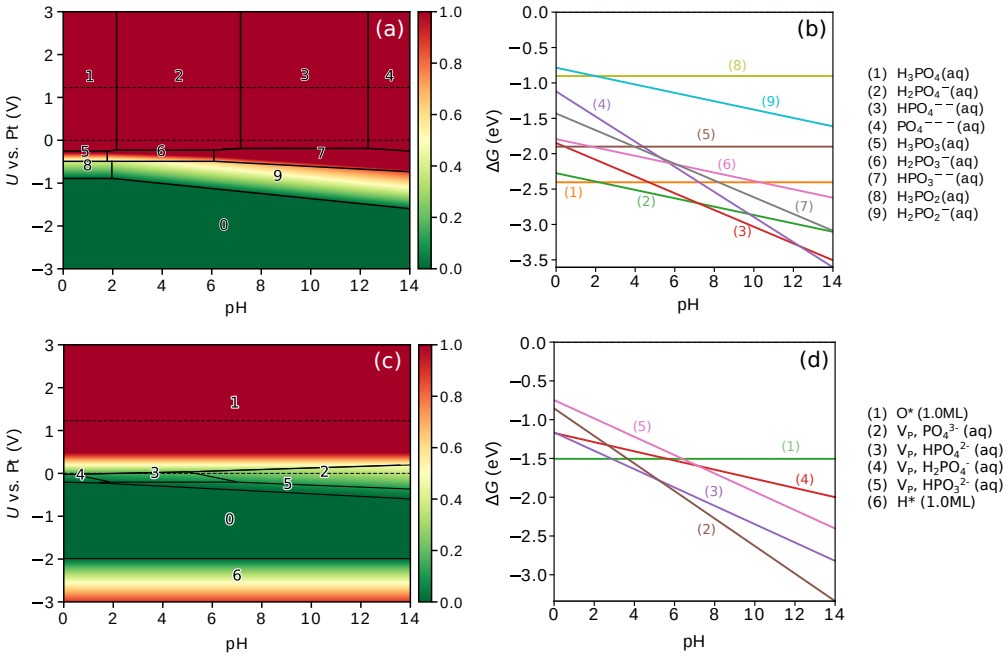


**Figure 7.14:** a) Pourbaix diagram of phosphorene, with Pt as the counter-electrode. b) Horizontal slice of diagram (a) at $U = 0$. c) ESPD of phosphorene, with Pt as the counter-electrode. d) Horizontal slice of diagram (c) at $U = 0$. The colorbars report the Pourbaix energy, in eV.

Phosphorene is the 2D counterpart of black phosphorus, which has a layered structure in bulk phase and can be mechanically exfoliated. Due to its high hole mobility and tunable band gap, phosphorene has been identified as a promising candidate for applications in field-effect transistors and photodetectors[80–82].

One of the main limitations towards the use of phosphorene in real devices is its instability in presence of oxygen and moisture, making its encapsulation with inert materials a necessary step. As observed by Wood *et al.*, phosphorene samples in ambient conditions degrade in few days. When the process is monitored, an XPS peak attributed to oxidized phosphor species ($PO_x$) appears with concurrent formation of bubbles on the sample surface.[83]. These observations are clear signs of a spontaneous electrochemical process producing the oxidation of the surface P atoms and the concurrent evolution of a gaseous species – most likely $H_2$.

In spontaneous electrochemical processes such as corrosion, the material acts as both the cathode and the anode: the oxidized and reduced species interact directly at the surface, without the necessity of driving the electrons through an external circuit. The oxidized species is the electrode material, while the reduced species are the protons converted into $H_2$ in a nearby region of the electrode. Since the potential at the surface is constant, the electrostatic contribution to the reaction energetics is zero.

In the potential-pH space, spontaneous processes are best described by the horizontal line crossing $U = 0$, where $U$ is the applied potential against the platinum electrode. Similarly to a generic material in contact with water, a Pt electrode is sensitive to the pH and cannot reverse the hydrogen evolution reaction, since it is not in contact with a $H_2$ reservoir. In this picture, it represents the portion of the electrode that evolves $H_2$.

As shown in Fig. 7.14a and 7.14c, both the conventional Pourbaix diagram and the ESPD predict phosphorene to be unstable in ambient conditions, represented by the lower dashed black line. This is due to three factors:

1. P has a variety of oxidation states and, accordingly, solvated oxoanions ($H_xP_yO_n^{z-}$) which have particularly low formation energies.
2. Phosphorene has low P vacancy formation energy. Some of the available dissolution pathways have negative $\Delta G$ already in standard conditions.
3. Oxygen adsorption on phosphorene is exothermic in ambient conditions.

Note that points 2 and 3 do not affect the Pourbaix diagram in Fig. 7.14a, where the predicted instability is mainly due to the relative chemical potentials of phosphorene and its dissolution products, since vacancies and adsorbates are not accounted for. Since vacancy formation is energetically affordable, although still endothermic in most cases (depending on the dissolution product), the ESPD predicts higher stability for phosphorene at negative potentials, up to ca. -0.2 V at pH 0.

Fig. 7.14b shows a slice of the ESPD at $U = 0$. All of the oxidation processes have negative free energy over the whole pH range, meaning that they are all thermodynamically favourable and can take place simultaneously. Phosphorene is thus sensitive to a variety of degradation pathways already in ambient conditions. After a prolonged exposure to the atmospheric moisture, the material is expected to release a variety

of phosphor oxoanions while adsorbing oxygen, leaving a partially dissolved, partially passivated surface. The XPS peaks observed in the aforementioned study can be attributed to the oxoanions, which can remain adsorbed on the surface, as well as the P atoms in contact with the adsorbed oxygen. All of these oxidation semi-reactions are necessarily paralleled by hydrogen evolution, which is the most logical origin of the bubbles observed experimentally.

At $U < -2$ vs. Pt, hydrogen adsorption (and parallel oxygen evolution) becomes favourable. The P-H bond lengths of 1.4 Å in the optimized structure are close to the one in phosphine $PH_3$, the most stable P-H molecular compound. It is thus possible that hydrogen adsorption in phosphorene is chemically irreversible and permanently affects the surface structure.

### 7.4.3 $Ti_2C$ MXene

MXenes are a class of two-dimensional materials that belong to the family of transition metal carbides, nitrides, and carbonitrides, with the "M" representing a transition metal and "X" representing carbon and/or nitrogen. They are characterized by their exceptional electronic, mechanical, and thermal properties, making them highly versatile for a range of applications including batteries[84], gas sensing[85] and photocatalysis[86].

One of the most prominent materials in the MXenes class is Titanium carbide $Ti_xC_y$. The Ti:C ratio in the material stoichiometry depends on the number of atomic layers in the so-called MAX phase, where "A" is a metallic element such as Al. The latter is selectively etched, converting the MAX phase into the final MX phase. The rich surface chemistry of this material has posed challenges towards its use in acqueous environment, due to its tendency to be passivated and/or decomposed by water and its derivates.

Decomposition processes are accelerated by heat and the presence of defects. In particular, Xia *et al.* identified Ti vacancies as the main promoter of the material degradation[87]. The extent and kinetics of these oxidative processes are likely influenced by the amount of defects and exposed edges present in the as-synthesized material. As observed by Zhang *et al.*, colloidal suspensions of $Ti_3C_2$ can decompose to $TiO_2$ and amorphous carbon over several days in solution[88]. $Ti_xC_y$ electrodes have been recently tested as HER catalysts, showing only modest performance which tends to further decrease over several cycles[89]. The poor activity and robustness seem to confirm the tendency of this material to form passivation layers and/or to dissolve.

The general instability of $Ti_xC_y$ in acqueous environment, the role played by surface vacancies and the unpredictable nature of MXenes surface termination make this system a perfect case study for the ESPD framework. We choose as our model surface the thinnest possible form of titanium carbide, with stoichiometry $Ti_2C$. Its structure consists in a layer of carbon sandwiched between two layers of titanium. In order to cover a wider range of surface terminations, we include mixed coverages of both O and OH (at different ratios) in our set of configurations.

The resulting ESPD, shown in Fig. 7.15a, highlights the remarkable surface reactivity of $Ti_2C$, which favours the coverage by a full monolayer of adsorbates in the whole spanned $U$-pH region. As expected, the overall oxidation state of the adsorbate layer progressively increases when moving from negative to positive applied potentials, going from a ML of adsorbed hydrogen up to a ML of oxygen. Mixed O and OH adsorption is found stable at intermediate potentials. Our results agree well with the surface Pourbaix diagram obtained by Gao *et al.*[90], with the difference that in our ESPD we include hydrogen adsorption, which affects the shape of the diagram at negative potentials.

No surface state involving the formation of vacancies is found as the most stable phase. Nevertheless, several of the dissolution processes have negative $\Delta G$ in extended regions of the diagram, as seen in the ESPD in Fig. 7.15b, obtained by omitting all the adsorption configurations. In order to investigate the spontaneity of dissolution reactions in ambient conditions, we report in Fig. 7.15c a slice of the ESPD against the Pt electrode at $U = 0$ (again, we omit the adsorption processes). At least one of the reactions producing Ti vacancies is exothermic in any pH conditions, supporting the observations by Xia *et al.* regarding the role of Ti vacancies in $Ti_2C$ degradation. H, O and OH adsorption still constitute the most favourable processes in these conditions. Hence, we expect a mixed contribution from adsorption and dissolution processes to the overall material degradation.

### 7.4.4 Gold oxidation

Our final example shows how improving the description of the metal-solution interface at the atomic scale can push the method towards semi-quantitative preditions.

Fig. 7.16a shows the CV scan of a Au(111) surface, performed in presence of 0.05M $H_2SO_4$ electrolite, which yields a pH of 1.3. During the anodic scan against Ag/AgCl, four main oxidation peaks are found:

- at $U = 0.3$ V, a small oxidation peak is associated with the lifting of the herringbone reconstruction, which is the preferred surface configuration for Au(111)[91]. The TEM images acquired at larger potentials (not shown) confirm the disappearance of the herringbone distinctive pattern.
- at $U = 0.9$ V, a second small peak has been attributed to a disordered-to-ordered rearrangements of the adsorbates on the surface. XPS spectra confirm the presence of sulphur on the surface, likely stemming from the dissociation products of the $H_2SO_4$ electrolyte. This species survive the transfer in vacuum required for XPS acquisition, suggesting a strong affinity with the Au surface.
- at $U = 1.2 - 1.3$ V a strong oxidation peak is observed. Its origin is unknown, since the XPS spectra do not identify a change in the oxidation state of Au or any feature associated with oxygen. A possible cause is the reversible adsorption of oxygen-containing species such as O, OH or OOH. If weakly adsorbed, these species might escape the surface upon the sample transfer in vacuum. This hypothesis has not been confirmed by experiments, since the available investigation techniques generally provoke the loss of the solvation layer.
- at $U > 1.7$ V (not shown in Fig. 7.16a) a large peak arises, accompanied by oxygen evolution. The process causes the irreversible oxidation of Au, which manifests as a darkening of the electrode surface and determines a notable shift of the Au and O XPS peaks (see Fig. 7.16b,c). The structure of the resulting oxide layer is uncertain and might be amorphous, since it does not generate clear diffraction patterns.

These experimental results were used as a benchmark for assessing the accuracy of the ESPD method. The goal is to identify the set of parameters necessary for closing the gap between the electrode-solution interface as modeled by DFT and the real interface in working conditions. If achieved, the ESPD turns into to a semi-quantitative investigation tool, able to reproduce the positions of the oxidation peaks and link them to a specific set of surface configurations. This can provide great support to the interpretation of the experimental data, which lacks insight at the atomic scale.

The pristine Au(111) surface is our reference system, obtained from the bulk Au structure and modeled as a 2×2×5 slab. The atomic coordinates of the bottom three layers are kept fixed in their bulk configuration during structural optimizations. We choose

not to model the computationally expensive herringbone reconstruction, since its lifting at $U = 0.3$ V is confirmed without ambiguity. The following observations are thus reliable at applied potentials larger than 0.3 V, since at lower values we cannot determine whether the reconstruction plays a significant role in the electrochemical processes.

The initial, minimal set of configurations consists of the pristine surface, O and OH adsorbates, and the surface with a Au vacancy. As for the adsorption structures, only 1/4ML coverage is considered at this stage. H adsorption is neglected since it is activated at negative potentials, which are not covered by the CV scan that we aim to compare with.

Fig. 7.17a shows the slice obtained at pH=1.3. The pristine surface is found to be stable until 0.75 V, after which O adsorption becomes spontaneous. Around 1.6 V vacancy formation becomes the preferred degradation process. The position (in terms of potential) and origin of this phase boundary seem to agree with the last CV peak: vacancy formation is likely a required step for a strong and irreversible oxidation processes causing structural changes in the electrode surface. It is clear, however, that this set of surface configurations is not sufficient to reproduce the remaining peaks observed in the experimental CV.

As previously stated, the peak at 0.9 V has been attributed to an electrochemical process involving the adsorbates. In a second iteration of the ESPD, we expand our set of adsorption configurations by accounting for the coverage of O and OH adsorbates up to a full ML. Additionally, we include two structures describing the adsorption of $SO_4{}^{2-}$ and $HSO_4{}^{-}$. The bulk concentration of these ions is determined in the following way:

- $HSO_4{}^{-}$ is the primary dissociation product of $H_2SO_4$. The latter is a strong acid which is assumed to dissociate completely, producing $H^+$ and $HSO_4{}^{-}$ at the same experimental bulk concentration: $[HSO_4{}^{-}] = [H^+] = 0.05$ mol $L^{-1}$.
- $SO_4{}^{2-}$ is obtained from the dissociation of the weak acid $HSO_4{}^{-}$:

  $$HSO_4{}^{-} \longrightarrow SO_4{}^{2-} + H^+$$

  its bulk concentration value is determined the acidic dissociation constant $K_a$ of $HSO_4{}^{-}$:

  $$K_a = \frac{[SO_4{}^{2-}][H^+]}{[HSO_4{}^{-}]} = 0.01 \text{ mol } L^{-1}$$

  since $[HSO_4{}^{-}] = [H^+]$:

  $$[SO_4{}^{2-}] = K_a = 0.01 \text{ mol } L^{-1}$$

Their adsorption is described by the following electrochemical processes:

$$* + HSO_4{}^{-} \longrightarrow *HSO_4 + e^-$$

$$* + {SO_4}^{2-} \longrightarrow *SO_4 + 2e^-$$
$$* + {HSO_4}^{-} \longrightarrow *SO_4 + H^+ + e^-$$
$$* + {SO_4}^{2-} + H^+ \longrightarrow *HSO_4 + e^-$$

Where $*HSO_4$ and $*SO_4$ represent the surface with the ions adsorbed in neutral charge state.

The resulting ESPD slice is shown in Fig. 7.17b. Given the strong affinity of Au towards ${HSO_4}^{-}$, its adsorption is favourable at relatively low potentials, in agreement with the experimental observations. The electrochemical conversion of ${HSO_4}^{-}$ into ${SO_4}^{2-}$ is predicted to prevail at $U = 1.15$ V, possibly explaining the CV peak at $U = 0.9$ V, although its position is not predicted accurately. Two additional phase boundaries are found at $U = 1.3$ V and $U = 1.65$ V, associated with OH and O adsorption, respectively. Overall, the ESPD predictions now agree with the experimental CV in the number of oxidation peaks, although their positions differ.

In a final iteration, we account for solvation effects by including a monolayer of adsorbed water in each configuration. Adsorption configurations are modeled by replacing different numbers of $H_2O$ molecules with the adsorbates according to the coverage (note that ${HSO_4}^{-}$ and ${SO_4}^{2-}$ occupy three adsorption sites). The resulting energy diagram is shown in Fig. 7.17c.

Interestingly, the solvation layer stabilizes ${SO_4}^{2-}$ adsorption relative to ${HSO_4}^{-}$, shifting the corresponding phase boundary to the lower potential value of $U = 0.9$ V. Water molecules seem to lock ${SO_4}^{2-}$ in a more symmetrical configuration compared to ${HSO_4}^{-}$, possibly justifying the disordered-to-ordered transition in the adsorbate layer observed experimentally.

A second phase boundary is now found at $U = 1.2$ V, associated with OH adsorption at 1/2ML. The OH adsorbates sit at the same distance from the surface as the $H_2O$ molecules in the solvation layer (about 2.2 Å ), suggesting that their bonding to the Au atoms is weak and governed by the same dispersive interactions. This supports the attribution of the CV peak at 1.2 V to weakly adsorbed species, not yet confirmed by experiments.

The last phase boundary is found at $U = 1.7$ V. At this potential, Au dissolution into $Au(OH)_3$ is the most favourable process. The resulting Au vacancies are possibly stabilized by the surrounding solvent molecules. As previously discussed, vacancy formation can explain the experimental peak at $U = 1.7$ V.

The ESPD obtained with this final set of configurations provides excellent qualitative and quantitative agreement with the CV scan. Additionally, the atomic structures associated with the stability domains seem to support the assignment from the experimental counterpart and the supporting spectroscopic and microscopic data.

The results presented in this section have been obtained in collaboration with Sara Barja Martinez and Jesus Maria Lopez Redondo at the *Centro de Fisica de Materiales* (CFM) in San Sebastian (Spain).

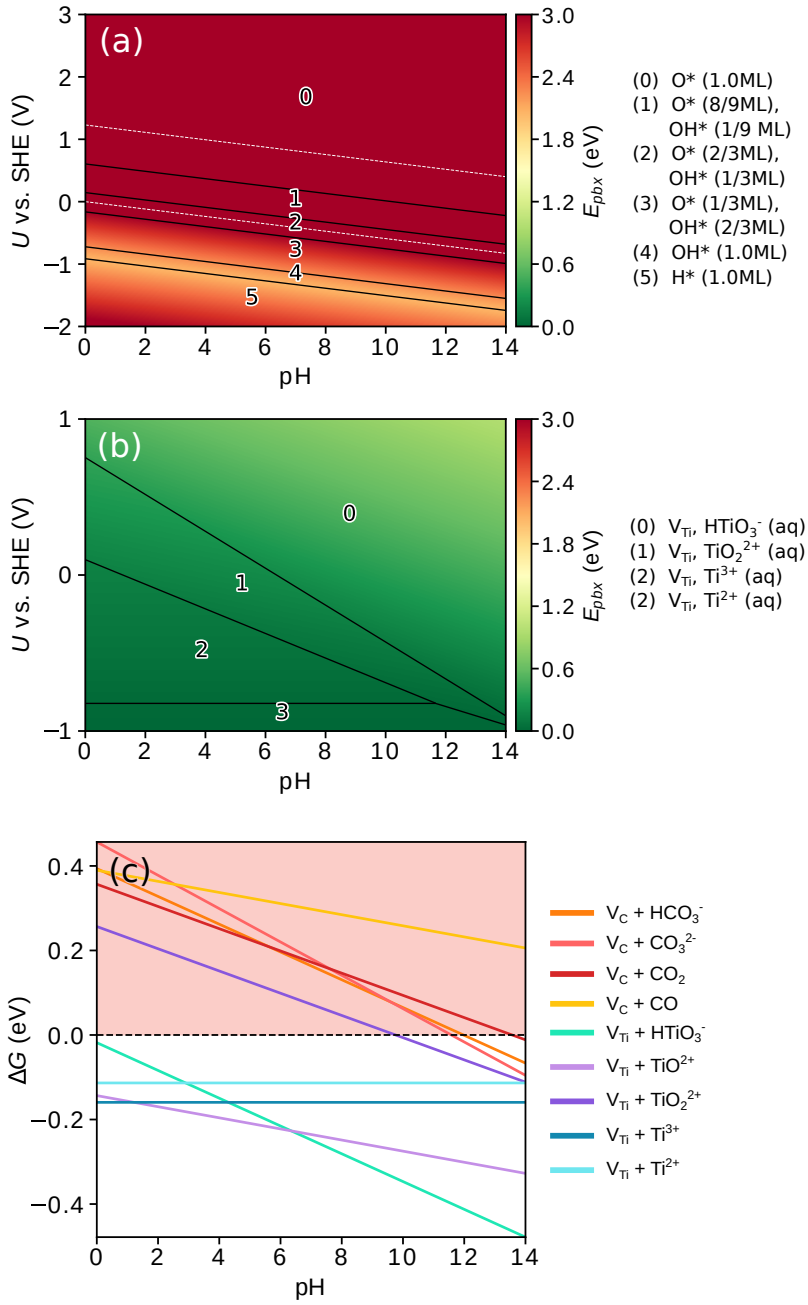


**Figure 7.15:** a) ESPD of $Ti_2C$. Potentials are reported vs. SHE. The upper and lower dashed lines represent the $H^+/H_2$ and $O_2/H_2O$ equilibrium potential, respectively. b) ESPD of $Ti_2C$ at potentials between -1 and +1 vs. SHE, obtained without considering adsorption processes. c) slice of the $Ti_2C$ ESPD at $U = 0$ vs. Pt. The diagram has been calculated without considering adsorption processes.

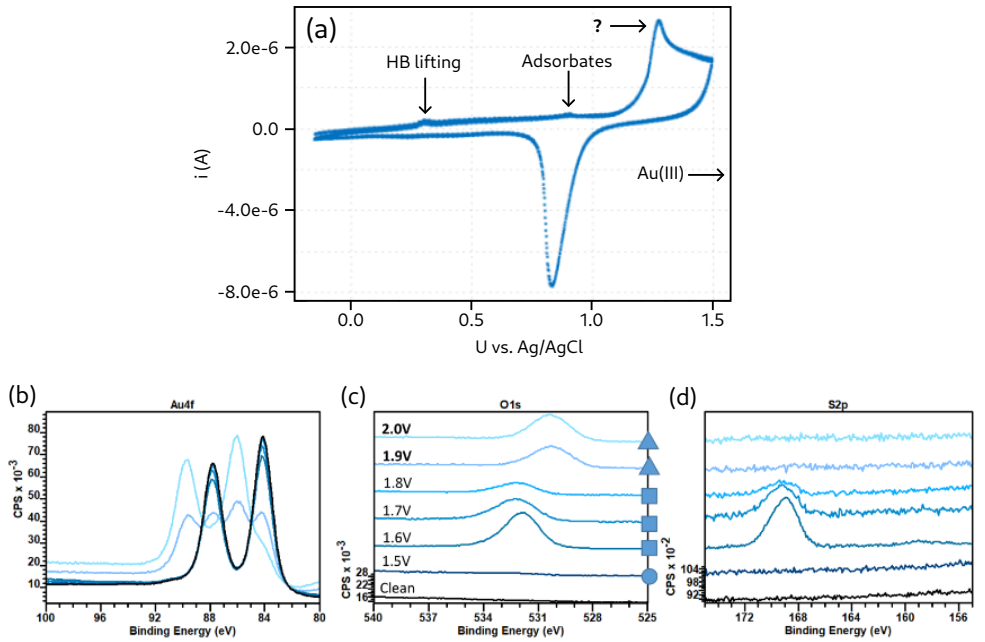


**Figure 7.16:** (a) Experimental CV scan against Ag/AgCl at pH 1.3. The peaks are labeled with the experimental attribution. Bottom panels: Au $4f$ (panel b), O $1s$ (panel c) and S $2p$ (panel d) XPS spectra. Different colors correspond to different potentials, consistently with panel (d). .

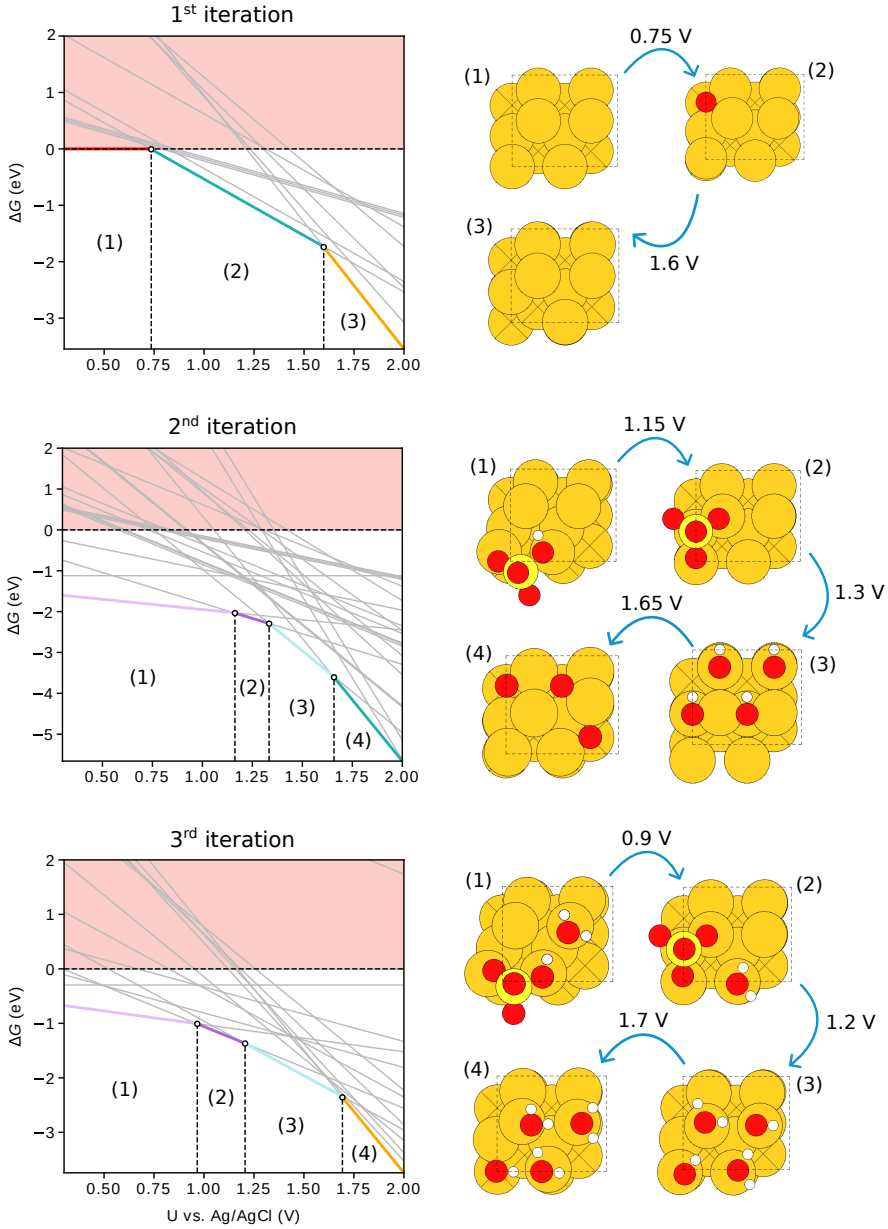


**Figure 7.17:** ESPD slice at pH 1.3 of a gold surface, with potentials referenced to the Ag/AgCl electrode. The three panels report the slices obtained at different iterations of the method, *i.e.* by using difference sets of surface configurations. At each iteration, the description of the Au surface is improved. The atomic structures associated with the different stability domains are reported on the right of each diagram. Only the thermodynamically most stable phases are reported, the others are represented by grey lines. Blue arrows indicate the order in which the configurations are encountered at increasing potentials. On top of the arrows, the potentials corresponding to the phase boundaries are reported .

# Bibliography


[1] J. K. Nørskov, T. Bligaard, A. Logadottir, J. Kitchin, J. G. Chen, S. Pandelov, and U. Stimming, "Trends in the exchange current for hydrogen evolution," Journal of The Electrochemical Society **152**, J23 (2005).

[2] K. S. Novoselov, A. K. Geim, S. V. Morozov, D. Jiang, Y. Zhang, S. V. Dubonos, I. V. Grigorieva, and A. A. Firsov, "Electric field effect in atomically thin carbon films," science **306**, 666 (2004).

[3] K. Novoselov, A. Mishchenko, A. Carvalho, and A. Castro Neto, "2d materials and van der waals heterostructures," Science **353**, aac9439 (2016).

[4] M. Khazaei, A. Ranjbar, M. Arai, T. Sasaki, and S. Yunoki, "Electronic properties and applications of mxenes: a theoretical review," Journal of Materials Chemistry C **5**, 2488 (2017).

[5] A. K. Geim and I. V. Grigorieva, "Van der waals heterostructures," Nature **499**, 419 (2013).

[6] P. Hohenberg and W. Kohn, "Inhomogeneous electron gas," Physical review **136**, B864 (1964).

[7] W. Kohn and L. J. Sham, "Self-consistent equations including exchange and correlation effects," Physical review **140**, A1133 (1965).

[8] J. P. Perdew, K. Burke, and M. Ernzerhof, "Generalized gradient approximation made simple," Physical review letters **77**, 3865 (1996).

[9] X. Li, X. Hao, A. Abudula, and G. Guan, "Nanostructured catalysts for electrochemical water splitting: current state and prospects," Journal of Materials Chemistry A **4**, 11973 (2016).

[10] Y.-W. Lee, A.-R. Ko, S.-B. Han, H.-S. Kim, and K.-W. Park, "Synthesis of octahedral pt–pd alloy nanoparticles for improved catalytic activity and stability in methanol electrooxidation," Physical Chemistry Chemical Physics **13**, 5569 (2011).

[11] S. R. Ede and Z. Luo, "Tuning the intrinsic catalytic activities of oxygen-evolution catalysts by doping: a comprehensive review," Journal of Materials Chemistry A **9**, 20131 (2021).

[12] H.-l. Liu, F. Nosheen, and X. Wang, "Noble metal alloy complex nanostructures: controllable synthesis and their electrochemical property," Chemical Society Reviews **44**, 3056 (2015).

[13] G. Hai, X. Xue, S. Feng, Y. Ma, and X. Huang, "High-throughput computational screening of metal–organic frameworks as high-performance electrocatalysts for co2rr," ACS Catalysis **12**, 15271 (2022).

[14] D. Jin, L. R. Johnson, A. S. Raman, X. Ming, Y. Gao, F. Du, Y. Wei, G. Chen, A. Vojvodic, Y. Gogotsi, et al., "Computational screening of 2d ordered double transition-metal carbides (mxenes) as electrocatalysts for hydrogen evolution reaction," The Journal of Physical Chemistry C **124**, 10584 (2020).

[15] X.-B. Li, T. Cao, F. Zheng, and X. Chen, "Computational screening of electrocatalytic materials for hydrogen evolution: platinum monolayer on transitional metals," The Journal of Physical Chemistry C **123**, 495 (2018).

[16] R. M. Ormerod, "Solid oxide fuel cells," Chemical Society Reviews **32**, 17 (2003).

[17] K. S. Santhanam, R. J. Press, M. J. Miri, A. V. Bailey, and G. A. Takacs, *Introduction to hydrogen technology* (John Wiley & Sons, 2017).

[18] H. Wendt, E. V. Spinacé, A. Oliveira Neto, and M. Linardi, "Electrocatalysis and electrocatalysts for low temperature fuel cells: fundamentals, state of the art, research and development," Química Nova **28**, 1066 (2005).

[19] Y. Lee, J. Suntivich, K. J. May, E. E. Perry, and Y. Shao-Horn, "Synthesis and activities of rutile iro2 and ruo2 nanoparticles for oxygen evolution in acid and alkaline solutions," The journal of physical chemistry letters **3**, 399 (2012).

[20] C. C. McCrory, S. Jung, I. M. Ferrer, S. M. Chatman, J. C. Peters, and T. F. Jaramillo, "Benchmarking hydrogen evolving reaction and oxygen evolving reaction electrocatalysts for solar water splitting devices," Journal of the American Chemical Society **137**, 4347 (2015).

[21] Z.-P. Wu, X. F. Lu, S.-Q. Zang, and X. W. Lou, "Non-noble-metal-based electrocatalysts toward the oxygen evolution reaction," Advanced Functional Materials **30**, 1910274 (2020).

[22] J. D. Benck, T. R. Hellstern, J. Kibsgaard, P. Chakthranont, and T. F. Jaramillo, "Catalyzing the hydrogen evolution reaction (her) with molybdenum sulfide nanomaterials," Acs Catalysis **4**, 3957 (2014).

[23] Z. W. Seh, J. Kibsgaard, C. F. Dickens, I. Chorkendorff, J. K. Nørskov, and T. F. Jaramillo, "Combining theory and experiment in electrocatalysis: insights into materials design," Science **355**, eaad4998 (2017).

[24] R. Parsons, "The rate of electrolytic hydrogen evolution and the heat of adsorption of hydrogen," Transactions of the Faraday Society **54**, 1053 (1958).

[25] J. Rossmeisl, A. Logadottir, and J. K. Nørskov, "Electrolysis of water on (oxidized) metal surfaces," Chemical physics **319**, 178 (2005).

[26] Q. Liang, G. Brocks, and A. Bieberle-Hütter, "Oxygen evolution reaction (oer) mechanism under alkaline and acidic conditions," Journal of Physics: Energy **3**, 026001 (2021).

[27] Z. Shi, X. Wang, J. Ge, C. Liu, and W. Xing, "Fundamental understanding of the acidic oxygen evolution reaction: mechanism study and state-of-the-art catalysts," Nanoscale **12**, 13249 (2020).

[28] V. Viswanathan, H. A. Hansen, J. Rossmeisl, and J. K. Nørskov, "Universality in oxygen reduction electrocatalysis on metal surfaces," Acs Catalysis **2**, 1654 (2012).

[29] C. Spöri, J. T. H. Kwan, A. Bonakdarpour, D. P. Wilkinson, and P. Strasser, "The stability challenges of oxygen evolving catalysts: towards a common fundamental understanding and mitigation of catalyst degradation," Angewandte Chemie International Edition **56**, 5994 (2017).

[30] M. Pourbaix, "Atlas of electrochemical equilibria in aqueous solutions," NACE (1966).

[31] A. H. Larsen, J. J. Mortensen, J. Blomqvist, I. E. Castelli, R. Christensen, M. Dułak, J. Friis, M. N. Groves, B. Hammer, C. Hargus, et al., "The atomic simulation environment—a python library for working with atoms," Journal of Physics: Condensed Matter **29**, 273002 (2017).

[32] D. Zagorac, H. Müller, S. Ruehl, J. Zagorac, and S. Rehme, "Recent developments in the inorganic crystal structure database: theoretical crystal structure data and related features," Journal of applied crystallography **52**, 918 (2019).

[33] S. Gražulis, A. Daškevič, A. Merkys, D. Chateigner, L. Lutterotti, M. Quirós, N. R. Serebryanaya, P. Moeck, R. T. Downs, and A. Le Bail, "Crystallography open database (cod): an open-access collection of crystal structures and platform for world-wide collaboration," Nucleic Acids Research **40**, D420 (2012).

[34] *Nist chemistry webbook*, https://webbook.nist.gov/chemistry/.

[35] J. E. Saal, S. Kirklin, M. Aykol, B. Meredig, and C. Wolverton, "Materials design and discovery with high-throughput density functional theory: the open quantum materials database (oqmd)," Jom **65**, 1501 (2013).

[36] A. Jain, S. P. Ong, G. Hautier, W. Chen, W. D. Richards, S. Dacek, S. Cholia, D. Gunter, D. Skinner, G. Ceder, and K. a. Persson, "The Materials Project: A materials genome approach to accelerating materials innovation," APL Materials **1**, 011002 (2013).

[37] S. Haastrup, M. Strange, M. Pandey, T. Deilmann, P. S. Schmidt, N. F. Hinsche, M. N. Gjerding, D. Torelli, P. M. Larsen, A. C. Riis-Jensen, et al., "The computational 2d materials database: high-throughput modeling and discovery of atomically thin crystals," 2D Materials **5**, 042002 (2018).

[38] M. N. Gjerding, A. Taghizadeh, A. Rasmussen, S. Ali, F. Bertoldo, T. Deilmann, N. R. Knøsgaard, M. Kruse, A. H. Larsen, S. Manti, et al., "Recent progress of the computational 2d materials database (c2db)," 2D Materials **8**, 044002 (2021).

[39] A. M. Patel, J. K. Nørskov, K. A. Persson, and J. H. Montoya, "Efficient pourbaix diagrams of many-element compounds," Physical Chemistry Chemical Physics **21**, 25323 (2019).

[40] M. Sankar, J. Macaskill, and R. G. Bates, "Standard potential of the silver-silver chloride electrode in 10, 20, and 40 wt.% ethanol/water solvents at 25, 0,- 5, and-10° c," Journal of Solution Chemistry **8**, 887 (1979).

[41] Y. Liu, Y. Zhao, X. Zhang, X. Huang, W. Liao, and Y. Zhao, "Mos2-based membranes in water treatment and purification," Chemical Engineering Journal **422**, 130082 (2021).

[42] Q. Ding, B. Song, P. Xu, and S. Jin, "Efficient electrocatalytic and photoelectrochemical hydrogen generation using mos2 and related compounds," Chem **1**, 699 (2016).

[43] E. Parzinger, B. Miller, B. Blaschke, J. A. Garrido, J. W. Ager, A. Holleitner, and U. Wurstbauer, "Photocatalytic stability of single-and few-layer mos2," ACS nano **9**, 11302 (2015).

[44] M. Parashar, V. K. Shukla, and R. Singh, "Metal oxides nanoparticles via sol–gel method: a review on synthesis, characterization and applications," Journal of Materials Science: Materials in Electronics **31**, 3729 (2020).

[45] K. S. Williams, J. P. Labukas, V. Rodriguez-Santiago, and J. W. Andzelm, "First principles modeling of water dissociation on mg (0001) and development of a mg surface pourbaix diagram," Corrosion **71**, 209 (2015).

[46] M. López, K. S. Exner, F. Viñes, and F. Illas, "Computational pourbaix diagrams for mxenes: a key ingredient toward proper theoretical electrocatalytic studies," Advanced Theory and Simulations, 2200217 (2022).

[47] Z. Li, F. Chen, W. Bian, B. Kou, Q. Wang, L. Guo, T. Jin, Q. Tang, and B. Pan, "Surface pourbaix diagram of agpd nanoalloys and its application in formate oxidation reaction," Electrochimica Acta **386**, 138465 (2021).

[48] H. A. Hansen, J. Rossmeisl, and J. K. Nørskov, "Surface pourbaix diagrams and oxygen reduction activity of pt, ag and ni (111) surfaces studied by dft," Physical Chemistry Chemical Physics **10**, 3722 (2008).

[49] S. Trasatti, "The absolute electrode potential: an explanatory note (recommendations 1986)," Pure and Applied Chemistry **58**, 955 (1986).

[50] S. Grimme, J. Antony, S. Ehrlich, and H. Krieg, "A consistent and accurate ab initio parametrization of density functional dispersion correction (dft-d) for the 94 elements h-pu," The Journal of chemical physics **132** (2010).

[51] K. F. Mak, C. Lee, J. Hone, J. Shan, and T. F. Heinz, "Atomically thin mos 2: a new direct-gap semiconductor," Physical review letters **105**, 136805 (2010).

[52] A. Ramasubramaniam, "Large excitonic effects in monolayers of molybdenum and tungsten dichalcogenides," Physical Review B **86**, 115409 (2012).

[53] D. Y. Qiu, H. Felipe, and S. G. Louie, "Optical spectrum of mos 2: many-body effects and diversity of exciton states," Physical review letters **111**, 216805 (2013).

[54] L. Ponomarenko, A. Geim, A. Zhukov, R. Jalil, S. Morozov, K. Novoselov, I. Grigorieva, E. Hill, V. Cheianov, V. Fal'Ko, et al., "Tunable metal–insulator transition in double-layer graphene heterostructures," Nature Physics **7**, 958 (2011).

[55] S. Haigh, A. Gholinia, R. Jalil, S. Romani, L. Britnell, D. Elias, K. Novoselov, L. Ponomarenko, A. Geim, and R. Gorbachev, "Cross-sectional imaging of individual layers and buried interfaces of graphene-based heterostructures and superlattices," Nature materials **11**, 764 (2012).

[56] C. R. Dean, A. F. Young, I. Meric, C. Lee, L. Wang, S. Sorgenfrei, K. Watanabe, T. Taniguchi, P. Kim, K. L. Shepard, et al., "Boron nitride substrates for high-quality graphene electronics," Nature nanotechnology **5**, 722 (2010).

[57] S. Mouri, W. Zhang, D. Kozawa, Y. Miyauchi, G. Eda, and K. Matsuda, "Thermal dissociation of inter-layer excitons in mos 2/mose 2 hetero-bilayers," Nanoscale **9**, 6674 (2017).

[58] H. Fang, C. Battaglia, C. Carraro, S. Nemsak, B. Ozdol, J. S. Kang, H. A. Bechtel, S. B. Desai, F. Kronast, A. A. Unal, et al., "Strong interlayer coupling in van der waals heterostructures built from single-layer chalcogenides," Proceedings of the National Academy of Sciences **111**, 6198 (2014).

[59] H. Heo, J. H. Sung, G. Jin, J.-H. Ahn, K. Kim, M.-J. Lee, S. Cha, H. Choi, and M.-H. Jo, "Rotation-misfit-free heteroepitaxial stacking and stitching growth of hexagonal transition-metal dichalcogenide monolayers by nucleation kinetics controls," Advanced Materials **27**, 3803 (2015).

[60] E. M. Alexeev, A. Catanzaro, O. V. Skrypka, P. K. Nayak, S. Ahn, S. Pak, J. Lee, J. I. Sohn, K. S. Novoselov, H. S. Shin, et al., "Imaging of interlayer coupling in van der waals heterostructures using a bright-field optical microscope," Nano letters **17**, 5342 (2017).

[61] J. Kunstmann, F. Mooshammer, P. Nagler, A. Chaves, F. Stein, N. Paradiso, G. Plechinger, C. Strunk, C. Schüller, G. Seifert, et al., "Momentum-space indirect interlayer excitons in transition-metal dichalcogenide van der waals heterostructures," Nature Physics **14**, 801 (2018).

[62] E. M. Alexeev, D. A. Ruiz-Tijerina, M. Danovich, M. J. Hamer, D. J. Terry, P. K. Nayak, S. Ahn, S. Pak, J. Lee, J. I. Sohn, et al., "Resonantly hybridized excitons in moiré superlattices in van der waals heterostructures," Nature **567**, 81 (2019).

[63] D. S. Koda, F. Bechstedt, M. Marques, and L. K. Teles, "Coincidence lattices of 2d crystals: heterostructure predictions and applications," The Journal of Physical Chemistry C **120**, 10895 (2016).

[64] M. Gjerding, T. Skovhus, A. Rasmussen, F. Bertoldo, A. H. Larsen, J. J. Mortensen, and K. S. Thygesen, "Atomic simulation recipes: a python framework and library for automated workflows," Computational Materials Science **199**, 110731 (2021).

[65] T. Cheiwchanchamnangij and W. R. Lambrecht, "Quasiparticle band structure calculation of monolayer, bilayer, and bulk mos 2," Physical Review B **85**, 205302 (2012).

[66] X. Zhao, P. Song, C. Wang, A. C. Riis-Jensen, W. Fu, Y. Deng, D. Wan, L. Kang, S. Ning, J. Dan, et al., "Engineering covalently bonded 2d layered materials by self-intercalation," Nature **581**, 171 (2020).

[67] F. Cui, X. Zhao, J. Xu, B. Tang, Q. Shang, J. Shi, Y. Huan, J. Liao, Q. Chen, Y. Hou, et al., "Controlled growth and thickness-dependent conduction-type transition of 2d ferrimagnetic cr2s3 semiconductors," Advanced Materials **32**, 1905896 (2020).

[68] H. Li, L. Wang, J. Chen, T. Yu, L. Zhou, Y. Qiu, H. He, F. Ye, I. K. Sou, and G. Wang, "Molecular beam epitaxy grown cr2te3 thin films with tunable curie temperatures for spintronic devices," ACS Applied Nano Materials **2**, 6809 (2019).

[69] Y. Wen, Z. Liu, Y. Zhang, C. Xia, B. Zhai, X. Zhang, G. Zhai, C. Shen, P. He, R. Cheng, et al., "Tunable room-temperature ferromagnetism in two-dimensional cr2te3," Nano Letters **20**, 3130 (2020).

[70] K. Lasek, P. M. Coelho, K. Zberecki, Y. Xin, S. K. Kolekar, J. Li, and M. Batzill, "Molecular beam epitaxy of transition metal (ti-, v-, and cr-) tellurides: from monolayer ditellurides to multilayer self-intercalation compounds," ACS nano **14**, 8473 (2020).

[71] K. Lasek, P. M. Coelho, P. Gargiani, M. Valvidares, K. Mohseni, H. L. Meyerheim, I. Kostanovskiy, K. Zberecki, and M. Batzill, "Van der waals epitaxy growth of 2d ferromagnetic cr(1+ $\delta$)te2 nanolayers with concentration-tunable magnetic anisotropy," Applied Physics Reviews **9**, 011409 (2022).

[72] J. Yang, A. R. Mohmad, Y. Wang, R. Fullon, X. Song, F. Zhao, I. Bozkurt, M. Augustin, E. J. Santos, H. S. Shin, et al., "Ultrahigh-current-density niobium disulfide catalysts for hydrogen evolution," Nature Materials **18**, 1309 (2019).

[73] Q.-Q. Li, S. Li, D. Wu, Z.-K. Ding, X.-H. Cao, L. Huang, H. Pan, B. Li, K.-Q. Chen, and X.-D. Duan, "Magnetic properties manipulation of crte2 bilayer through strain and self-intercalation," Applied Physics Letters **119**, 162402 (2021).

[74] R. Li, J. Jiang, H. Bai, and W. Mi, "Tailoring interlayer magnetic coupling to modify the magnetic properties of fecl 2 bilayers by self-intercalation," Journal of Materials Chemistry C **10**, 14955 (2022).

[75] Y. Guo, N. Liu, Y. Zhao, X. Jiang, S. Zhou, and J. Zhao, "Enhanced ferromagnetism of cri3 bilayer by self-intercalation," Chinese Physics Letters **37**, 107506 (2020).

[76] X. Li and H. Zhu, "Two-dimensional mos2: properties, preparation, and applications," Journal of Materiomics **1**, 33 (2015).

[77] K. Krishnamoorthy, G. K. Veerasubramani, S. Radhakrishnan, and S. J. Kim, "Supercapacitive properties of hydrothermally synthesized sphere like mos2 nanostructures," Materials Research Bulletin **50**, 499 (2014).

[78] R. Pujari, A. Lokhande, A. Shelke, J. Kim, and C. Lokhande, "Chemically deposited nano grain composed mos2 thin films for supercapacitor application," Journal of colloid and interface science **496**, 1 (2017).

[79] C. Tsai, H. Li, S. Park, J. Park, H. S. Han, J. K. Nørskov, X. Zheng, and F. Abild-Pedersen, "Electrochemical generation of sulfur vacancies in the basal plane of mos2 for hydrogen evolution," Nature communications **8**, 15113 (2017).

[80] H. Liu, A. T. Neal, Z. Zhu, Z. Luo, X. Xu, D. Tománek, and P. D. Ye, "Phosphorene: an unexplored 2d semiconductor with a high hole mobility," ACS nano **8**, 4033 (2014).

[81] A. Carvalho, M. Wang, X. Zhu, A. S. Rodin, H. Su, and A. H. Castro Neto, "Phosphorene: from theory to applications," Nature Reviews Materials **1**, 1 (2016).

[82] V. Eswaraiah, Q. Zeng, Y. Long, and Z. Liu, "Black phosphorus nanosheets: synthesis, characterization and applications," Small **12**, 3480 (2016).

[83] J. D. Wood, S. A. Wells, D. Jariwala, K.-S. Chen, E. Cho, V. K. Sangwan, X. Liu, L. J. Lauhon, T. J. Marks, and M. C. Hersam, "Effective passivation of exfoliated black phosphorus transistors against ambient degradation," Nano letters **14**, 6964 (2014).

[84] F. Ming, H. Liang, G. Huang, Z. Bayhan, and H. N. Alshareef, "Mxenes for rechargeable batteries beyond the lithium-ion," Advanced Materials **33**, 2004039 (2021).

[85] E. Lee, A. VahidMohammadi, B. C. Prorok, Y. S. Yoon, M. Beidaghi, and D.-J. Kim, "Room temperature gas sensing of two-dimensional titanium carbide (mxene)," ACS applied materials & interfaces **9**, 37184 (2017).

[86] Q. Zhong, Y. Li, and G. Zhang, "Two-dimensional mxene-based and mxene-derived photocatalysts: recent developments and perspectives," Chemical Engineering Journal **409**, 128099 (2021).

[87] F. Xia, J. Lao, R. Yu, X. Sang, J. Luo, Y. Li, and J. Wu, "Ambient oxidation of ti 3 c 2 mxene initialized by atomic defects," Nanoscale **11**, 23330 (2019).

[88] C. J. Zhang, S. Pinilla, N. McEvoy, C. P. Cullen, B. Anasori, E. Long, S.-H. Park, A. Seral-Ascaso, A. Shmeliov, D. Krishnan, et al., "Oxidation stability of colloidal two-dimensional titanium carbides (mxenes)," Chemistry of Materials **29**, 4848 (2017).

[89] Z. W. Seh, K. D. Fredrickson, B. Anasori, J. Kibsgaard, A. L. Strickler, M. R. Lukatskaya, Y. Gogotsi, T. F. Jaramillo, and A. Vojvodic, "Two-dimensional molybdenum carbide (mxene) as an efficient electrocatalyst for hydrogen evolution," ACS Energy Letters **1**, 589 (2016).

[90] G. Gao, A. P. O'Mullane, and A. Du, "2d mxenes: a new family of promising catalysts for the hydrogen evolution reaction," Acs Catalysis **7**, 494 (2017).

[91] S. Narasimhan and D. Vanderbilt, "Elastic stress domains and the herringbone reconstruction on au(111)," Phys. Rev. Lett. **69**, 1564 (1992).

CHAPTER 8

# Publication I

*Functionalised 2D materials: Enhancing metallicity and chemical reactivity via self-intercalation*

# Enhancing metallicity and basal plane reactivity of 2D materials via self-intercalation

Stefano Americo,* Sahar Pakdel, and Kristian Sommer Thygesen

*Computational Atomic-scale Materials Design (CAMD), Department of Physics, Technical University of Denmark, 2800 Kgs. Lyngby Denmark*

E-mail: steame@dtu.dk

## Abstract

Intercalation (ic) of metal atoms into the van der Waals (vdW) gap of layered materials constitutes a facile strategy to create new materials whose properties can be tuned via the concentration of the intercalated atoms. Here we perform systematic density functional theory calculations to explore various properties of an emergent class of crystalline 2D materials (ic-2D materials) comprising vdW homobilayers with native metal atoms on a sublattice of intercalation sites. From an initial set of 1348 ic-2D materials, generated from 77 vdW homobilayers, we find 95 structures with good thermodynamic stability (formation energy within 200 meV/atom of the convex hull). A significant fraction of the semiconducting host materials are found to undergo an insulator to metal transition upon self-intercalation with only $PdS_2$, $PdSe_2$, and $GeS_2$ maintaining a finite electronic gap. In five cases, self-intercalation introduces magnetism. In general, self-intercalation is found to promote metallicity and enhance the chemical reactivity on the basal plane. Based on the calculated H binding energy we find that self-intercalated $SnS_2$ and $Hf_3Te_2$ are promising candidates for hydrogen evolution catalysis. All the stable ic-2D structures and their calculated properties can be explored

in the open C2DB database.

# Introduction

Atomically thin two-dimensional (2D) materials exhibit unique physical properties that could form the basis for future generations of ultra-compact devices with novel functionalities or architecture designs.[1–4] Moreover, the extreme surface area-to-volume ratio makes 2D materials natural candidates for chemical sensors[5,6] and (electro)catalysts[7–12] – in particular if their basal planes could be activated.[13,14] So far, most research has focused on 2D monolayers and their stacked homo- or heterostructures.[15,16] While stacking can be used to modulate the electronic and optical properties of 2D materials,[17–19] the effects are relatively limited due to the weakness of the interlayer van der Waals (vdW) interactions. An alternative functionalisation strategy consists in intercalating foreign or native atoms into the vdW gap of a multi-layer structure. In general, this scheme can produce significant changes to the materials properties thanks to the strong covalent bonds formed between the host 2D layers and the intercalated atoms.[20–22] In particular, it is expected that intercalation can enhance interlayer interactions, induce doping of the 2D materials, strongly modify their electronic structure and chemical reactivity, or even convert them into distinctly different structural phases.

Self-intercalation, i.e. intercalation of native metal atoms, has recently emerged as an effective technique to produce new types of covalently bonded, crystalline 2D materials (referred to as ic-2D materials) with stoichiometry dependent properties.[23] This approach is interesting for several reasons: (1) Intercalation in few-layer structures, in particular bilayers, provides an effective way to expand the family of atomically thin 2D materials. (2) The properties of ic-2D materials can be tuned by varying the concentration of intercalated atoms, i.e. the stoichiometry. (3) ic-2D materials with different stoichiometries, including the parent vdW host structure, belong to the same compositional space yet may exhibit com-

plementary properties. In particular, they share the same chemical elements and have similar lattice constants, but may be metallic or insulating, magnetic or non-magnetic, and show different chemical properties depending on the stoichiometry. Such compatible/complementary material sets are ideal for device construction.

Zhao *et al.* produced a range of ic-2D materials, in particular $TaS_2$ and $TaSe_2$ with various concentrations of intercalated Ta, using both molecular beam epitaxy (MBE) and chemical vapour deposition (CVD).[23] In these experiments, the stoichiometry was controlled during growth by tuning the relative chemical potentials of Ta and S/Se, and the resulting ic-2D materials showed stoichiometry-dependent crystal structures and magnetism. There have been several reports on CVD and MBE grown few-layer $Cr_2Te_3$, which is a self-intercalated version of the vdW crystal $CrTe_2$, showing thickness dependent conduction behaviour (from n- to p-type)[24] and tunable ferromagnetism down to the limit of intercalated bilayers.[25–27] It has been shown that self-intercalation compounds competes with and often dominates over multilayer vdW crystals during direct MBE growth of the early transition metal (Ti, V, Cr) ditellurides.[28] Yang *et al.* showed that Nb intercalation can dramatically increase the catalytic activity of the vdW crystal $NbS_2$ for the hydrogen evolution reaction.[14]

In addition to these experimental studies, density functional theory calculations have shown that self-intercalation can modulate and enhance the interlayer exchange interaction and the magnetic anisotropy in intrinsically magnetic vdW materials such as $CrTe_2$,[29] $FeCl_2$,[30] and $CrI_3$.[31]

In this work we, perform a systematic exploration of ic-2D materials and their stoichiometry-dependent properties using density functional theory (DFT) calculations. Starting from 77 binary vdW bilayers, we insert native metal atoms in the vdW gap in various concentrations and determine the stability of the resulting crystal structures. For the most stable compounds, we compute a range of properties including the mechanical stiffness, electronic band structures, magnetic moments, and basal plane reactivity (defined from the adsorption energy of H). Out of 23 semiconducting vdW bilayers, 20 undergo an insulator-to-metal

transition upon self-intercalation. This transition is clearly correlated with an increase in the H binding energy. Our results show that intercalation is an efficient means to activate the basal plane of 2D materials. Specifically, we identify seven ic-2D materials (involving five different host systems) as promising electrocatalysts for the hydrogen evolution reaction.

## Results and discussion

We start by describing the workflow used to set up the ic-2D structures. In the subsequent sections, we discuss the thermodynamic stability of the resulting ic-2D structure and their agreement with available experimental data before we explore their electronic properties and potential as electrocatalysts for the hydrogen evolution reaction.

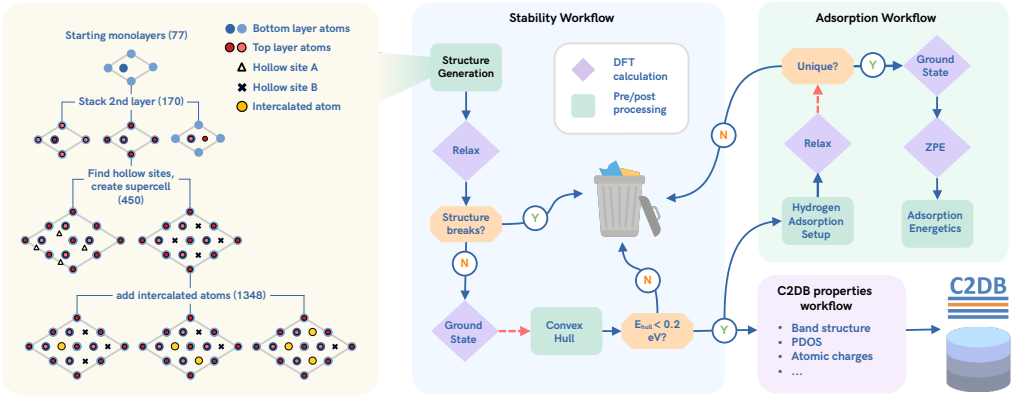


Figure 1: Workflow for calculation of the ic-2D properties, including a schematic representation of the structure generation procedure. The numbers in parentheses represent the number of structures generated at each step. Red dashed arrow represent bottlenecks in the workflow, where all the previous steps have to be completed for the related ic-2D structures before proceeding to the following steps.

**Intercalation workflow** All the ic-2D bilayer structures are generated starting from a set of parent monolayers (ML) selected from the Computational 2D Material Database (C2DB)[32,33] according to the following criteria:

a) At most two different chemical species ($A_xB_y$).

b) Good thermodynamic stability. Specifically, the energy above the convex hull of the ML ($\Delta H_{\text{hull}}$) is below 100 meV/atom.

c) Dynamical stability, i.e. all phonon energies of the ML should be real and positive.

d) Maximum six atoms per unit cell in the ML. This condition limits the complexity of the resulting ic-2D structures and the computational demands.

e) The material should be experimentally known in few-layer or bulk form. In practice this means that all the materials are reported in either the ICSD[34] and/or the COD[35] crystal structure databases and/or can have been explored experimentally and reported in the literature.

f) The ML does not contain rare[36] or toxic elements. The blacklisted elements are Cd, Pb, Hg, Pt, Au, Os, Ru, Ir, Rh, Re, Kr, Xe. All materials are thus ensured to be obtainable from earth-abundant elements and suitable for sustainable applications.

These preliminary selection criteria result in a set of 77 MLs. The ic-2D bilayer generation procedure follows the scheme illustrated in Fig. 1 (left). For each of the MLs, we obtain a set of vdW homobilayers corresponding to the most stable stacking configurations as defined by Pakdel.[37] For each stacking, we automatically identify all the hollow sites in the vdW gap region that are inequivalent by symmetry (see Methods section for a description of the software framework in use). We then determine a suitable supercell containing at least three sites for each hollow site type, typically resulting in a $(\sqrt{3} \times \sqrt{3})$R30 or a 2×2 supercell depending on the host bilayer cell symmetry. For each hollow site type, we then generate ic-2D bilayers with different concentrations of intercalated atoms.

Defining the ic-fraction as the number of intercalated atoms per primitive unit cell of the bilayer host (for instance a 2×2 supercell with one intercalated atom will have an ic-fraction of 0.25), we obtain fractions in the 0.25 - 1.0 range, which are comparable with the ones typically realized in experiments.[14,23,28] In the following, this fraction will sometimes be referred to as a percentage or ic-concentration. We note that the relatively high concentrations considered implies that the ic-atoms should not be regarded as point defects/impurities. Rather, they

form a periodic sublattice producing a completely new crystalline phase with well-defined stoichiometry.

Following this procedure, the initial 77 MLs result in a total of 1348 ic-2D bilayers. Due to the large number of structures, we developed a high-throughput workflow to manage the DFT calculations. As illustrated in Fig. 1, the workflow consists of the three sub-sections described below:

*Stability workflow.* First, the ic-2D atomic structures are relaxed using the PBE exchange-correlation functional. Structures that undergo major rearrangements during relaxation or present no significant chemical bonding between the the intercalated atoms and the 2D layers, are discarded. The remaining ic-2D structures represent covalently bonded 2D materials justifying the use of the PBE functional. In particular, we find that the use of the D3 correction to account for vdW interactions has a negligible effect on on the structures (see Fig. S3). The workflow then groups the ic-2D bilayers according to the parent MLs, and calculates the energy above the convex hull using the MLs from C2DB and most stable binary and ternary bulk compounds from the OQMD database[38] as reference phases. For each ic-concentration, the workflow selects the stacking/hollow site combination that yields the lowest formation energy, and keeps the structure if its energy above the convex hull fulfills $\Delta H_{\text{hull}} < 0.2$ eV/atom. Other structures with the same ic-concentration are not given further consideration. The selected ic-2D bilayers are then passed to the "Adsorption" and "Properties" workflows (right panels in Fig. 1).

*Adsorption workflow.* Different configurations are generated by adsorbing a hydrogen atom at each of the inequivalent adsorption sites at the surface of the ic-2D structure. Since hydrogen typically shows weak adsorbate-adsorbate interactions,[39] even at our relatively high hydrogen coverage (20-30%) the adsorbed atoms can be considered as isolated. After performing a structural optimization, the workflow filters out duplicate structures (initially different structures may become identical after relaxation). In order to reduce the overall computational cost, the zero point energy (ZPE) of the adsorbed hydrogen is calculated

only for the lowest-energy configuration and used for all the remaining configurations when evaluating the adsorption free energies.

*Properties workflow.* The workflow evaluates basic properties of the ic-2D materials including the stiffness tensor, the electronic band structure, the projected density of states, Fermi surface, Bader charges, and magnetic moments. This workflow is a part of the full property workflow used to characterise 2D materials in the C2DB.

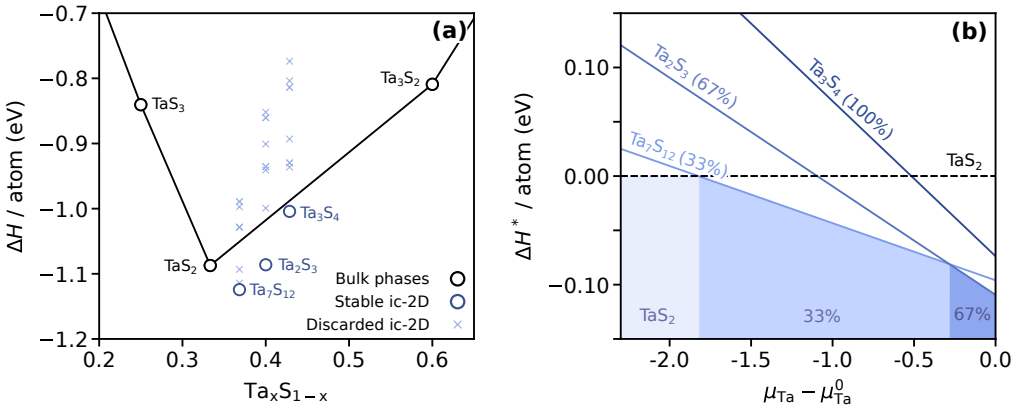


Figure 2: a) Ta-S convex hull including the stable self-intercalated phases (blue circles). The other tested configurations with higher formation energies are represented by blue crosses. b) Formation energy of the ic-2D phases as a function of the Ta chemical potential ($\mu_{\mathrm{Ta}}$) relative to the standard state. The asterisk in $\Delta H^*$ indicates that here $\mu_{\mathrm{Ta}}$ is treated as a free variable, while the S chemical potential $\mu_{\mathrm{S}}$ is constrained such that $TaS_2$ formation is always at equilibrium, *i.e.* $\mu_{\mathrm{Ta}} + 2\ \mu_{\mathrm{S}} = E(\mathrm{TaS_2})$. The ic-concentrations are shown in parentheses. The regions corresponding to different stable phases have been colored in blue.

**Thermodynamic stability** As previously described, the initial part of the workflow evaluates the thermodynamic stability of the candidate ic-2D structures. For each of the 77 host materials, the workflow collects the set of structures with identical stoichiometry (equivalently, the same ic-concentration). For each subset of structure, only the one with the lowest formation energy is kept. This results in 117 ic-2D structures that also satisfy our stability criterion of $\Delta H_{\mathrm{hull}} < 0.2$ eV/atom.

We further exclude the ic-2D structures where the distance between the intercalation

layer and any of the layers of the host system is larger than 3 Å. This indicates that the intercalation layer does not provide sufficient binding energy, resulting in a weakly interacting three-layer system rather than a new, covalently bonded phase.

Our final set of materials consists of the 95 ic-2D materials with $\Delta H_{\text{hull}} < 0.2$ eV/atom listed in Table S1-2. The subset of 40 ic-2D with $\Delta H_{\text{hull}} < 50$ meV/atom is shown in Table 1

Out of the initial 77 host materials, 39 have at least one ic-2D structure with $\Delta H_{\text{hull}} < 0.2$ eV/atom. As a general trend, the thermodynamic stability tends to decrease (i.e. the formation energy increases) for higher ic-concentrations. Several materials, however, satisfy our stability criterion even at high ic-concentrations. For instance, Fig. 2a shows the calculated convex hull for the ic-2D structures obtained from $TaS_2$ – one of the materials for which self-intercalation in the same concentration range has been realized experimentally.[23] Fig. 2b shows the relative stability of the ic-2D phases as a function of the Ta chemical potential ($\mu_{\text{Ta}}$), highlighting how, at progressively higher $\mu_{\text{Ta}}$ (Ta-rich environment), the pristine bilayer is replaced by its 33% and 67% intercalated phases.

We also find that the formation energy of the ic-2D tends to assume more negative values for the ic-2D where the ratio between the atomic radii of the metallic atom and the non-metallic atom is relatively large. This general trend is shown in Fig. S2.

**Comparison with experiments** Self-intercalation has been experimentally demonstrated for a number of the vdW materials considered in this work, namely $TaS_2$,[23] $TaSe_2$,[23] $VS_2$,[23,40,41] $NbS_2$,[14] $CrTe_2$,[28] $VTe_2$[28] and $TiTe_2$.[28] It is highly encouraging that for all these materials, the most stable ic-2D structure found by our workflow for all considered ic-concentrations, satisfy our general stability requirement of $\Delta H_{\text{hull}} < 0.2$ eV/atom. In fact, for most of the materials we find an ic-2D structure with negative $\Delta H_{\text{hull}}$ and for all the materials we always find at least one ic-concentration satisfying $\Delta H_{\text{hull}} < 50$ meV/atom. Below we provide a more detailed discussion for each of the materials.

ic-$TaS_2$ has been synthesised by CVD with ic-concentrations in the 25% to 100% range. In good agreement, we find the 33%, 67% and 100% ic-2D structures to be thermodynamically stable ($\Delta H_{\text{hull}} < 0$), thus confirming that $TaS_2$ constitutes a robust host system for self-intercalation over a broad concentration range. For the 33% ic-2D structure, the calculated in-plane lattice constant of 5.7 Å compares well with the experimental value of 5.8 Å.[23] The calculated distance between metal atoms belonging to the two $TaS_2$ layers is 6.0 Å while the experimental value is slightly larger, namely 6.6 Å.

ic-2D structures have also been experimentally realised for $TaSe_2$ in the same concentration range, although in this work we find lower stability towards intercalation as compared to $TaS_2$. The 33%, 67% and 100% phases all satisfy our $\Delta H_{\text{hull}}$ stability criterion, although the structures are predicted to be metastable relative to the pristine bilayer and Ta atoms in the solid phase. Specifically, the energy above the convex hull ($\Delta H_{\text{hull}}$) is 34, 105, and 176 meV, respectively. The calculated in-plane lattice constant is 5.9 Åfor both the 67% and 100% ic-2D structures, which is underestimated with respect to the experimental values (6.6 and 6.2 Å, respectively).

Self-intercalated vanadium disulphide $VS_2$ has been successfully synthesized at concentrations of 20-25%. In this work, we find the 33%-ic configuration to be thermodynamically stable and the 66%-ic as metastable, lying 24 meV above the convex hull.

$TiTe_2$ has been self-intercalated experimentally at 50% ic-concentration.[28] All three ic-2D structures generated in this work satisfy our stability criterion. The 66% and 100% ic-concentrations being slightly metastable (29 and 74 meV above the hull, respectively) and the 33% being thermodynamically stable.

For $CrTe_2$, a 50% ic-2D structure has been synthesised.[28] We predict the 25% and 50% ic-2D structures to be slightly meta-stable with $\Delta H_{\text{hull}}$ values of 30 and 40 meV, respectively. The calculated $d_{\text{m-m}}$ of 6.3 Å compares well with the experimental value of 5.9 eV.

Finally, multilayer $NbS_2$ has been self-intercalated experimentally[14] in a form, which we believe corresponds to the 33% ic-concentration based on the provided stoichiometry and

STEM images. We find the 33% and 67% ic-2D structures to be thermodynamically stable while the 100% ic-2D structure is predicted to be metastable with $\Delta H_{\text{hull}}$ of 59 meV. The calculated vertical distance between Nb atoms of the two $NbS_2$ layers is 6.5 Å in good agreement with the experimental value of 6.8 Å.

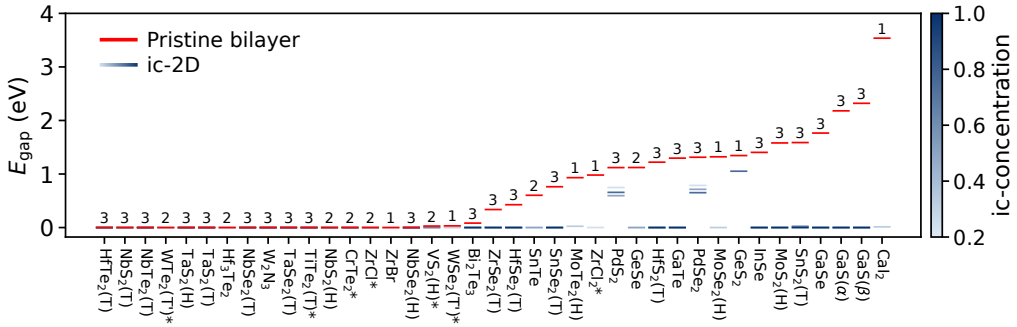


Figure 3: Band gap ($E_g$) of the pristine bilayer host systems (in red) and their ic-2D counterparts (in shades of blue). The x-axis displays the monolayer unit formulas and, in parenthesis, the crystalline phase (when available). Sytems with the same stoichiometry are labelled with greek letters when a reported crystalline phase is missing. An asterisk is appended to the label for systems with at least one magnetic ic-2D configuration. The ic-2D are reported in shades of blue according to the ic-concentration, following the color map on the side. Only ic-2D with $\Delta H_{hull} \leq 0.2$ eV/atom are considered. For each starting bilayer, the number of ic-2D configurations that satisfy this condition is reported above the pristine bilayer line.

**Electronic properties** The primary aim of this work is to investigate the viability of self-intercalation as a strategy to functionalize 2D materials. In order to assess how self-intercalation affects the intrinsic properties of the bilayer we have calculated the electronic band structures of the 95 most stable ic-2D structures and compared them to those of the pristine vdW bilayers.

Fig. 3 shows the electronic band gap of the 95 ic-2D structures (blue lines) and the pristine bilayers (red lines). The ic-concentration is indicated by the blue color code. Materials for which a magnetic ground state is found for at least one ic-concentration, are indicated by an asterisk. It can immediately be observed that self-intercalation always preserves the metallic nature when it is already present in the pristine bilayer. When the host bilayer

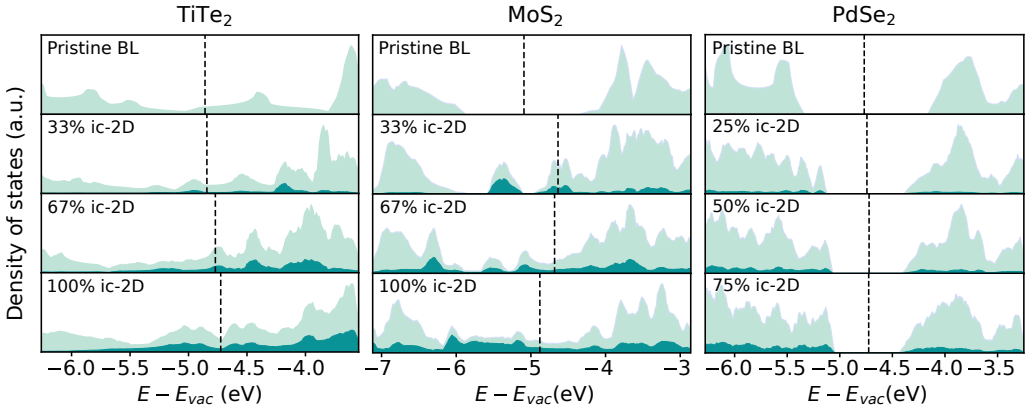


Figure 4: Density of states of ic-2D systems obtained from $TiTe_2$, $MoS_2$ and $PdSe_2$. For each, the top graph represents the total density of states of the corresponding pristine bilayer. The total density of states is shown in light blue, while the projections on the self-intercalated atoms are shown in darker blue. Vertical dashed lines represent the position of the Fermi level. Energies on the x-axis are relative to the vacuum level $E_{vac}$

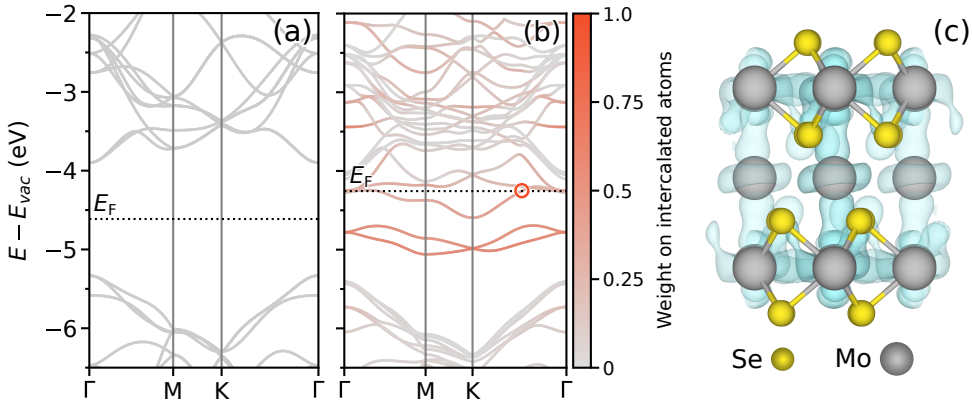


Figure 5: a) Band structure of a pristine $MoSe_2$ monolayer in a $(\sqrt{3} \times \sqrt{3})$R30 supercell. Energies are relative to the vacuum level, the Fermi energy is represented by a dashed line. b) Band structure of 33% self-intercalated $MoSe_2$, in the same supercell as for panel a). The color scale shows the projections of the eigenstates on the intercalated atoms. c) Real space distribution of the states highlighted by the red circle in panel b).

exhibits a finite band gap, this is either fully eliminated or significantly reduced upon self-intercalation. The enhanced metallicity observed in ic-2D obtained from semiconducting host systems agrees with the findings by Coelho *et al.* on self-intercalated $MoSe_2$ and $MoTe_2$.[42]

Fig. 4 illustrates the evolution of the density of states (DOS) as a function of ic-fraction for three representative systems, namely $TiTe_2$, $MoS_2$ and $PdSe_2$. These systems represent the three distinct cases of: (i) a metallic bilayer remaining metallic, (ii) a gapped bilayer evolving into a metal, and (iii) a semiconducting bilayer that remains gapped. Although intercalation does not change the metallic nature of $TiTe_2$, it significantly increases the DOS at the Fermi level. Thus even in cases of metals, self-intercalation enhances the metallicity. As illustrated by the case of $MoS_2$ (middle panel of Fig. 4) the transition from an insulator to a metal takes place already at relatively low ic-concentrations and occurs due to formation of new (metallic) states inside the band gap.

As an example, Fig. 5b shows the band structure of the 33%-intercalated $MoSe_2$ (H-phase), which has a 1.3 eV PBE band gap in its ML form. Bands with larger weight on the ic-atoms appear more red. Compared to the ML band structure, shown in Fig. 5a, it can be seen how bands with substantial weight on the intercalated atoms appear in the gap region, now crossing the Fermi level. Due to the covalent nature of the bonding between the intercalated atoms and the 2D host layers, such states are never fully localized on the ic-atoms and typically carry significant contributions from the surrounding atomic environment. Fig. 5c shows a contour plot of a wave function at the Fermi level (indicated by a red circle on the band structure plot). The wave function is mainly located on the Mo atoms of the structure and its orbital character is $d_{z^2}$-like.

As previously discussed, the initial pool of parent monolayers includes only non-magnetic materials, with the exception of $VS_2$ and $CrTe_2$. After self-intercalation, a magnetic ground state arises as an emergent property for the five different, initially non-magnetic, ic-2D materials (see table S1-2): 100%-ic $TiTe_2$, 33% and 50%-ic $W_2Se_4$, 33%-ic ZrCl and 25%-ic $ZrCl_2$. Note that $VS_2$ preserves the magnetic ground state only at 33% ic-concentration,

while the 67% phase is found to be non-magnetic, i.e. in this case self-intercalation suppresses magnetism.

The significant changes in the electronic properties induced by self-intercalation suggests that the ic-2D materials could complement the original 2D materials in useful ways. Importantly, the pristine and self-intercalated materials share the same chemical elements. In addition, the lattice constants are very similar (see the SI). Thus the pristine 2D material and the ic-2D counterparts are chemically and structurally highly compatible. This could be useful for construction of 2D electronic devices, particular, field effect transistors. For example, one could imagine using a metallic ic-2D material as electrical contact to a its semiconducting pristine counterpart. The high degree of compatibility of the two types of materials are expected to yield high quality interfaces, which is key in order to minimise the contact resistance.

**Catalytic properties** As shown in the previous section, self-intercalation can significantly affect the electronic properties of the host system, e.g. by reducing the band gap of an insulating/semiconducting material, turning it into a metal, or increasing the density of states at the Fermi level of a metal. Since the reactivity of a material is directly related to its (surface) electronic structure, it is anticipated that the presence of intercalated metal atoms will affect the ability of the material to bind atoms or molecules at the basal plane. Ideally, intercalation could then be used to enhance the catalytic properties of an otherwise chemically inert 2D material. This hypothesis is explored in the following.

To investigate how self-intercalation can affect surface reactivity, we computed the hydrogen adsorption free energy, $\Delta G_{\mathrm{H}^*}$, on the 95 most stable ic-2D materials. It has been shown by Nørskov *et al.*[43,44] that $\Delta G_{\mathrm{H}^*}$ correlates well with the catalytic activity of a material towards the hydrogen evolution reaction (HER). More specifically, HER catalysts with higher exchange current densities and lower overpotentials tend to have $\Delta G_{\mathrm{H}^*}$ closer to zero.[43]

For each of the 95 selected ic-2D structures, we determined all the symmetry-inequivalent

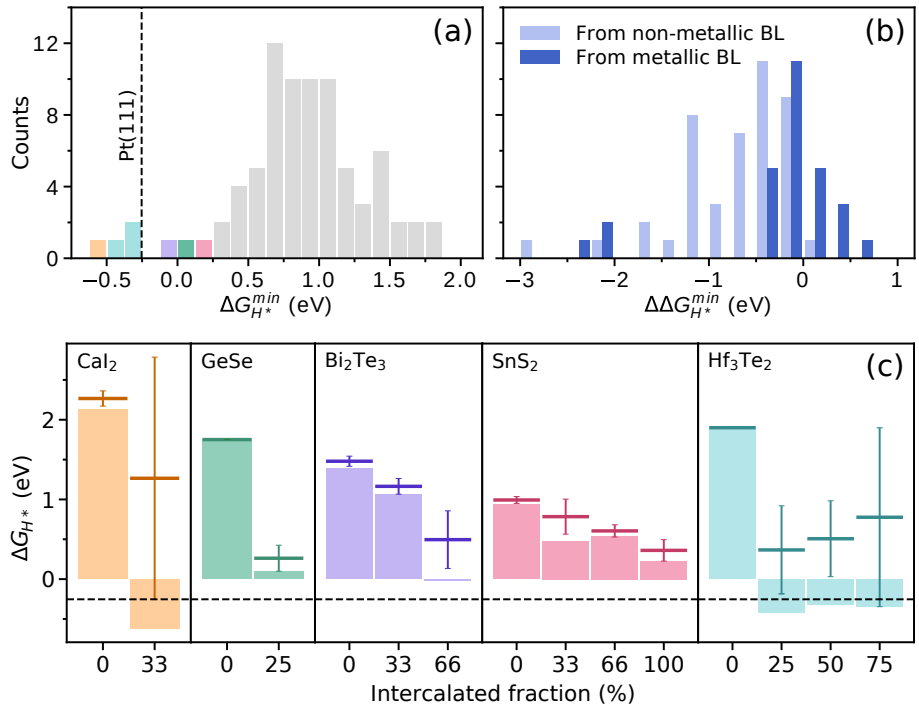


Figure 6: a) Distribution of the hydrogen adsorption energies on the lowest-energy site ($\Delta G_{H*}^{min}$) for the thermodynamically stable ic-2D. The colored bars correspond to the four ic-2D with $\Delta G_{H*}^{min}$ within 0.3 eV from the one calculated for a Pt(111) surface (-0.25 eV, dashed line). b) Distribution of the $\Delta G_{H*}^{min}$ of the ic-2D relative to the ones calculated for the pristine bilayers. light blue and dark blue bars gather the ic-2D obtained from non-metallic and metallic bilayers, respectively. c) Hydrogen adsorption energies $\Delta G_{H*}$ as a function of the ic-concentration. We selected the four systems having at least one ic-2D configuration that satisfies the criterion described for panel a). The filled bars represent $\Delta G_{H*}^{min}$, while the darker, horizontal lines correspond to the H adsorption energy averaged between all the adsorption sites. The error bars show the corresponding standard deviation. The horizontal dashed line shows, again, $\Delta G_{H*}^{min}$ of Pt(111). Colors are consistent with panel a).

adsorption sites on the surface and calculated the corresponding hydrogen adsorption energies. The Methods section provides detailed information on how $\Delta G_{\mathrm{H}^*}$ is calculated. We expect the site with the lowest $\Delta G_{\mathrm{H}^*}$ to dominate the overall reaction dynamics, and we denote the corresponding H adsorption energy as $\Delta G_{\mathrm{H}^*}^{\mathrm{min}}$. Fig. 6a shows the distribution of the calculated $\Delta G_{\mathrm{H}^*}^{\mathrm{min}}$ for the 95 ic-2D structures. The distribution is centered around 1.0 eV, far above the optimal, thermo-neutral adsorption required for HER catalysts. Nevertheless,

seven ic-2D structures are found to be promising candidates for the HER, with $\Delta G_{H^*}^{min}$ lying within 0.5 eV of the value obtained for a Pt(111) surface (-250 meV), here used as a model for the ideal HER catalyst. These seven systems are $CaI_2$ (33%-ic), GeSe (25%-ic), $Bi_2Te_3$ (66%-ic), $SnS_2$ (100%-ic) and $Hf_3Te_2$ (25, 50 and 75%-ic).

Fig. 6b shows the change in $\Delta G_{H^*}^{min}$ between the ic-2D structures and their parent pristine bilayers. The distribution points towards a general increase in the chemical reactivity, i.e. more negative adsorption energies, for ic-2D structures obtained from non-metallic host systems (red bars). This observation correlates well with the observed enhanced metallicity, which is expected to increase the chemical reactivity. For intrinsically metallic host materials (blue bars), self-intercalation seems to leave the reactivity either unaffected or slightly decreased. One prominent exception is ic-$Hf_3Te_2$ for which $\Delta G_{H^*}^{min}$ is more than 2 eV lower compared to the pristine bilayer, and in fact constitutes one of the most promising HER electro-catalysts found in this work.

The drastic change in $\Delta G_{H^*}^{min}$ observed for ic-$Hf_3Te_2$ is ascribed to a particular adsorption configuration in which H is able to penetrate the surface and bond to a Hf surface atom from an interstitial site. A similar configuration was found for 33%-ic $CaI_2$, which also showed a comparable change in $\Delta G_{H*}^{min}$ relative to the pristine bilayer. The two atomic structures are shown in figure S4. Interestingly, these special adsorption sites are activated by the self-intercalation. For the pristine bilayers these interstitial adsorption sites are also found upon relaxation, but the H adsorption energy is significantly higher and similar to those at the surface sites.

Fig. 6c shows the hydrogen adsorption energies as a function of the intercalated fraction for $CaI_2$, GeSe, $Bi_2Te_3$, $SnS_2$ and $Hf_3Te_2$. The colored bars represent $\Delta G_{H*}^{min}$ while the horizontal (vertical) lines represent the average (standard deviation) of the distribution of $\Delta G_{H*}$ over all adsorption sites. The variation in $\Delta G_{H*}$ among the different adsorption sites highlights how the presence of the intercalated atoms affects the local environment, resulting in a number of diverse and generally more reactive adsorption sites rather than the

few, chemically equivalent sites present on the pristine host systems.

In Ref.,[14] Yang *et al.* found that self-intercalated $NbS_2$ (H-phase) presented a significantly enhanced current density in electrocatalytic HER measurements as compared to the non-intercalated $NbS_2$. This enhancement was explained by DFT calculations showing hydrogen adsorption energies close to thermoneutrality ($\Delta G^{\min}_{H*}$) for the Nb-terminated surface of the intercalated system. We point out that Yang *et al.* report $Nb_{1.35}S_2$ as the experimentally observed stoichiometry, corresponding to 33% intercalation. However, their simulated structures seem to correspond to 100% intercalation. When comparing their reported hydrogen adsorption energy for the S-terminated surface with our 100%-ic configuration, we obtain a perfect agreement (1.00 eV and 0.997 eV, respectively).

The theoretical predictions presented by Yang *et al.* are intriguing, as they point towards the Nb-terminated surface being responsible for the observed enhancement in HER reactivity upon intercalation. Consequently, a more complete description of the HER on self-intercalated $NbS_2$ and other similar ic-2D structures should invoke an analysis of the relative stability of different surface terminations/compositions under the relevant electrochemical conditions.

# Conclusions

Our work shows that self-intercalation opens new possibilities for creating novel types of 2D materials with enhanced metallicity and basal plane activity and potential applications e.g. in (opto)electronics and catalysis. In accordance with most experiments on self-intercalated 2D materials (ic-2D), the structures investigated in this work possess a period arrangement of the intercalated atoms and corresponding well defined stoichiometries. Thus the considered ic-2D structures represent unique, crystalline, and covalently bonded 2D materials. Consequently, many of their basic properties were calculated and included in the open C2DB database. Several new stable ic-2D materials were identified by the high-throughput com-

putational workflow. It was shown that self-intercalation generally promotes metallicity and enhances the chemical reactivity of the materials, and a number of ic-2D materials were found to be promising as HER electrocatalysts based on the calculated hydrogen adsorption energy. Future work in this direction should explore the stability of different surface terminations/compositions of the ic-2D materials under HER conditions, i.e. their surface Pourbaix diagrams. It would also be interesting to examine the assumption of crystalline intercalation structures at finite temperatures and investigate their phase diagram (order-disorder transition), e.g. using Monte Carlo simulations.

# Methods

**Density functional theory calculations** All the DFT calculations are performed with the projector augmented wave (PAW) method[45,46] as implemented in the GPAW electronic structure code,[47] using the Perdew-Burke-Ernzerhof (PBE) exchange-correlation functional.[48] Spin polarization is always taken into account and a Fermi smearing of 0.05 eV is consistently applied. Structure optimizations are carried out in two steps, starting with a coarse relaxation of both the unit cell and the atomic positions until the forces are below 0.3 eV $\text{Å}^{-1}$, followed by a refinement of the atomic positions only until all forces are below 0.03 eV $\text{Å}^{-1}$. For relaxations, we use a plane-wave cutoff of 500 eV and a k-point density of 4 $\text{Å}^{-1}$. These are increased to 800 eV and 12 $\text{Å}^{-1}$, respectively, for electronic ground state calculations.

When relaxing hydrogen adsorption configurations, D3 corrections[49] are applied in order to take into account the van der Waals interactions. The corrections are not applied during the course of the C2DB properties workflow for two reasons: (1) the inter-layer bonding in ic-2D structures in absence of adsorbates is dominated by covalent interactions between the host material layers and the intercalated atoms, rather than dispersion interactions. The comparison between the thickness of ic-2D structures relaxed with and without D3

corrections shows no significant differences, as seen in Fig. S3. (2) for consistency with the computational parameters used in C2DB.[32]

Vibrational zero-point energies (ZPE) of the Hydrogen adsorbates on the ic-2D surfaces are calculated by displacing the adsorbed H atoms by $\pm 0.01$ Å along each direction while keeping all other atoms fixed.

**Structure generation and workflow** The ic-2D structures are generated using the Atomic Simulation Environment (ASE)[50] and its defect builder utility,[51] which can identify inequivalent hollow and adsorption sites based on the Voronoi tessellation method. The computational workflow is built using the ASR-MyQueue[52,53] framework.

**Hydrogen adsorption energetics** Hydrogen adsorption on a surface site, denoted by *, can be described by the chemical reaction

$$\mathrm{H}^+(aq) \; + \; e^- \; + \; * \; \rightleftharpoons \; \mathrm{H}^* \tag{1}$$

where $\mathrm{H}^*$ denotes a neutral hydrogen atom adsorbed on the surface site. Overall, the HER process is governed by the electrochemical reduction of solvated protons into gaseous hydrogen:

$$\mathrm{H}^+(aq) \; + \; e^- \; \rightleftharpoons \; 1/2 \; \mathrm{H}_2(g) \tag{2}$$

In standard conditions (pH 0, $p(\mathrm{H}_2) = 1$ bar) and at $U = 0$ vs. SHE, this process is at equilibrium ($\Delta G^0 = 0$), leading to the equivalence

$$\mu^0(\mathrm{H}^+) + \mu^0(e^-) = 1/2 \; \mu^0(\mathrm{H}_2) \tag{3}$$

Where $\mu^0(i)$ represents the standard chemical potential of species $i$ and will be represented herein by its calculated DFT total energy. This allows one to evaluate the Gibbs free energy

of reaction 1 (in the same conditions) as

$$\Delta G_{\mathrm{H}^*} = E^{DFT}(\mathrm{H}^*) - E^{DFT}(*) - 1/2\ E^{DFT}(\mathrm{H}_2) + \Delta\mathrm{ZPE} - T\Delta S \tag{4}$$

Where $E^{DFT}(*)$ and $E^{DFT}(\mathrm{H}^*)$ represent the calculated energy of the pristine surface and the surface with a H atom adsorbed, respectively. $\Delta$ZPE is the difference between the zero-point energies of an adsorbed hydrogen atom and hydrogen in the gas phase, while $\Delta S$ is the difference in their standard entropy. We neglect any entropic contribution coming from the solid surfaces and we assume the entropy of an adsorbed H atom to be small compared to the one in gas phase, hence we approximate $\Delta S \simeq 1/2\ S^0(\mathrm{H}_2(g))$. We use ZPE($\mathrm{H}_2$)=0.27 eV from Irikura[54] and $S^0(\mathrm{H}_2(g))$=0.41 eV from Chase *et al.*[55] The calculated total energy for a $\mathrm{H}_2$ molecule is -6.8 eV.

## Data Availability

The results reported in this article are freely available on the C2DB website.

## Acknowledgement

We acknowledge funding from the European Research Council (ERC) under the European Union's Horizon 2020 research and innovation program Grant No. 773122 (LIMA) and Grant agreement No. 951786 (NOMAD CoE). K. S. T. is a Villum Investigator supported by VILLUM FONDEN (grant no. 37789).

## Supporting Information Available

The provided supplementary material contains information about the effect of (a) self-intercalation on the lattice structure, (b) atomic composition on the formation energy. (c)

D3 corrections on the ic-2D structure. Atomic structure referenced in the article text are also provided. Finally, we include a table summarizing the main thermodynamic and electronic properties of all the 95 stable ic-2D.

# References


(1) Das, S.; Sebastian, A.; Pop, E.; McClellan, C. J.; Franklin, A. D.; Grasser, T.; Knobloch, T.; Illarionov, Y.; Penumatcha, A. V.; Appenzeller, J., et al. Transistors based on two-dimensional materials for future integrated circuits. *Nature Electronics* **2021**, *4*, 786–799.

(2) Cao, G.; Meng, P.; Chen, J.; Liu, H.; Bian, R.; Zhu, C.; Liu, F.; Liu, Z. 2D material based synaptic devices for neuromorphic computing. *Advanced Functional Materials* **2021**, *31*, 2005443.

(3) Ahn, E. C. 2D materials for spintronic devices. *npj 2D Materials and Applications* **2020**, *4*, 17.

(4) Wang, C.; You, L.; Cobden, D.; Wang, J. Towards two-dimensional van der Waals ferroelectrics. *Nature Materials* **2023**, 1–11.

(5) Lee, C. W.; Suh, J. M.; Jang, H. W. Chemical sensors based on two-dimensional (2D) materials for selective detection of ions and molecules in liquid. *Frontiers in Chemistry* **2019**, *7*, 708.

(6) Anichini, C.; Czepa, W.; Pakulski, D.; Aliprandi, A.; Ciesielski, A.; Samorì, P. Chemical sensing with 2D materials. *Chemical Society Reviews* **2018**, *47*, 4860–4908.

(7) Cummins, D. R.; Martinez, U.; Sherehiy, A.; Kappera, R.; Martinez-Garcia, A.; Schulze, R. K.; Jasinski, J.; Zhang, J.; Gupta, R. K.; Lou, J., et al. Efficient hydrogen

evolution in transition metal dichalcogenides via a simple one-step hydrazine reaction. *Nature communications* **2016**, *7*, 11857.

(8) Pandey, M.; Thygesen, K. S. Two-dimensional MXenes as catalysts for electrochemical hydrogen evolution: A computational screening study. *The Journal of Physical Chemistry C* **2017**, *121*, 13593–13598.

(9) Pandey, M.; Vojvodic, A.; Thygesen, K. S.; Jacobsen, K. W. Two-dimensional metal dichalcogenides and oxides for hydrogen evolution: a computational screening approach. *The journal of physical chemistry letters* **2015**, *6*, 1577–1585.

(10) Li, Z.; Wu, Y. 2D early transition metal carbides (MXenes) for catalysis. *Small* **2019**, *15*, 1804736.

(11) Zhang, J.; Zhao, Y.; Guo, X.; Chen, C.; Dong, C.-L.; Liu, R.-S.; Han, C.-P.; Li, Y.; Gogotsi, Y.; Wang, G. Single platinum atoms immobilized on an MXene as an efficient catalyst for the hydrogen evolution reaction. *Nature Catalysis* **2018**, *1*, 985–992.

(12) Mondal, A.; Vomiero, A. 2D Transition Metal Dichalcogenides-Based Electrocatalysts for Hydrogen Evolution Reaction. *Advanced Functional Materials* **2022**, *32*, 2208994.

(13) Han, J. H.; Kim, H. K.; Baek, B.; Han, J.; Ahn, H. S.; Baik, M.-H.; Cheon, J. Activation of the basal plane in two dimensional transition metal chalcogenide nanostructures. *Journal of the American Chemical Society* **2018**, *140*, 13663–13671.

(14) Yang, J.; Mohmad, A. R.; Wang, Y.; Fullon, R.; Song, X.; Zhao, F.; Bozkurt, I.; Augustin, M.; Santos, E. J.; Shin, H. S., et al. Ultrahigh-current-density niobium disulfide catalysts for hydrogen evolution. *Nature Materials* **2019**, *18*, 1309–1314.

(15) Jariwala, D.; Sangwan, V. K.; Lauhon, L. J.; Marks, T. J.; Hersam, M. C. Emerging device applications for semiconducting two-dimensional transition metal dichalcogenides. *ACS Nano* **2014**, *8*, 1102–1120.

(16) Briggs, N.; Subramanian, S.; Lin, Z.; Li, X.; Zhang, X.; Zhang, K.; Xiao, K.; Geohegan, D.; Wallace, R.; Chen, L.-Q., et al. A roadmap for electronic grade 2D materials. *2D Materials* **2019**, *6*, 022001.

(17) Peimyoo, N.; Deilmann, T.; Withers, F.; Escolar, J.; Nutting, D.; Taniguchi, T.; Watanabe, K.; Taghizadeh, A.; Craciun, M. F.; Thygesen, K. S., et al. Electrical tuning of optically active interlayer excitons in bilayer MoS2. *Nature Nanotechnology* **2021**, *16*, 888–893.

(18) Tran, K.; Moody, G.; Wu, F.; Lu, X.; Choi, J.; Kim, K.; Rai, A.; Sanchez, D. A.; Quan, J.; Singh, A., et al. Evidence for moiré excitons in van der Waals heterostructures. *Nature* **2019**, *567*, 71–75.

(19) Winther, K. T.; Thygesen, K. S. Band structure engineering in van der Waals heterostructures via dielectric screening: the G$\Delta$W method. *2D Materials* **2017**, *4*, 025059.

(20) Rajapakse, M.; Karki, B.; Abu, U. O.; Pishgar, S.; Musa, M. R. K.; Riyadh, S. S.; Yu, M.; Sumanasekera, G.; Jasinski, J. B. Intercalation as a versatile tool for fabrication, property tuning, and phase transitions in 2D materials. *npj 2D Materials and Applications* **2021**, *5*, 30.

(21) Wu, Y.; Li, D.; Wu, C.-L.; Hwang, H. Y.; Cui, Y. Electrostatic gating and intercalation in 2D materials. *Nature Reviews Materials* **2023**, *8*, 41–53.

(22) Zhang, P.; Xue, M.; Chen, C.; Guo, W.; Zhang, Z. Mechanism Regulating Self-Intercalation in Layered Materials. *Nano Letters* **2023**, *23*, 3623–3629.

(23) Zhao, X.; Song, P.; Wang, C.; Riis-Jensen, A. C.; Fu, W.; Deng, Y.; Wan, D.; Kang, L.; Ning, S.; Dan, J., et al. Engineering covalently bonded 2D layered materials by self-intercalation. *Nature* **2020**, *581*, 171–177.

(24) Cui, F.; Zhao, X.; Xu, J.; Tang, B.; Shang, Q.; Shi, J.; Huan, Y.; Liao, J.; Chen, Q.; Hou, Y., et al. Controlled growth and thickness-dependent conduction-type transition of 2D ferrimagnetic Cr2S3 semiconductors. *Advanced Materials* **2020**, *32*, 1905896.

(25) Li, H.; Wang, L.; Chen, J.; Yu, T.; Zhou, L.; Qiu, Y.; He, H.; Ye, F.; Sou, I. K.; Wang, G. Molecular beam epitaxy grown Cr2Te3 thin films with tunable Curie temperatures for spintronic devices. *ACS Applied Nano Materials* **2019**, *2*, 6809–6817.

(26) Wen, Y.; Liu, Z.; Zhang, Y.; Xia, C.; Zhai, B.; Zhang, X.; Zhai, G.; Shen, C.; He, P.; Cheng, R., et al. Tunable room-temperature ferromagnetism in two-dimensional Cr2Te3. *Nano Letters* **2020**, *20*, 3130–3139.

(27) Lasek, K.; Coelho, P. M.; Gargiani, P.; Valvidares, M.; Mohseni, K.; Meyerheim, H. L.; Kostanovskiy, I.; Zberecki, K.; Batzill, M. Van der Waals epitaxy growth of 2D ferromagnetic Cr(1+ $\delta$)Te2 nanolayers with concentration-tunable magnetic anisotropy. *Applied Physics Reviews* **2022**, *9*, 011409.

(28) Lasek, K.; Coelho, P. M.; Zberecki, K.; Xin, Y.; Kolekar, S. K.; Li, J.; Batzill, M. Molecular beam epitaxy of transition metal (Ti-, V-, and Cr-) tellurides: From monolayer ditellurides to multilayer self-intercalation compounds. *ACS nano* **2020**, *14*, 8473–8484.

(29) Li, Q.-Q.; Li, S.; Wu, D.; Ding, Z.-K.; Cao, X.-H.; Huang, L.; Pan, H.; Li, B.; Chen, K.-Q.; Duan, X.-D. Magnetic properties manipulation of CrTe2 bilayer through strain and self-intercalation. *Applied Physics Letters* **2021**, *119*, 162402.

(30) Li, R.; Jiang, J.; Bai, H.; Mi, W. Tailoring interlayer magnetic coupling to modify the magnetic properties of FeCl 2 bilayers by self-intercalation. *Journal of Materials Chemistry C* **2022**, *10*, 14955–14962.

(31) Guo, Y.; Liu, N.; Zhao, Y.; Jiang, X.; Zhou, S.; Zhao, J. Enhanced ferromagnetism of CrI3 bilayer by self-intercalation. *Chinese Physics Letters* **2020**, *37*, 107506.

(32) Haastrup, S.; Strange, M.; Pandey, M.; Deilmann, T.; Schmidt, P. S.; Hinsche, N. F.; Gjerding, M. N.; Torelli, D.; Larsen, P. M.; Riis-Jensen, A. C., et al. The Computational 2D Materials Database: high-throughput modeling and discovery of atomically thin crystals. *2D Materials* **2018**, *5*, 042002.

(33) Gjerding, M. N.; Taghizadeh, A.; Rasmussen, A.; Ali, S.; Bertoldo, F.; Deilmann, T.; Knøsgaard, N. R.; Kruse, M.; Larsen, A. H.; Manti, S., et al. Recent progress of the computational 2D materials database (C2DB). *2D Materials* **2021**, *8*, 044002.

(34) Bergerhoff, G.; Brown, I.; Allen, F., et al. Crystallographic databases. *International Union of Crystallography, Chester* **1987**, *360*, 77–95.

(35) Gražulis, S.; Daškevič, A.; Merkys, A.; Chateigner, D.; Lutterotti, L.; Quiros, M.; Serebryanaya, N. R.; Moeck, P.; Downs, R. T.; Le Bail, A. Crystallography Open Database (COD): an open-access collection of crystal structures and platform for world-wide collaboration. *Nucleic acids research* **2012**, *40*, D420–D427.

(36) Taylor, S. R. Abundance of chemical elements in the continental crust: a new table. *Geochimica et cosmochimica acta* **1964**, *28*, 1273–1285.

(37) Pakdel, S.; Rasmussen, A.; Taghizadeh, A.; Kruse, M.; Olsen, T.; Thygesen, K. S. Emergent properties of van der Waals bilayers revealed by computational stacking. *arXiv preprint arXiv:2304.01148* **2023**,

(38) Saal, J. E.; Kirklin, S.; Aykol, M.; Meredig, B.; Wolverton, C. Materials design and discovery with high-throughput density functional theory: the open quantum materials database (OQMD). *Jom* **2013**, *65*, 1501–1509.

(39) Gossenberger, F.; Juarez, F.; Groß, A. Sulfate, bisulfate, and hydrogen co-adsorption on Pt (111) and Au (111) in an electrochemical environment. *Frontiers in Chemistry* **2020**, *8*, 634.

(40) Yang, M.; Cao, L.; Wang, Z.; Qu, Y.; Shang, C.; Guo, H.; Xiong, W.; Zhang, J.; Shi, R.; Zou, J., et al. Vanadium self-intercalated C/V1. 11S2 nanosheets with abundant active sites for enhanced electro-catalytic hydrogen evolution. *Electrochimica Acta* **2019**, *300*, 208–216.

(41) Zhang, C. Y.; Sun, G. W.; Liu, Q. Y.; Pan, J. L.; Wang, Y. C.; Zhao, H.; Sun, G. Z.; Gao, X. P.; Pan, X. J.; Zhou, J. Y., et al. Deciphering the catalysis essence of vanadium self-intercalated two-dimensional vanadium sulfides (V5S8) on lithium polysulfide towards high-rate and ultra-stable Li-S batteries. *Energy Storage Materials* **2021**, *43*, 471–481.

(42) Coelho, P. M.; Komsa, H.-P.; Coy Diaz, H.; Ma, Y.; Krasheninnikov, A. V.; Batzill, M. Post-synthesis modifications of two-dimensional MoSe2 or MoTe2 by incorporation of excess metal atoms into the crystal structure. *ACS nano* **2018**, *12*, 3975–3984.

(43) Nørskov, J. K.; Rossmeisl, J.; Logadottir, A.; Lindqvist, L.; Kitchin, J. R.; Bligaard, T.; Jonsson, H. Origin of the overpotential for oxygen reduction at a fuel-cell cathode. *The Journal of Physical Chemistry B* **2004**, *108*, 17886–17892.

(44) Montoya, J. H.; Seitz, L. C.; Chakthranont, P.; Vojvodic, A.; Jaramillo, T. F.; Nørskov, J. K. Materials for solar fuels and chemicals. *Nature materials* **2017**, *16*, 70–81.

(45) Blöchl, P. E. Projector augmented-wave method. *Physical review B* **1994**, *50*, 17953.

(46) Kresse, G.; Joubert, D. From ultrasoft pseudopotentials to the projector augmented-wave method. *Physical review b* **1999**, *59*, 1758.

(47) Enkovaara, J.; Rostgaard, C.; Mortensen, J. J.; Chen, J.; Dułak, M.; Ferrighi, L.; Gavnholt, J.; Glinsvad, C.; Haikola, V.; Hansen, H., et al. Electronic structure calculations with GPAW: a real-space implementation of the projector augmented-wave method. *Journal of physics: Condensed matter* **2010**, *22*, 253202.

(48) Perdew, J. P.; Burke, K.; Ernzerhof, M. Generalized gradient approximation made simple. *Physical review letters* **1996**, *77*, 3865.

(49) Grimme, S.; Antony, J.; Ehrlich, S.; Krieg, H. A consistent and accurate ab initio parametrization of density functional dispersion correction (DFT-D) for the 94 elements H-Pu. *The Journal of chemical physics* **2010**, *132*.

(50) Larsen, A. H.; Mortensen, J. J.; Blomqvist, J.; Castelli, I. E.; Christensen, R.; Dułak, M.; Friis, J.; Groves, M. N.; Hammer, B.; Hargus, C., et al. The atomic simulation environment—a Python library for working with atoms. *Journal of Physics: Condensed Matter* **2017**, *29*, 273002.

(51) Davidsson, J.; Bertoldo, F.; Thygesen, K. S.; Armiento, R. Absorption versus adsorption: high-throughput computation of impurities in 2D materials. *npj 2D Materials and Applications* **2023**, *7*, 1–7.

(52) Gjerding, M.; Skovhus, T.; Rasmussen, A.; Bertoldo, F.; Larsen, A. H.; Mortensen, J. J.; Thygesen, K. S. Atomic Simulation Recipes: A Python framework and library for automated workflows. *Computational Materials Science* **2021**, *199*, 110731.

(53) Mortensen, J. J.; Gjerding, M.; Thygesen, K. S. MyQueue: Task and workflow scheduling system. *Journal of Open Source Software* **2020**, *5*, 1844.

(54) Irikura, K. K. Experimental vibrational zero-point energies: Diatomic molecules. *Journal of physical and chemical reference data* **2007**, *36*, 389–397.

(55) Chase, M. W.; (US), N. I. S. O. *NIST-JANAF thermochemical tables*; American Chemical Society Washington, DC, 1998; Vol. 9.

Table 1: List of ic-2D materials with $\Delta H_{\text{hull}} < 50$ meV/atom. For each material, we report the chemical formula of the parent monolayer, the intercalated fraction, the heat of formation, the energy above the convex hull, the band gap, and the magnetic moment.

| Parent ML | ic-fraction | $\Delta H_f$ (eV/atom) | $\Delta H_{\text{hull}}$ (eV/atom) | $E_{\text{gap}}$ (eV) | $\mu_{\text{mag}}$ |
|---|---|---|---|---|---|
| $Bi_2Te_3$ | 0.33 | -0.18 | 45.2 | 0 | 0 |
| $CrTe_2$ | 0.5 | -0.23 | 3.5 | 0 | 23.88 |
| | 1 | -0.23 | 16.2 | 0 | 28.74 |
| GaTe | 0.33 | -0.32 | 40.3 | 0 | 0 |
| $HfS_2$(T) | 0.33 | -1.57 | -39.2 | 0 | 0 |
| | 0.67 | -1.52 | -34.2 | 0 | 0 |
| | 1 | -1.4 | 29.8 | 0 | 0 |
| $HfSe_2$(T) | 0.33 | -1.31 | 4.1 | 0 | 0 |
| $HfTe_2$(T) | 0.33 | -0.8 | -2.1 | 0 | 0 |
| | 0.67 | -0.73 | 45.7 | 0 | 0 |
| InSe | 0.33 | -0.49 | 24 | 0 | 0 |
| $NbS_2$(H) | 0.33 | -1.17 | -51.6 | 0 | 0 |
| $NbS_2$(T) | 0.33 | -1.1 | 23.6 | 0 | 0 |
| | 0.67 | -1.17 | -12.1 | 0 | 0 |
| $NbSe_2$(H) | 0.33 | -0.9 | -10.3 | 0 | 0 |
| | 0.67 | -0.88 | 22.7 | 0 | 0 |
| $NbSe_2$(T) | 0.33 | -0.85 | 41.8 | 0 | 0 |
| $PdS_2$ | 0.25 | -0.27 | 30.5 | 0.75 | 0 |
| $PdSe_2$ | 0.25 | -0.28 | 13.1 | 0.79 | 0 |
| | 0.5 | -0.27 | 32.8 | 0.71 | 0 |
| $SnS_2$(T) | 0.33 | -0.38 | 35.5 | 0 | 0 |
| $SnSe_2$(T) | 0.33 | -0.36 | 9.8 | 0 | 0 |
| | 0.67 | -0.36 | 17.5 | 0 | 0 |
| | 1 | -0.38 | 16.8 | 0 | 0 |
| $TaS_2$(H) | 0.33 | -1.13 | -75.3 | 0 | 0 |
| | 0.67 | -1.09 | -70.2 | 0 | 0 |
| | 1 | -1.01 | -17.8 | 0 | 0 |
| $TaS_2$(T) | 0.33 | -1.05 | 2.3 | 0 | 0 |
| | 0.67 | -0.99 | 31.4 | 0 | 0 |
| $TaSe_2$(T) | 0.33 | -0.77 | 34.5 | 0 | 0 |
| $TiTe_2$(T) | 0.33 | -0.72 | -6.1 | 0 | 0 |
| | 0.67 | -0.69 | 28.7 | 0 | 0 |
| $VS_2$(H) | 0.33 | -0.96 | -26 | 0 | 1.51 |
| | 0.67 | -0.96 | 23.8 | 0 | 0 |
| $W_2N_3$ | 0.33 | -0.32 | -135 | 0 | 0 |
| | 0.67 | -0.31 | -121.1 | 0 | 0 |
| | 1 | -0.2 | -15.6 | 0 | 0 |
| $ZrSe_2$(T) | 0.33 | -1.38 | -60.4 | 0 | 0 |
| | 0.67 | -1.35 | -65.7 | 0 | 0 |
| | 1 | -1.3 | -49.8 | 0 | 0 |

# Functionalised 2D materials: Enhancing metallicity and chemical reactivity *via* self-intercalation

## Supporting information

Stefano Americo[1,*], Sahar Pakdel[1], and Kristian Sommer Thygesen[1]

[1]Computational Atomic-scale Materials Design (CAMD), Department of Physics, Technical University of Denmark, 2800 Kgs. Lyngby Denmark
[*]Email: steame@dtu.dk

## Effect of self-intercalation on the lattice constants

We compare the first component of the lattice constants between the intercalated phases and their pristine host structure. Self-intercalation does not change the unit cell of the material significantly, with the largest percentage variations being around 4.5% and the overall distribution centered around 0.

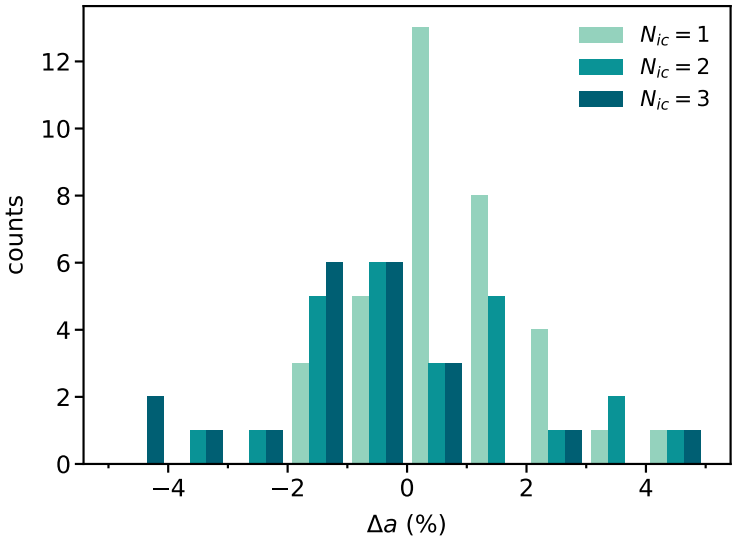


Figure 1: in-plane lattice constant variation ($\Delta a$) between the ic-2D and their corresponding pristine host materials, expressed as a percentage. The data set is subdivided according to the number of intercalated atoms in the ic-2D ($N_{ic}$)

## Correlation between atomic radii and formation energies

We investigated whether any descriptor based on the host material composition can be used in order to assess the stability of its intercalated phases. Here, materials with large metallic atoms relative to the non-metallic ones are found to generally produce more negative formation energies.

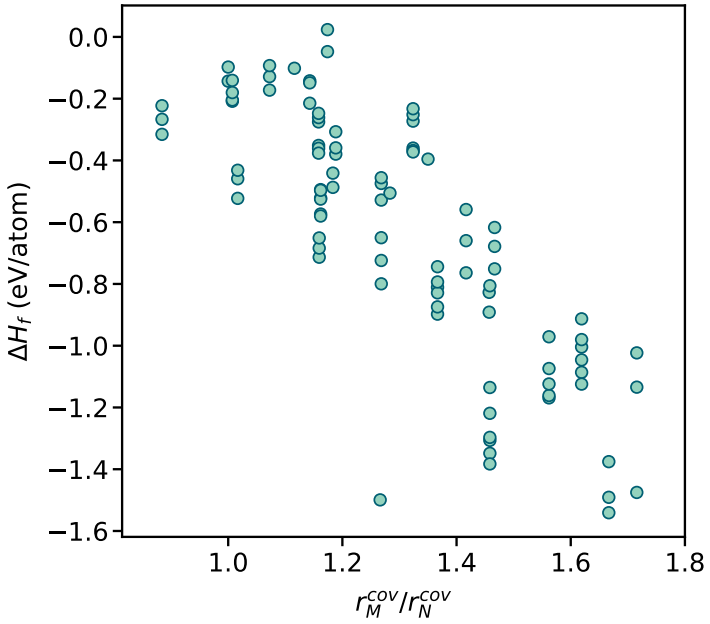


Figure 2: Formation energy of the stable ic-2D as a function of the ratio between the covalent radii of the metallic element ($r_M^{cov}$) and the non-metallic element ($r_N^{cov}$).

## Effect of van der Waals corrections on the ic-2D structure

We determine the effect of the D3 correction scheme on the thickness of the stable ic-2D, by comparing the relaxed structure of all the 95 stable ic-2D obtained with and without corrections. The thickness is defined as the difference between the largest and the smallest atomic coordinate along the z-axis. In general, we observe a good agreement between structures optimized with and without D3 corrections, with the exception of 25% and 100%-ic $PdS_2$, where the use of D3 results in a ca. 1 Å thinner structures.

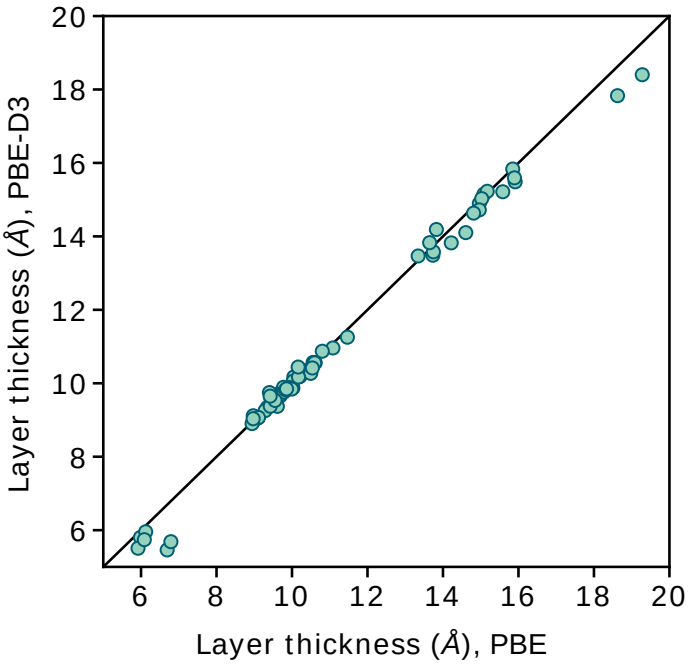


Figure 3: Comparison between the thicknesses of ic-2D relaxed with and without D3 corrections. The thickness is defined as the difference between the maximum and the minimum out-of-plane atomic coordinates in the structure.

## Highly stable H adsorption configurations

Here we show the structures of two hydrogen adsorption configurations that are significantly stabilized by self-intercalation.

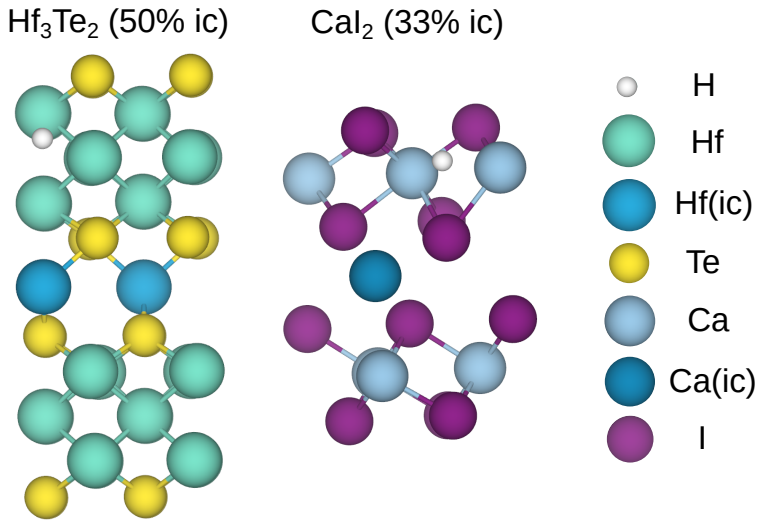


Figure 4: Hydrogen adsorption configurations providing the lowest $\Delta G_{\mathrm{H}*}^{\mathrm{min}}$ of 50%-ic $Hf_3Te_2$ and 33%-ic $CaI_2$.

## Complete list of stable ic-2D

| Parent ML | ic-fraction | $\Delta H$ (eV/atom) | $\Delta H_{\text{hull}}$ (eV/atom) | $E_{\text{gap}}$ (eV) | $\mu_{\text{mag}}$ |
|---|---|---|---|---|---|
| $Bi_2Te_3$ | 0.33 | -0.18 | 45.2 | 0 | 0 |
| | 0.67 | -0.14 | 76.1 | 0 | 0 |
| | 1 | -0.11 | 102.8 | 0 | 0 |
| $CaI_2$ | 0.33 | -1.5 | 78.9 | 0.01 | 0 |
| $CrTe_2$ | 0.5 | -0.23 | 3.5 | 0 | 23.88 |
| | 1 | -0.23 | 16.2 | 0 | 28.74 |
| GaSe | 0.33 | -0.53 | 51 | 0 | 0 |
| | 0.67 | -0.47 | 81.9 | 0 | 0 |
| | 1 | -0.45 | 87.2 | 0 | 0 |
| GaS($\alpha$) | 0.33 | -0.58 | 56.4 | 0 | 0 |
| | 0.67 | -0.53 | 84.7 | 0 | 0 |
| | 1 | -0.51 | 84.6 | 0 | 0 |
| GaS($\beta$) | 0.33 | -0.58 | 62.5 | 0 | 0 |
| | 0.67 | -0.52 | 89.2 | 0 | 0 |
| | 1 | -0.5 | 88.5 | 0 | 0 |
| GaTe | 0.33 | -0.32 | 40.3 | 0 | 0 |
| | 0.67 | -0.27 | 76 | 0 | 0 |
| | 1 | -0.23 | 105.2 | 0 | 0 |
| $GeS_2$ | 0.75 | -0.2 | 120.2 | 1.05 | 0 |
| GeSe | 0.25 | -0.15 | 68.6 | 0 | 0 |
| | 0.5 | -0.1 | 118.5 | 0 | 0 |
| $Hf_3Te_2$ | 0.25 | -0.54 | 54.5 | 0 | 0 |
| | 0.5 | -0.48 | 98.1 | 0 | 0 |
| $HfS_2$(T) | 0.33 | -1.57 | -39.2 | 0 | 0 |
| | 0.67 | -1.52 | -34.2 | 0 | 0 |
| | 1 | -1.4 | 29.8 | 0 | 0 |
| $HfSe_2$(T) | 0.33 | -1.31 | 4.1 | 0 | 0 |
| | 0.67 | -1.22 | 58.6 | 0 | 0 |
| | 1 | -1.14 | 111.7 | 0 | 0 |
| $HfTe_2$(T) | 0.33 | -0.8 | -2.1 | 0 | 0 |
| | 0.67 | -0.73 | 45.7 | 0 | 0 |
| | 1 | -0.66 | 95.7 | 0 | 0 |
| InSe | 0.33 | -0.49 | 24 | 0 | 0 |
| | 0.67 | -0.44 | 51.9 | 0 | 0 |
| | 1 | -0.42 | 52.8 | 0 | 0 |
| $MoS_2$(H) | 0.33 | -0.75 | 118.3 | 0 | 0 |
| | 0.67 | -0.68 | 146.9 | 0 | 0 |
| | 1 | -0.62 | 169.1 | 0 | 0 |
| $MoSe_2$(H) | 0.33 | -0.51 | 158.3 | 0 | 0 |
| $MoTe_2$(H) | 0.33 | -0.11 | 189.9 | 0.02 | 0 |
| $NbS_2$(H) | 0.33 | -1.17 | -51.6 | 0 | 0 |
| | 0.67 | -1.17 | -12.1 | 0 | 0 |
| | 1 | -1.13 | 55.5 | 0 | 0 |
| $NbS_2$(T) | 0.33 | -1.1 | 23.6 | 0 | 0 |
| | 0.67 | -1.05 | 103 | 0 | 0 |
| $NbSe_2$(H) | 0.33 | -0.9 | -10.3 | 0 | 0 |
| | 0.67 | -0.88 | 22.7 | 0 | 0 |
| | 1 | -0.82 | 96.4 | 0 | 0 |

Table 1: List of ic-2D materials with energy above the convex hull, $\Delta H_{\text{hull}} < 200$ meV/atom. For each material, we report the chemical formula of the parent monolayer, the intercalated fraction, the heat of formation, the energy above the convex hull, the band gap, and the magnetic moment.

| Parent ML | ic-fraction | $\Delta H$ (eV/atom) | $\Delta H_{\text{hull}}$ (eV/atom) | $E_{\text{gap}}$ (eV) | $\mu_{\text{mag}}$ |
|---|---|---|---|---|---|
| $NbSe_2$(T) | 0.33 | -0.85 | 41.8 | 0 | 0 |
| | 0.67 | -0.8 | 103.8 | 0 | 0 |
| | 1 | -0.75 | 161.9 | 0 | 0 |
| $NbTe_2$(T) | 0.33 | -0.4 | 68.8 | 0 | 0 |
| | 0.67 | -0.36 | 116.4 | 0 | 0 |
| | 1 | -0.31 | 176 | 0 | 0 |
| $PdS_2$ | 0.25 | -0.27 | 30.5 | 0.75 | 0 |
| | 0.5 | -0.26 | 53.4 | 0.6 | 0 |
| | 0.75 | -0.24 | 77.1 | 0.66 | 0 |
| $PdSe_2$ | 0.25 | -0.28 | 13.1 | 0.79 | 0 |
| | 0.5 | -0.27 | 32.8 | 0.71 | 0 |
| | 0.75 | -0.25 | 51.2 | 0.65 | 0 |
| $SnS_2$(T) | 0.33 | -0.38 | 35.5 | 0 | 0 |
| | 0.67 | -0.36 | 62.1 | 0.02 | 0 |
| | 1 | -0.37 | 64.2 | 0 | 0 |
| $SnSe_2$(T) | 0.33 | -0.36 | 9.8 | 0 | 0 |
| | 0.67 | -0.36 | 17.5 | 0 | 0 |
| | 1 | -0.38 | 16.8 | 0 | 0 |
| SnTe | 0.25 | -0.18 | 87.1 | 0 | 0 |
| | 0.5 | -0.14 | 117 | 0 | 0 |
| $TaS_2$(H) | 0.33 | -1.13 | -75.3 | 0 | 0 |
| | 0.67 | -1.09 | -70.2 | 0 | 0 |
| | 1 | -1.01 | -17.8 | 0 | 0 |
| $TaS_2$(T) | 0.33 | -1.05 | 2.3 | 0 | 0 |
| | 0.67 | -0.99 | 31.4 | 0 | 0 |
| | 1 | -0.91 | 73.1 | 0 | 0 |
| $TaSe_2$(T) | 0.33 | -0.77 | 34.5 | 0 | 0 |
| | 0.67 | -0.66 | 105.4 | 0 | 0 |
| | 1 | -0.56 | 175.6 | 0 | 0 |
| $TiTe_2$(T) | 0.33 | -0.72 | -6.1 | 0 | 0 |
| | 0.67 | -0.69 | 28.7 | 0 | 0 |
| | 1 | -0.65 | 74.1 | 0 | 4.97 |
| $VS_2$(H) | 0.33 | -0.96 | -26 | 0 | 1.51 |
| | 0.67 | -0.96 | 23.8 | 0 | 0 |
| $W_2N_3$ | 0.33 | -0.32 | -135 | 0 | 0 |
| | 0.67 | -0.31 | -121.1 | 0 | 0 |
| | 1 | -0.2 | -15.6 | 0 | 0 |
| $WSe_2$(T') | 0.33 | -0.41 | 172.7 | 0 | 2.1 |
| | 0.25 | 0.03 | 165.8 | 0 | 0 |
| | 0.5 | 0.02 | 146.8 | 0 | 2.46 |
| ZrBr | 0.33 | -0.81 | 187.2 | 0 | 0 |
| $ZrCl_2$ | 0.25 | -1.48 | 165.3 | 0 | 2.08 |
| | 0.33 | -1.14 | 135.4 | 0 | 2.2 |
| | 0.67 | -1.03 | 198.7 | 0 | 0 |
| $ZrSe_2$(T) | 0.33 | -1.38 | -60.4 | 0 | 0 |
| | 0.67 | -1.35 | -65.7 | 0 | 0 |
| | 1 | -1.3 | -49.8 | 0 | 0 |

Table 2: continuation of Table 1

Technology plays a pivotal role in modern society. It shapes our lifestyle and the way we communicate. it allows us to travel long distances both physically and digitally and, in general, makes our life easier. The transistors in computer processors, the batteries powering our smartphones, the antennas in GPS navigation systems are examples of essential devices in modern technology. All of them are based on a clever combination of materials with unique properties.

Some physical properties relevant for device construction are the ability to conduct electricity, to absorb light and chemically interact with the surrounding environment. The particular combination of these features in a material results from the delicate interplay between atomic nuclei and electrons, defining its microscopic structure. By adopting an *ab initio* approach based on the laws of quantum mechanics, we can investigate the atomic and electronic structure of virtually any material and predict its properties.

In this thesis, we explore from first principles the electronic and catalytic properties of a wide range of two-dimensional materials, characterized by one or few atomically thin layers distributed on a plane. We show how these highly versatile layers can be used as building blocks in more complex two-dimensional structures. For instance, a completely new material can be realized by introducing additional metallic atoms in between two identical layers, increasing the electric conductivity and the ability to accelerate chemical reactions. New two-dimensional materials can also be obtained by stacking layers of different composition on top of each other, obtaining van der Waals heterostructures with hybrid properties.

Any material, two-dimensional or not, can dissolve and undergo undesired degradation when immersed in solution and subject to electric fields. Here, we present two general models - one relying on bulk properties, the other centered on the microscopic surface structure - aimed at predicting the likelihood of such events in conditions relevant for clean energy conversion processes.

**Technical University of Denmark**
**DTU Physics**
**Department of Physics**

Fysikvej 311
2800 Kongens Lyngby, Denmark
Phone: +45 4525 3344
info@fysik.dtu.dk

www.fysik.dtu.dk